Spectroscopic Studies of Surface Chemistry on Cerium Oxide

Zur Erlangung des akademischen Grades eines

DOKTORS DER NATURWISSENSCHAFTEN

(Dr. rer. nat.)

der KIT-Fakultät für Chemie und Biowissenschaften

des Karlsruher Instituts für Technologie (KIT)

genehmigte

DISSERTATION

von

M.Eng. Chengwu Yang

aus

Linyi, China

KIT-Dekan: Prof. Dr. Willem M. Klopper

Referent: Prof. Dr. Christof Wöll

Korreferent: Prof. Dr. Olaf Deutschmann

Tag der mündlichen Prüfung: 22.07.2016

I hereby declare that this dissertation represents the result of my own original research from November 2012 to July 2016 at the Karlsruhe Institute of Technology (KIT) under the supervision of Prof. Dr. Christof Wöll, and it has not been submitted to any other institution for another degree or qualification. Those sections of this work, which were taken from other sources – cited directly or indirectly – are quoted as such.

Karlsruhe 06.06.2016 Chengwu Yang

Acknowledgements

This thesis represents the end of my PhD journey. It would not have come to fruition without the support of many helping hands and minds. Therefore, I would like to express my gratitude towards all of the people who have made these studies possible for me with helpful comments, practical advice and moral support.

First and foremost, I would like to express the deepest appreciation to my supervisor, Prof. Dr. Christof Wöll, for giving me the chance to study here and showing me how the genuine science works. I very admire his profound knowledge and keen intuition in science and great research habits.

I am also grateful to my co-supervisor, Prof. Dr. Olaf Deutschmann, for accepting me as a member of the Helmholtz Research School and many constructive discussions.

I am extremely indebted to Dr. Alexei Nefedov and Dr. Yuemin Wang for their excellent supervision, continuous encouragement, and great help, not only in science but also in my daily life. They are the best leaders I ever met, and my research could not go well without their organization and support.

Many thanks for the financial support from the China Scholarship Council (CSC) and the Helmholtz Research School Energy-Related Catalysis, where I received a continuous living stipend and research grant over the last three and half years.

Furthermore, I would like to give my special thanks to THEO colleagues. Dr. Hikmet Sezen, Dr. Fabian Bebensee, Dr. Maria Buchholz, Stefan Heißler, Dr. Carsten Natzeck, and Dr. Jun Chen taught me all the details of working on the ultra-high vacuum (UHV) apparatus. Xiaojuan Yu and Ludger Schöttner helped me overcome many technical problems.

I would like to thank all colleagues at the COOI department, Dr. Peter Weidler, Dr. Hartmut Gliemann, Dr. Jinxuan Liu, Dr. Zhengbang Wang, Dr. Sophia Schmitt, Dr. Zhigang Gu, Wencai Zhou, Dr. Wei Guo, Dr. Jianxi Liu, Peter Krolla-Sidenstein, Dr. Peter Lindemann, Dr. Carlos Azucena, Dr. Alexander Welle, Dr. Engelbert Redel, Dr. Manuel Tsotsalas, Julia Hümmer, Dr. Michael Naboka, PD Dr. Lars Heinke, Qi An, Kai Müller,

Stefanie Sellheim-Ret, and Astrid Biedermann, for the wonderfully professional, friendly and positive working atmosphere.

I also would like to thank all the members of Helmholtz Research School Energy-Related Catalysis for excellent ideas and stimulating discussions. I would like to acknowledge in particular Dr. Steffen Tischer and Dr. Claudia Antinori for their great organization. I benefit a lot from the summer schools, winter schools and soft skill courses.

I am very grateful to Mr. Wolfram Kessler (Oerlikon KN) and Mr. Mike Füßler for their excellent technical support.

I greatly appreciate the external collaborations with Prof. Dr. Joachim Sauer, Dr. Joachim Paier, and Thomas Kropp from Humboldt-Universität zu Berlin, Prof. Dr. Xue-Qing Gong and Li-Li Yin from East China University of Science and Technology, PD Dr. Karin Fink and Dr. Qiang Li from KIT, for the theoretical calculations, which help us deeply understand our experimental observations. I also would like to acknowledge Prof. Dr. Jan-Dierk Grunwaldt (KIT), Prof. Dr. Claus Feldmann (KIT), Prof. Dr. Alessandro Trovarelli (Università di Udine, Italy), Prof. Dr. Martin Muhler (Ruhr-Universität Bochum), and Prof. Dr. Michael Reichling (Universität Osnabrück), for sharing their very nice powder and film ceria samples. A big thanks also goes to Peter Droste of SurfaceNet who satisfies all my needs and always supplies me with the best ceria single crystals.

I also take this opportunity to sincerely acknowledge my master's advisor, Prof. Dr. Minghan Han (Tsinghua University, China), for his support and encouragement all along. I am also very grateful to Prof. Dr. Fei Wei (Tsinghua University, China) for his kind help when I was applying to study abroad.

This thesis is dedicated to the memory of my grandfather. He said he would wait for me to come back home. I miss him dearly. I would like to give my heartfelt thanks to my family for their endless love and spiritual support, in particular to my beloved fiancee, Jingjing, for her love, patience, and sacrifice during my PhD study.

Besides all I earnestly thank each and every one from the bottom of my heart and I also pay my sincere apology to those if I have not offer my thankfulness.

Preface

When I came to Germany in November 2012, I just finished my master's degree after three years of hard work in industrial catalysis. In those days I developed the catalyst for a process of trying to converse corrosive by-product hydrogen chloride (HCl) into more valuable chlorine (Cl_2). This process was invented by a British chemist Henry Deacon in 1868 and therefore is called Deacon process. Though its history is as long as that of catalysis, a suitable catalyst for large-scale industrial production is still not found yet. As I was told, it is normal since the R&D of industrial catalysts nowadays still remains empirically like cooking. It was not funny at all for a rookie like me who had to handle HCl and Cl_2 every day and was waving over whether to continue in this filed. Until I met THEO and our HESGM endstation at the synchrotron facility (BESSY II) and after worked on them over last three and half years, I have been often astonished that (model) catalysis studies can even be done so microscopically and so precisely.

I know ceria back to my master phase when I added it routinely into my HCl oxidation catalyst as a promoter. It is so magic a material that can inhibit the sintering of the supported Cu particles and provide active O species for the reaction like a reservoir. Thus I was so excited that I can continue working with it during my PhD, and later I had the luck to find a source who can supply the precious bulk ceria single crystal samples. These bulk single crystals are believed to be very difficult to obtain.

Combined our unique spectroscopic techniques and scarce bulk ceria single crystals, we produced many interesting results. These results enable us to settle some long-standing disputes, such as the assignments of IR-bands of probe molecules (CO and methanol) and whether the reduced ceria is re-oxidized by CO_2, and thus it proves to me the elegance and great power of surface science approach. Some ongoing projects are not included in this thesis like O_2 and N_2O interaction with ceria, and I would like to accomplish them before I move back to China. After finishing this thesis, I just hope it is worth of reading and can help its readers, if possible, to some extent, at least help them to think about the underlying problems in this thesis.

06.06.2016 Karlsruhe

Contents

1 Introduction

1.1 Catalysis and surface science

The famous Swedish chemist Jöns Jacob Berzelius, from 1821 on, summarized and reviewed critically the scientific investigations conducted worldwide in his "Annual Report" (Jahresberichte). In his 1835 report, Berzelius coined the term "catalysis" to describe the phenomenon that certain substances influenced the progress of a chemical reaction without being consumed and hence apparently not being affected by this reaction [1]. Throughout the rest of the 19th century both the term and the phenomenon remained heavily debated [2] until around 1900 the German chemist Wilhelm Ostwald proposed a now generally accepted definition: "A catalyst is a substance which affects the rate of a chemical reaction without being part of its end products" [3, 4]. Ostwald's contributions to catalysis were recognized with the Nobel Prize for Chemistry in 1909. The catalyst changes the kinetics of the reaction by forming intermediates with the molecules involved in the reaction, offering them an alternate, more rapid path to the final products, but does not change the thermodynamics.

Catalysis is of vital importance. The applications of catalysis are numerous, and impact heavily on our daily lives. In living organisms, enzymes accelerate or catalyze almost all of the biochemical reactions. Manmade catalytic processes are pivotal to the production of fuels, foods, chemicals, pharmaceuticals, and a host of materials (e.g. plastics and fibers). In environmental chemistry, catalysts are essential to break down pollutants such as automobile and industrial exhausts.

All three types of catalysts (i.e. enzymes, homogeneous, and heterogeneous) operate by the same fundamental principles, and their properties derive from the electronic and geometric (steric) characteristics of the active centers. More relevant in technical processes is heterogeneous catalysis, where the catalyst is a solid and the reacting molecules interact with its surface from the gaseous or liquid phases, and it has been estimated that ~90% of all chemical processes use heterogeneous catalysts [5]. The main advantage of using a heterogeneous catalyst is that, being a solid material, it is easy to separate from the gas and/or liquid reactants and products of the overall catalytic reaction.

The atoms in the surface of the solid catalyst have fewer nearest neighbors than those in the bulk. As a consequence, these surface atoms are chemically unsaturated and may give rise to bond formation with atoms in impinging molecules from the adjacent gas or liquid phase, a phenomenon known as chemisorption. By this step, existing bonds will be modified or may even be broken (dissociative chemisorption). The chemisorbed species are mobile on the surface and may react with others, and the produced molecules eventually leave the surface (desorption) as the desired reaction products. If operated in a flow reactor, the catalyst can in this way continuously operate without being consumed.

However, the study on surface chemistry of "real" catalysts is hampered by fundamental problems. A catalyst with high activity generally has to exhibit a high specific surface area. Apart from the use of highly porous materials with large "internal" surface areas (e.g. zeolites), this is mostly achieved by depositing small particles of the active catalyst material onto (more or less) inert high surface area supports. Moreover, the reacting systems exist merely as two-dimensional phases for which most of the usual methods of investigation are not well suited. All these effects render the surface chemistry of a "real" catalyst rather complex. A possible strategy to overcome this problem was already proposed by Irving Langmuir [6] in 1922: "*Most finely divided catalysts must have structures of great complexity. In order to simplify our theoretical consideration of reactions at surfaces, let us confine our attention to plane surfaces. If the principles in this case are well understood, it should then be possible to extend the theory to the case of porous bodies. In general, we should look upon the surface as consisting of a checkerboard…*"

The so-called "surface science approach" [7] that Langmuir had in mind was experimentally not yet accessible in his days, but began to become available during the 1960s with the advent of ultrahigh vacuum (UHV) and surface sensitive analytical methods [8-11]. Nowadays a whole arsenal of such techniques is available to study the structural, electronic, or dynamic properties of such well-defined single crystal surfaces.

While the majority of surface science studies have been carried out on well-defined single crystal surfaces under UHV conditions, most catalytically active systems are employed at high pressure or at solid-liquid interfaces. This gap between UHV and industrial conditions is known as the "pressure gap". In addition, since the properties of well-defined single crystal surfaces will generally be quite different from the surface properties of "real" catalysts, this

gives rise to the so-called “materials gap”. The pressure gap can be bridged directly by designing high pressure surface techniques such as high-pressure sum frequency generation (SFG), high-pressure scanning tunneling microscopy (STM), ambient pressure X-ray photoelectron spectroscopy (XPS), and in situ atomic force microscopy (AFM) [12]. In addition, the pressure gap can also be bridged indirectly by theoretical calculations using molecular-based models (e.g. kinetic Monte Carlo calculations, microkinetic models), which first describe the experimental results obtained at low pressures, and then extrapolate this information to high-pressure reaction conditions. The materials gap between model and real catalysts could be bridged by introducing defects and depositing nanoparticles with specific sizes and geometries on model surfaces [13, 14].

Unfortunately, most of the surface science studies were carried out on metal substrates, whereas the information on metal oxides, another one of the most important and widely employed categories of solid catalysts, is still rather scarce [15]. The lack of information on planar model surfaces of metal oxides is due to the inherent experimental difficulties arising from the insulating properties of many bulk oxides, whose low electrical and thermal conductivity resulting in charging or band-bending and cooling problems. In order to tackle these problems, growth of oxide thin films with well-ordered surfaces on conductive substrates has been introduced into surface science studies [16, 17]. And some other analytical methods, such as molecular beam scattering [18, 19] and AFM [20, 21], become active owing to the inherent insensitivity to charge effect.

1.2 Cerium dioxide (ceria, CeO_2)

Cerium, named after the dwarf planet Ceres, is the first element of the lanthanide group with symbol Ce and atomic number 58. Cerium is the most abundant of the rare earth elements, and is about as abundant as copper and nearly three times as abundant as lead in the igneous rocks of Earth’s crust. It easily oxidizes in air at room temperature to form cerium dioxide (CeO_2), which, also known as ceria, crystallizes in the fluorite structure (CaF_2) [22, 23]. Ceria has a face-centered cubic (fcc) unit cell with space group *Fm3m*. The Ce cations are bonded to eight O nearest neighbors while the O anions are tetrahedrally bonded to four Ce nearest neighbors (cf. Figure 1.1).

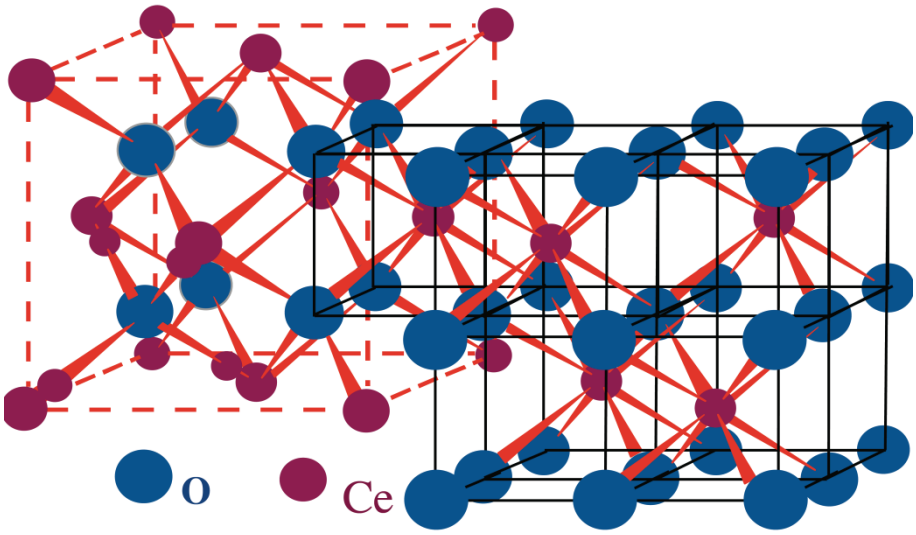

Figure 1.1 The crystal structure of CeO_2. Adopted from Prof. Alessandro Trovarelli's presentation at MCE-2015.

Ceria is a wide band-gap semiconductor. The band-gap lies within the range of 5.5–6.0 eV [24-27]. The valence band and conduction band are formed predominantly by O2p and Ce5d states, respectively [28]. Ce4f states, which are unoccupied in the defect-free bulk material, are located within the band gap. Due to resolution limits, it is difficult to experimentally determine the degree of localization of these f states, but they are assumed to be localized [29]. The energy difference between the lowest unoccupied 4f state and the valence band maximum (VBM) was experimentally found to be around 3.0 eV [25, 30].

Ceria is one of the most reducible metal oxides [31]. It is possible to accommodate a large number of mobile oxygen vacancies by removing oxygen atoms from CeO_2, which can either be removed from the bulk by annealing with subsequent diffusion to the surface [32], or directly from the surface by annealing [33], sputtering [34], electron irradiation [25], exposure to X-rays [35], or chemical reduction [36]. Calculations have indicated that the oxygen vacancy formation energy, which is related to the reducibility, is approximately 30% lower on ceria surfaces compared to the bulk [31, 37, 38]. Upon one oxygen vacancy formation, there would be two excess electrons left behind, which can be accommodated in localized Ce4f orbitals of two cerium sites driving the Ce^{4+} to Ce^{3+} reduction (c.f. Figure 1.2). Thus, in the valence band photoemission spectra of reduced surfaces, a peak at a binding energy of 1.2–1.5 eV above the top of the O2p in the band gap is assigned to emission from the Ce4f states [27, 30, 34, 39, 40].

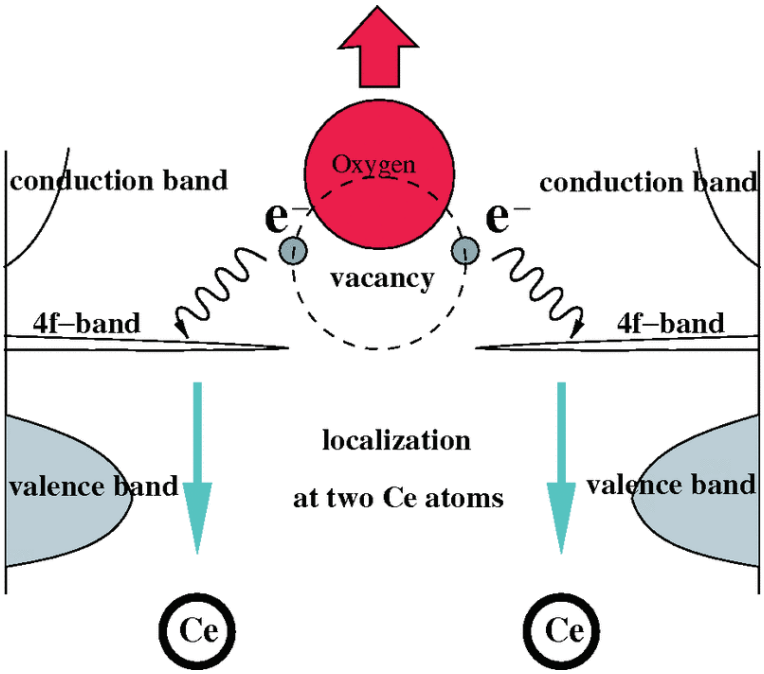

Figure 1.2 The process of oxygen vacancy formation in ceria. An oxygen atom moves away from its lattice position leaving behind two electrons, which localize on two cerium atoms, turning Ce^{4+} into Ce^{3+}. Adopted from [41].

Scientists at Ford Motor Company in 1976 first envisaged the key role of an oxygen storage component in the formulation of three-way catalysts [42]. Since then ceria has evolved from an almost unknown oxide of the rare earth family to become one of the major players in the catalysis game. The ability of ceria to rapidly switch its average oxidation state in a suitable temperature range, while maintaining structural integrity, is the key to its widespread applications. A great amount of research from fundamentals to applications has been devoted to ceria over the past forty years. The history has been tracked from the seminal review article by Trovarelli in 1996 [43] through two subsequent books in 2002 [44] and 2013 [45]. In the most recent overview Delgado et al. identified many catalytic applications of ceria-based materials [46] with respect to hydrogen production, pollution abatement, and chemical manufacturing. Organic syntheses catalyzed by ceria and related materials that involve more complex reactants and products have been reviewed by Vivier and Duprez [47]. Of these various applications the use of ceria in automotive three-way catalysts (TWCs) has been the most classical and unquestionably the most technologically successful.

Although the "surface science approach" has proven extremely successful to gain fundamental information about the interactions between adsorbates and surfaces, it is only in recent decades that surface science studies on cerium oxide have been coming into their

own [48]. Ceria has three stable low-index crystallographic faces, (111), (110) and (100), which expose cerium cations and oxygen anions with different coordination environments. The ability to adsorb or give up oxygen varies from surface to surface on which redox type reactions are likely to be different. Additionally, the chemistry of the same adsorbate proceeding on a fully oxidized CeO_2 surfaces may be substantially distinct from that on reduced ceria surface due to differing oxidation states of surface cerium cations. Therefore, thorough surface science studies on cerium oxides need to be done on both oxidized and reduced surfaces along all three low-index orientations.

In this thesis, the surface chemistry of various ceria surfaces of single crystals, films and nanocrystals were studied systematically by using primarily ultra-high vacuum Fourier transform infrared spectroscopy (UHV-FTIRS) in combination with other spectroscopic techniques including X-ray photoelectron spectroscopy (XPS) and near-edge X-ray absorption fine structure (NEXAFS) spectroscopy. Our studies focused on the surface atomic and molecular composition, the geometric and electronic structure, as well as the dynamics and energetics of adsorption, desorption and surface reactions. Our collaborators carried out first-principles calculations to help interpret the experimental observations. It is worth noting that computational studies had been limited by the inability of traditional DFT methods to adequately describe the reduced CeO_{2-x}. Upon the removal of one surface neutral O, two excess electrons are left behind and deposited in the 4f orbitals of cerium. DFT delocalizes these electrons through Ce in the substrate producing a fractional occupation of the 4f orbital with a metallic ground state [49]. Recent advances have largely overcome this obstacle and there are two extensive reviews covering computational studies on ceria [49, 50].

The three low-index faces of cerium oxide are prototypical examples of three types of ionic crystal surfaces whose stability was considered by Tasker [51]. CeO_2(110) is a nonpolar surface with stoichiometric proportions of anions and cations in each plane, which results in zero dipole moment perpendicular to the surface (type 1, see Figure 1.3a). CeO_2(111) is also a nonpolar surface, since along the [111] direction each plane is charged but a neutral three-plane repeat unit causes no net dipole moment (type 2, see Figure 1.3b). Both nonpolar (110) and (111) surfaces should have relatively low surface energies, thereby inducing surfaces with only modest relaxations compared to their respective bulk truncation. A bulk truncation along CeO_2(100) creates a type 3 surface. In the bulk crystal, (100) planes are composed alternately of oxygen and cerium ions, leading to an unbalanced dipole at the

surface (Figure 1.3c). A straightforward way to eliminate the dipole moment is to remove half of the O anions in a checkerboard style from the top surface and place on the bottom surface.

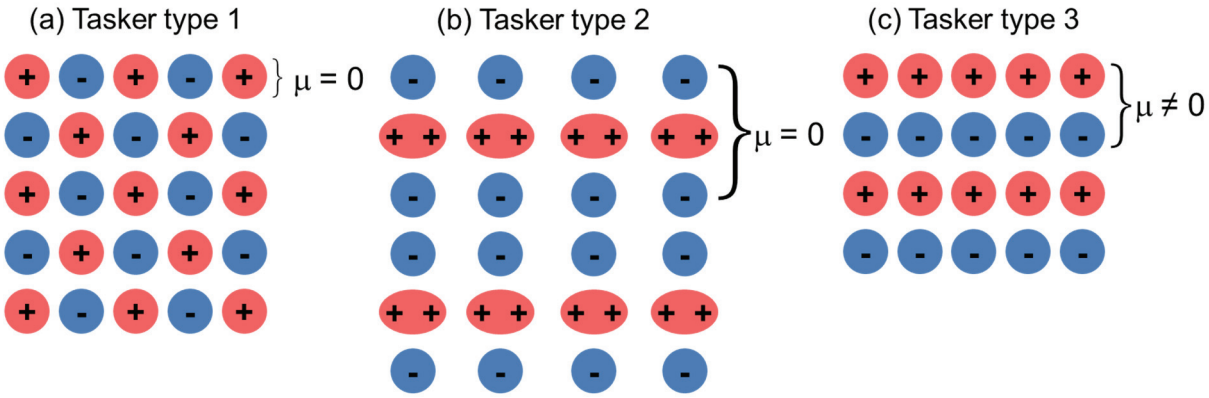

Figure 1.3 Schematic Tasker classification for low-index crystal surfaces of CeO_2 [51]. μ – electric dipole moment associated with the lattice repeat unit.

The structure and stability of these three low-index surfaces of cerium oxide has been theoretically studied in the past few decades [37, 52-60]. While the methods and absolute results may vary, the general consensus is that stability of these three surfaces (as reflected by surface energies) runs as (111) > (110) > (100). The surface energies decrease by relaxation with a contraction between the first and second layers, and the degree of relaxation runs in the reverse order of the surface energies. As for reducibility, the most stable (111) surface has the highest oxygen vacancy formation energy, while the value for (110) surface is the least, which is even lower than that of the polar (100) surface, suggesting that (110) is the most reactive surface [49, 50].

1.2.1 CeO_2(111)

Experimental studies of CeO_2(111) by low energy electron diffraction (LEED) [61-64], ion scattering [39] and STM/AFM [61-63, 65-71] have determined its oxygen termination and are consistent with the surface structure depicted in Figure 1.4. Scanning probe microscopy (SPM) micrographs of the (111) surface demonstrate the expected lattice constant and hexagonal symmetry. In addition, a hexagonal (1×1) LEED pattern was also observed.

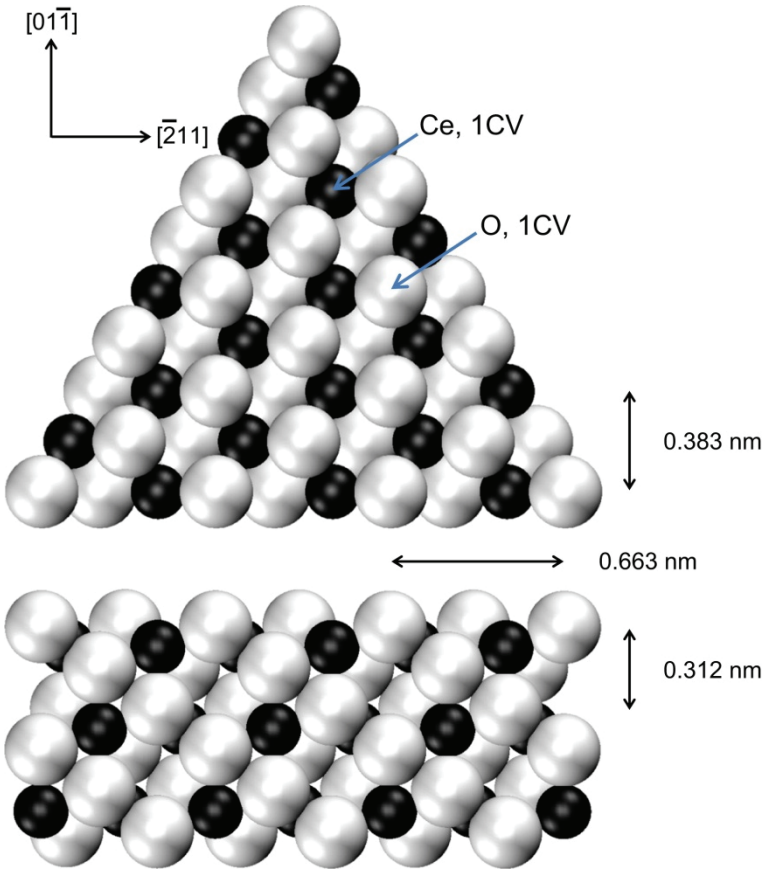

Figure 1.4 CeO_2(111) surface structure. The black spheres are Ce and the white spheres are O. CV refers to the number of coordination vacancies around the Ce in the second layer and O in the top layer. Adopted from [48].

1.2.2 CeO_2(110)

Nörenberg and Briggs investigated the surface structure of single crystal CeO_2(110) by low energy electron diffraction (LEED), reflection high energy electron diffraction (RHEED), and high-temperature STM [72]. LEED and RHEED indicated a (2×1) reconstruction upon annealing to 940 °C. Meanwhile, STM showed line features running along the [1-10] direction separated by 11 Å. Referring to Figure 1.5, these lines are along the rows of Ce cations, and the separation is equal to twice the distance between Ce rows in the [001] direction. By analogy with STM structures observed on the UO_2(110) surface [73], Nörenberg and Briggs inferred that the surface reconstruction was possibly due to "missing rows" of both oxygen and cerium. Further annealing to 1030 °C leads to widening of these missing rows indicative of (111) facet formation, an interpretation confirmed by RHEED. This faceting is similar to that observed on (110) surfaces of some metal substrates [74, 75].

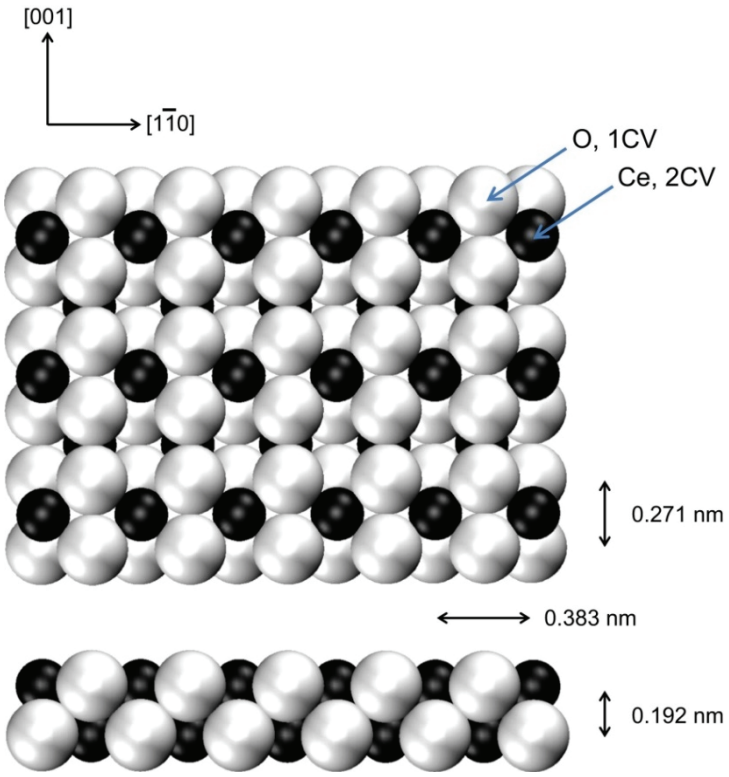

Figure 1.5 CeO_2(110) surface structure. The black spheres are Ce and the white spheres are O. CV refers to the number of coordination vacancies around the Ce and O ions in the top layer. Adopted from [48].

1.2.3 CeO_2(100)

The structure of polar CeO_2(100) surface is currently still under debate, although extensive studies have been conducted on film and bulk single crystal (100) surfaces, and on ceria nanocubes on which it is believed that (100) facets are predominantly exposed. Square, (1×1) LEED patterns were observed for CeO_2(100) thin films grown on Pd(100) [76] and on $SrTiO_3$(100) [77]. However, these authors made no claim as to surface termination. Overbury and coworkers performed angle resolved low energy alkali ion scattering experiments [78]. The incident angle dependence was consistent with that expected for unreconstructed (100) but with a mixture of both oxygen and cerium terminated surface regions. Kim et al. reported the results of direct recoil spectroscopy and low energy ion scattering measurements, which suggested that the CeO_2(100) surface was predominantly terminated by O [77]. Based on results from direct recoil scattering cross sections and angle resolved mass spectroscopy of recoil ions, Herman proposed a reconstructed model of (100) surface with half of the outermost surface O removed in a checkerboard style as depicted in Figure 1.6 [79]. Yang et al. imaged CeO_2(100) thin films grown on oxidized Cu(111) by

STM [80]. However, they were using a positive sample bias which imaged the Ce cations. Therefore they could not come to any conclusion about the termination or O structure. STM studies of single crystal CeO_2(001) by Nörenberg and Harding [81] revealed a √2/2(3×2)R45° surface reconstruction. After exposing the reconstructed CeO_2(001) surface to air and annealing, a c(3×3) surface reconstruction was observed [81]. Lin et al. investigated the atomic structures of ceria nanocubes exposing predominantly (100) surface adopts a mixture of Ce, O, and reduced CeO terminations [82]. They also noted a pronounced tendency of these atoms to hop along the surface.

Overall, a definite structure for the CeO_2(100) surface may not exist due to small energetic differences between different surface models allowing various terminations that may be in constant flux. However, we can conclude that this surface is not terminated by a full layer of Ce or O atoms as obtained from simple bulk truncation.

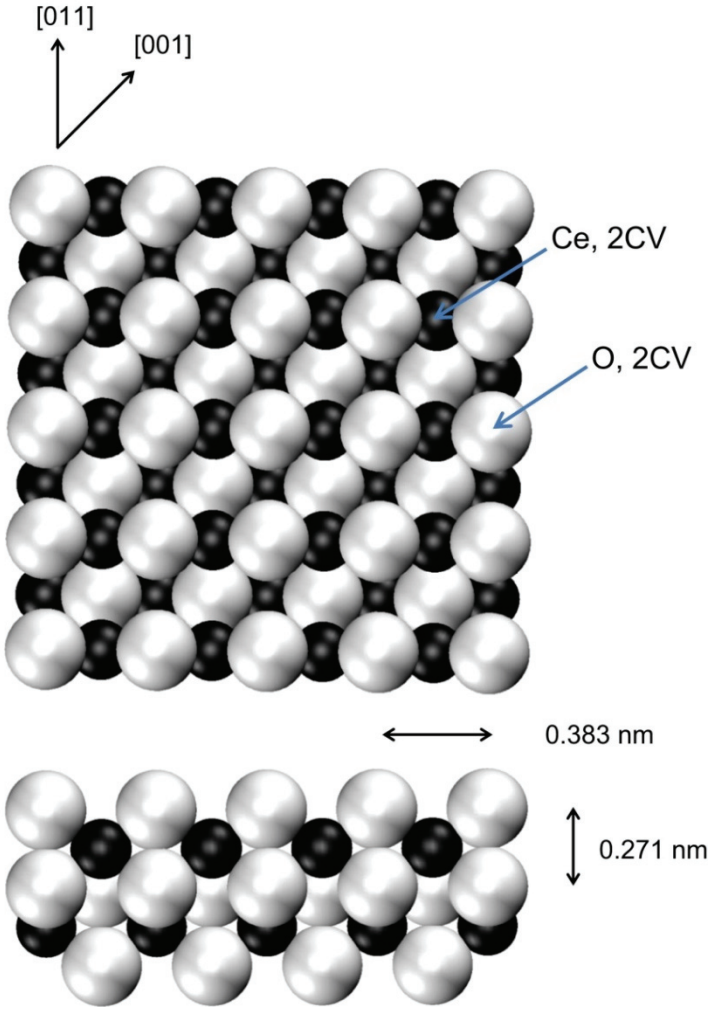

Figure 1.6 Reconstructed CeO_2(100) surface structure. The black spheres are Ce and the white spheres are O. CV refers to the number of coordination vacancies around the Ce in the second layer and O in the top layer. Adopted from [48].

1.3 Organization of this thesis

In this thesis, I will present a thorough spectroscopic study of surface chemistry on ceria surfaces. Considering extensive applications of ceria in heterogeneous catalysis, the adsorption of various C1 molecules (CO, CO_2, CH_3OH) on ceria single crystals and nanocrystals was studied by ultra-high vacuum Fourier transform infrared spectroscopy (UHV-FTIRS) or near-edge X-ray absorption fine structure (NEXAFS) spectroscopy with the support of the core-level and valence band X-ray photoelectron spectroscopy (XPS), low energy electron diffraction (LEED), and first-principles calculations. Chapters 2 and 3 briefly review the experimental techniques and setups. Chapter 4 reports IRRAS data of CO adsorption on all three low-index surfaces of cerium oxide, which subsequently are compared with the results for ceria films. We demonstrate that CO, as the most frequently used IR-probe molecule, is capable of probing surface oxygen vacancies and distinguishing facet orientations. Chapter 5 presents IR results of CO adsorption on ceria nanocrystals (conventional particles, rods, cubes). Based on the IRRAS data for various ceria single crystal surfaces, detailed insights into the atomic surface structure of CeO_2 nanocrystals are obtained. Our IR results reveal that oxide nanocrystals are not always perfectly structured, but are of rather complex nature and contain surface reconstruction, nanofaceting and surface vacancies, which is in contradiction to previous assumptions. Chapter 6 presents IRRAS data of methanol adsorption on bulk single crystal CeO_2(111) and (110) surfaces, which clarify the ambiguous assignments of methanol IR-bands derived from previous ceria powder and thin film data. In chapter 7, data of CO_2 adsorption on CeO_2(110) surface provides the final piece of the jigsaw for the NEXAFS study of CO_2 on ceria single crystal surfaces, where the charge transfer between reduced CeO_{2-x}(110) and adsorbed CO_2 molecules is experimentally observed, thereby settling the controversy over whether the reduced ceria can be re-oxidized by CO_2.

2 Theory background of techniques

2.1 Infrared spectroscopy

Infrared spectroscopy is one variant of vibrational spectroscopy that deals with the infrared region of the electromagnetic spectrum, which is light extending from the nominal red edge of the visible spectrum at 700 nm to 1 mm. Infrared spectroscopy is one of the most important and widely used analytical techniques available to scientists working in a whole range of fields. One of the great advantages of infrared spectroscopy is that virtually any sample in virtually any state may be studied. Liquids, solutions, pastes, powders, films, fibers, gases and surfaces can all be examined with a judicious choice of sampling technique [83, 84].

The instrument used for these spectroscopic measurements is called infrared spectrometer. A basic IR spectrum is essentially a plot of infrared light absorbance (or transmittance) as a function of wavenumber, which is defined as the inverse of the wavelength

$$\tilde{\nu} = \frac{1}{\lambda} = \frac{\nu}{c}$$

where wavelength λ is in units of cm, ν is the frequency, c is the speed of light in vacuum (3×10^{10} cm/s).

Infrared radiation covers a wavenumber range from about 12800 to 10 cm^{-1} comprised of near-infrared (NIR, 12800 to 4000 cm^{-1}), mid-infrared (MIR, 4000 to 400 cm^{-1}) and far-infrared (FIR, 400 to 10 cm^{-1}). Among them, the mid-infrared region is of greatest practical use, as the vibrations and rotations of most molecules can be excited with radiation of these frequencies. All infrared spectroscopic measurements carried out in this work are exclusively in the mid-infrared range.

Infrared spectroscopy exploits the fact that transitions between discrete vibrational and rotational states of a molecule can take place by absorption of infrared radiation, when the frequency of the absorbed radiation matches the transition energy of the bond or group in motion. Consequently, different functional groups absorb light at different characteristic frequencies and the resulting IR spectrum can be seen as the fingerprint of a substance.

The vibrational excitation in IR can occur only if the general selection rules are satisfied.

A vibration is IR-active, i.e. a corresponding band in IR spectroscopy is observed, when the electric dipole moment of the molecule changes during the vibration. Hence the stretching modes of symmetric diatomic molecules like N_2 and O_2 cannot be observed by IR spectroscopy, which yet are Raman-active due to a change in the polarizability of the molecule. Therefore, Raman spectroscopy can be used as a complementary method to IR spectroscopy.

The change in the molecular dipole moment induced by a vibration resulting in a so-called transition dipole moment (TDM), which is the physical basis for the interaction of the electric field of the incident infrared light with matter. The interaction reaches a maximum when the frequency of the vibration and the exciting radiation are identical and the direction of TDM and of the exciting radiation are the same.

The electrons in the chemical bond act like a classic spring between the nuclei. The plot of the potential energy of the molecule versus the distance between the nuclei is called potential curve (cf. Figure 2.1). The oscillation of the nuclei can be described in a first approximation as the oscillation of point masses in a harmonic potential. The following Schrödinger equation has to be solved

$$-\frac{\hbar}{2\mu}\frac{\partial^2}{\partial x^2}\Psi(x) + \frac{1}{2}kx^2\Psi^2 = E_{\mathrm{v}}\Psi^2$$

where k is the force constant, $\mu = (m_1 m_2)/(m_1 + m_2)$ the reduced mass, and x the deviation from the equilibrium. The corresponding energy levels E_n, obtained from the solution of the Schrödinger equation, are equidistant and are given by

$$E_{\mathrm{v}} = h\nu(\mathrm{v} + \frac{1}{2})$$

where h is the Planck constant, ν the frequency, and v the vibration quantum number.

$$\nu = \frac{1}{2\pi}\sqrt{\frac{k}{\mu}}$$

The frequency increases for vibrations of stronger bonds (larger force constant) and decreases for molecules with heavier atoms.

The model of the harmonic oscillator describes molecular vibrations approximately, where only transitions with $\Delta\mathrm{v} = \pm 1$ are allowed and thus overtone and combination vibrations are not included in this model. Moreover, the harmonic oscillator model is invalid to large

deviation from the equilibrium interatomic distance, which excludes the possible description of breaking of the chemical bonds. Therefore, a more realistic model, anharmonic oscillator, for accurate description of molecular vibrations is used, in which the potential energy $V(x)$ is the Morse potential

$$V(x) = D(1 - e^{-\beta x})^2 \text{ with } \beta = \pi\nu(\frac{2\mu}{D})^2$$

where D is the dissociation energy of the vibrating bond.

In this case, the most fundamental correction is the anharmonic distortion of the potential acting on the nuclei (cf. Figure 2.1): for high deflections the potential becomes shallower and finally reaches a limit at the dissociation energy; for contraction of the oscillator the potential becomes considerably steeper due to the Pauli repulsion (electrostatic repulsion alone cannot explain the effect). The anharmonicity produces some measurable consequences that

- The vibrational levels are no longer equidistant. Their distance shrinks as the quantum number v increases. At the dissociation limit the energy levels are close enough to be considered as a continuum.
- Harmonic frequencies, i.e. excitations contradicting the specific selection rules, can be observed in the spectrum (with low intensity). Here for example the transition from v = 0 to v = 2 (overtone) can be detected.
- The average distance of the nuclei is no longer constant and independent of the vibrational quantum number v but increases as a function of the v.

The energy eigenvalues for the anhamonic oscillator are obtained by solving the Schrödinger equation

$$E_{\mathrm{v}} = h\nu_0(\mathrm{v} + 1) - h\nu_0 x_e(\mathrm{v} + \frac{1}{2})$$

where x_e is the anharmonicity constant.

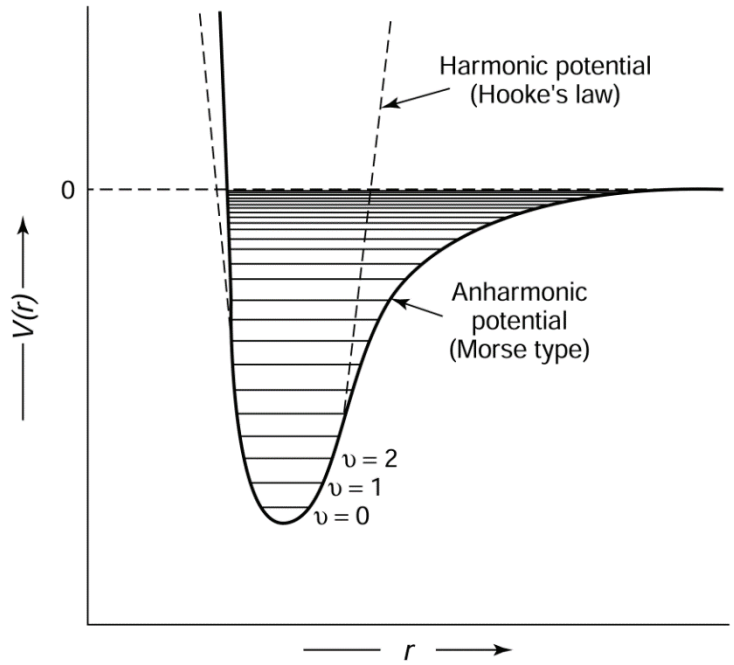

Figure 2.1 Potential energy of a diatomic molecule as a function of the atomic displacement during a vibration for a harmonic oscillator (broken line) and an anharmonic oscillator (solid line). Adopted from [85].

A molecule can vibrate in many ways, and each way is called a vibrational mode. The degrees of freedom of movement for linear polyatomic molecules containing N atoms are 3N-5 and 3N-6 for non-linear molecules. Vibrations involve either a change in bond length (stretching) or bond angle (bending). Figure 2.2 represents different vibrational modes for the atoms in a CH_2 group.

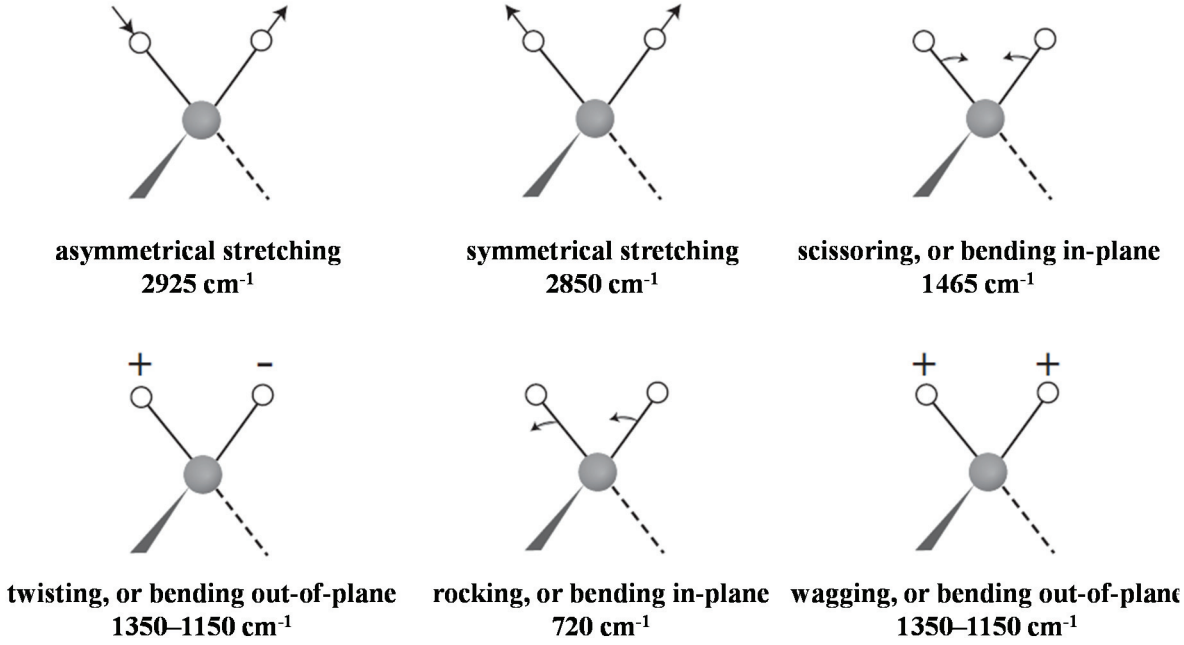

Figure 2.2 Stretching and bending vibrational modes for a CH_2 group. Adopted from [86].

2.1.1 Infrared reflection absorption spectroscopy (IRRAS)

Infrared reflection absorption spectroscopy (IRRAS) is the main technique in this thesis for investigations of interactions between various molecules with cerium oxide single crystals. The IRRAS approach was developed in the 1960s and has proved to be a particularly powerful research tool for the study of adsorbed layers on metal surfaces [87, 88]. Unlike the vibrational excitation of molecules in pure substances by infrared light, the absorption of infrared radiation by a molecule adsorbed on a metal surface is dominated by the dielectric behavior of the metal, since the electric field of the incident light as well as that of the dipole moment of a molecular vibration will interact with the metal electrons. Greenler [88-90] first demonstrated that the metallic surface imposes a strict surface selection rule, which demands that the incident light should have a component parallel to the plane of incidence, i.e. p-polarized, and that only vibrations with component dynamic dipole moment aligned perpendicular to the surface plane will be excited.

Figure 2.3 illustrates the incident and reflected electric vectors of the so-called s and p components of the radiation where p refers to parallel polarized radiation and s to perpendicular polarized radiation with respect to the plane of incidence. The intensity of light reflected from a surface related to phase shift δ upon reflection (cf. Figure 2.4). The p-polarized light almost doubles in amplitude via the vector summation of E_p and $E_{p'}$. Nonetheless, for the s-polarized radiation, the reflected electric vector $E_{s'}$ undergoes a 180-degree phase-shift with respect to incident electric vector E_s, which causes these two vectors cancel each other out and so the net amplitude of the s component by reflection is zero.

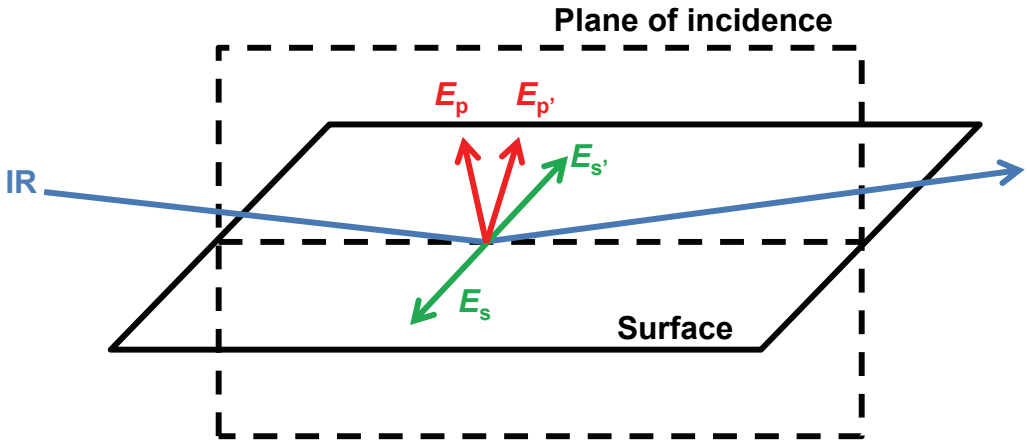

Figure 2.3 Schematic representation of the plane of incidence and the definition of p- and s-polarized radiation in the IRRAS experiment. Reproduced from [91].

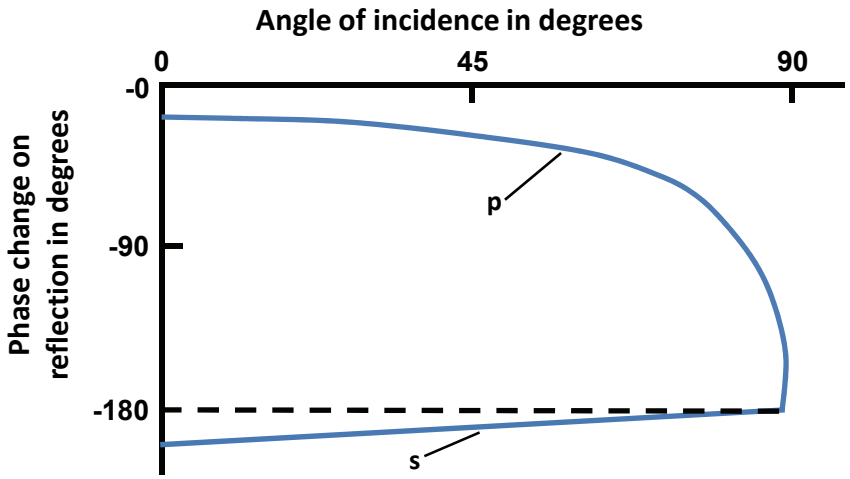

Figure 2.4 The phase shift for light reflected from a metal surface as calculated for light polarized parallel to (p) and perpendicular to (s) the plane of incidence. Modified from [88].

Additionally, considering all angles of incidence, the normal component of p-polarized light that is oriented perpendicular to the surface reaches a maximum near grazing incidence via the use of Maxwell's equations, while the tangential component parallel to the surface has low amplitude, which is relatively structureless as a function of angle of incidence.

Thus the best sensitivity for observing species adsorbed at metallic surfaces in IRRAS can be obtained, when using p-polarized radiation oriented perpendicularly to the surface plane at grazing incidence.

By now there was little in the way of IRRAS studies on metal oxide single crystals. This unfortunate lack of information results from fundamental experimental problems. The two most important causal factors are the absence of an image dipole amplifying the excitations probability for vibrations with their transition dipole moment oriented normal to the metal surface and, second, the strongly reduced reflectivity of an oxide surface at grazing incidence. Together, these two facts result in a large decrease in intensity of IR-active adsorbate vibrations of at least in an order of magnitude relative to metal surfaces. Figure 2.5 exemplifies the problem by comparison of calculated reflectivity differences between gold, a metal substrate, and glass, a dielectric substrate. The aforementioned "surface selection rule" is not applicable on dielectric substrates, and both perpendicular and parallel vibrations of adsorbed molecules can be detected, since s- polarized and p-polarized lights are absorbed and cause a change in reflectivity between the sample and the reference. The reflectivity change (R_0-R_F) induced by adsorbates here is not always positive, but can also be negative,

leading to negative bands in the reflection spectrum, where R_0 and R_F are the reflectivities of the clean substrate and the film-covered substrate, respectively. In the case of s-polarized light, negative bands are predicted by the model calculations in Figure 2.5 over the whole range of incidence angles, which means the reflectivity of s-polarized light becomes larger in the presence of an adsorbate compared to pure substrate (reference). As described above, the s-polarized surface electric field is zero on a totally reflecting metal surface due to mutual cancellation of the incident and reflected electric field vector. In contrast, on dielectric substrates the reflectivity of s-polarized light increases with the incidence angle and with the substrate's refractive index, and the band intensities therefore decrease simultaneously.

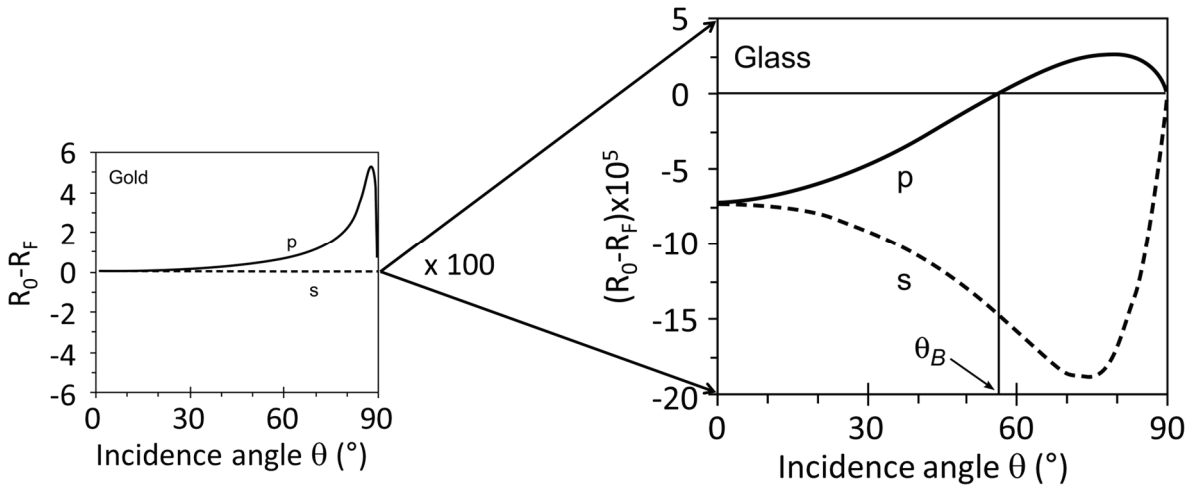

Figure 2.5 Reflectivity of gold compared to glass. Modified from [92].

For p-polarized light, the sign of (R_0-R_F) changes, i.e. it can be positive or negative band in the spectrum depending on the particular substrate and on the incidence angle. A band undergoes an inversion at the Brewster angle (θ_B). Absorption bands point upwards for $\theta > \theta_B$ and downwards for $\theta < \theta_B$ (or vice versa), which is caused by the phase change of the reflected p-polarized radiation from 0° (for $\theta < \theta_B$) to 180° (for $\theta > \theta_B$).

2.2 Low energy electron diffraction (LEED)

LEED is a powerful surface analytic technique for the determination of the surface structure of crystalline materials [93]. The electron energies used in LEED are generally located at 20–500 eV. This is due to the following two reasons. First, the mean free path of electron in solid shows very small value in this energy region, which makes LEED very surface sensitive. Second, in this energy region the wavelength of electron is comparable to lattice constant of solid, which makes LEED suited for studying single crystals.

In LEED experiment, an energy-tunable electron beam bombards on sample surface (in most cases perpendicular to the surface) and is reflected by the sample surface. After filtering inelastically scattered electrons by applying a retarding potential, only elastically scattered electrons are recorded by a fluorescent screen. The elastically scattered electrons form diffraction pattern on the fluorescent screen, which is considered as the reciprocal structure and reflects the periodicity of the sample surface.

LEED is usually used in two ways to study surface structure: LEED pattern and LEED IV-curves analysis. From LEED pattern one can check the surface quality and periodicity. Surface reconstruction or superstructure formed by adsorbates can also be well monitored by LEED patterns. Note that from LEED pattern we can only get the information about surface periodicity, and no any local structure including position and orientation can be deduced from this method. The local structure information of surface can be obtained from LEED IV-curves in which the multi-scattering process of electrons is considered. However, the explanation of LEED IV-curves is a complicated process since prediction and test processes are involved. In this work, the structures of different oxide surfaces are checked only by recording LEED patterns with a microchannel plate LEED (MCP-LEED).

2.3 X-ray photoelectron spectroscopy (XPS)

X-ray photoelectron spectroscopy (XPS), also referred to as electron spectroscopy for chemical analysis (ESCA), is the most widely used surface analysis technique for identifying chemical elements and their chemical states [94, 95]. XPS analysis is based on the photoelectric effect, where the photon source is X-rays of constant wavelength. Photons penetrate into material and excite electrons from the core levels to vacuum states. The kinetic energy distribution of the emitted photoelectrons (i.e. the number of emitted photoelectrons as a function of their kinetic energy) can be measured using an electron energy analyzer, and a photoelectron spectrum can thus be recorded. The process of photoionization can be considered in this way

$$A + photon \rightarrow A^{+} + e^{-}$$

Conservation of energy then requires that

$$E(A) + h\nu \rightarrow E(A^{+}) + E(e^{-})$$

Since the electron possesses solely *kinetic energy (KE)*, the above equation can be rearranged to give the following expression for the *KE* of the photoelectron

$$KE = h\nu - (E(A^{+}) - E(A))$$

The final term in the bracket, representing the difference in energy between the ionized and neutral atom, is generally called the *binding energy (BE)* of the electron. This then leads to the following equation

$$KE = h\nu - BE$$

The *BE* is now taken to be a direct measure of the energy required to remove the electron from its initial level to the vacuum level, and the *KE* of the photoelectron is again given by equation above. In case of a solid sample, because the photoelectrons are measured with an analyzer, the work function should be also taken into account. The work function is the minimum energy required to remove an electron from the Fermi level of a solid to the vacuum level. Hence the equation above is changed into the following form

$$KE = h\nu - BE - \Phi$$

where Φ is the work function difference of sample and analyzer.

Since the work function, Φ, can be compensated artificially, it is eliminated or calibrated, giving the binding energy as follows

$$KE' = h\nu - BE$$

where

$$KE' = KE + \Phi$$

The basic principles of XPS are illustrated in Figure 2.6.

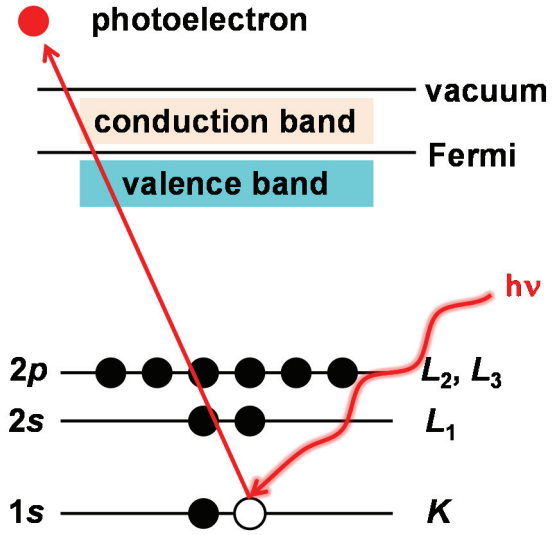

Figure 2.6 Principles of X-ray photoelectron spectroscopy (XPS).

The basic requirements for XPS experiments are (1) an X-ray source as a probe; (2) an electron energy analyzer, which can disperse the emitted electrons according to their kinetic energy, and thereby measure the flux of emitted electrons of a particular energy; (3) an ultrahigh vacuum (UHV) condition to enable the emitted photoelectrons to be analyzed without interference from gas phase collisions. Such a system is illustrated schematically in Figure 2.7.

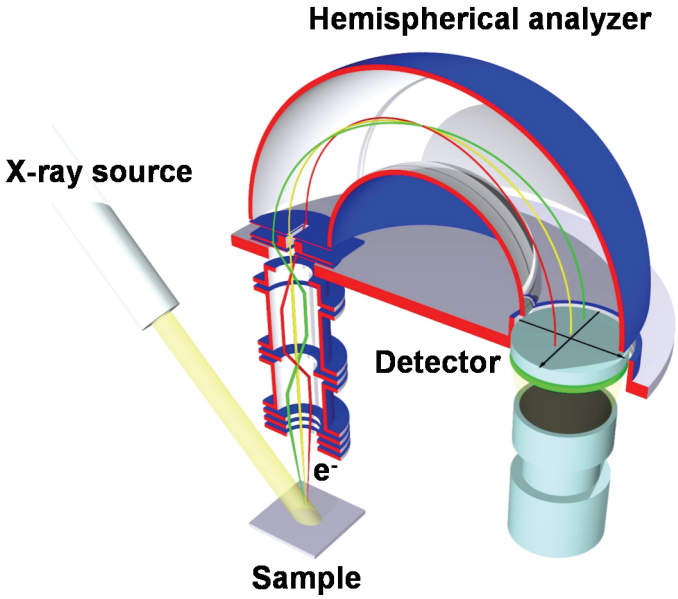

Figure 2.7 The components of X-ray photoelectron spectroscopy (XPS) experimental setup. Modified from [96].

2.4 Near-edge X-ray absorption fine structure (NEXAFS) spectroscopy

(Part of this text is taken from reference [97])

Near-edge X-ray absorption fine structure (NEXAFS), which occasionally is also known as X-ray absorption near edge structure (XANES), is one of the most powerful techniques to explore the electronic and geometric structure of molecules adsorbed on solid surfaces by probing transitions from the innermost shell (K-shell) of an atomic species into unoccupied molecular orbitals [98]. In a NEXAFS experiment, the incident energy of the photons is continuously varied over a certain energy range, and thus this technique clearly requires the availability of a high performance synchrotron source. The method has had its largest success when applied to low Z molecules (Z is the atomic number), for which intense absorption edges are located in the soft X-ray region (100–700 eV).

2.4.1 Theory background

A NEXAFS spectrum presents the photoabsorption cross section as a function of the photon energy, which excites the core electrons to empty states just below ionization threshold, or up to around 50 eV above. Figure 2.8 shows schematically the origin of NEXAFS features for molecular (sub)unit consisting of two atoms. The effective electrostatic potential and the corresponding K-shell spectrum are also shown. Empty molecular orbitals are labelled as π^* and σ^* according to their symmetry. The π^* resonance corresponding to the $1s \rightarrow \pi^*$ transition has a sharp shape in the lower energy region, which can only be observed for molecules with π-bonding (i.e. double and triple bonds or aromatic systems), but not for single bonds. The σ^* resonance or $1s \rightarrow \sigma^*$ transition is a broader feature at higher energies above the absorption edge. Rydberg orbitals give rise to sharp but weak resonances occurring below the ionization threshold. They generally lie between the π^*-resonance and the ionization potential. The width of the resonances depends on the lifetime of the excited states and increases as the final orbitals located higher in the continuum.

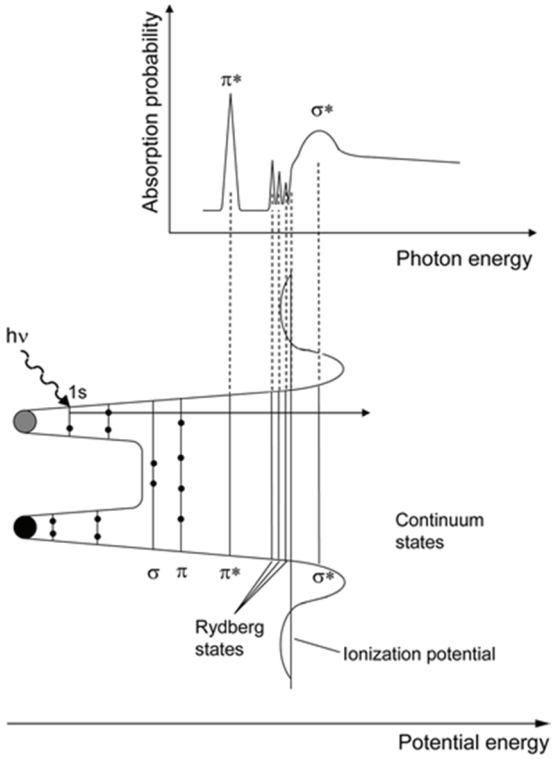

Figure 2.8 Schematic potential (bottom) and corresponding NEXAFS K-shell spectrum (top) of a diatomic molecular (sub)group. Adopted from [99].

In addition to the information on the electronic structure of molecules or molecular fragments, NEXAFS can be used to determine the orientation of a molecule relative to the substrate surface [98, 100]. Bonds and the corresponding molecular orbitals are highly directional and the spatial orientation of an orbital, i.e. the direction of maximum orbital amplitude on the excited atom, determines the angular dependence of the K-shell spectra. Therefore, the transition intensities depend on the orientation of the electric field vector relative to the orientation of the molecule, which will not be discussed in detail here.

2.4.2 Acquisition of the NEXAFS spectra

In the most important variant of NEXAFS spectroscopy used today for the investigation of surface properties, the absorption of X-ray photons is measured by detecting the secondary electrons generated by the decay of the core hole emitted from the sample into the vacuum. While the most direct way to measure the total current would be to use a sensitive amperemeter to measure the total photocurrent generated by the impinging photons as a function of photon energy, in practice it has proven more effective to measure the electrons emitted into the vacuum using electron multipliers or channel plates.

The photoabsorption process taking place when the incident photons hit the sample substrate results in the creation of a photoelectron and a core hole. The hole is subsequently filled by another electron, the corresponding excess in energy is dissipated either radiatively by the emission of a fluorescent photon, or non-radiatively by the emission of an Auger electron (cf. Figure 2.9). Both channels are a direct result of the core hole created in the X-ray photoabsorption process and thus provide a basis to determine the absorption cross section. In principle, either dissipation process can be used for the detection. It is necessary to note, however, that for low-Z elements (C, N, O) the Auger electron yield is much higher than the fluorescence yield (FY), making the electron yield channel better suited for low-Z molecules [101]. In addition, electron detection provides the higher surface sensitivity and in the majority of studies published in the literature this so-called electron yield detection scheme has been employed. The reason for the higher surface sensitivity is the relatively low kinetic energy of the electrons and the corresponding mean free path in solid matter, which is typically less than 1 nm for energies between 250 eV and 600 eV [8]. The inelastic scattering process leads to an electron cascade, of which only those electrons with sufficient energy to overcome the work function of the material will escape the surface. The surface sensitivity can be further enhanced by applying a retarding voltage. By suppressing lower kinetic energy electrons, only those electrons that emerge from the outermost surface region (3 nm) are detected. For the investigation of adsorbates on surfaces, this so-called partial electron yield (PEY) detection has a better signal-to-background ratio than total electron yield (TEY) detection, where all electrons that emerge from the surface are detected. A further option is Auger electron yield (AEY) detection where only elastically scattered Auger electrons are recorded. The AEY mode provides the best surface sensitivity of the three detection techniques, but requires an electron energy analyzer.

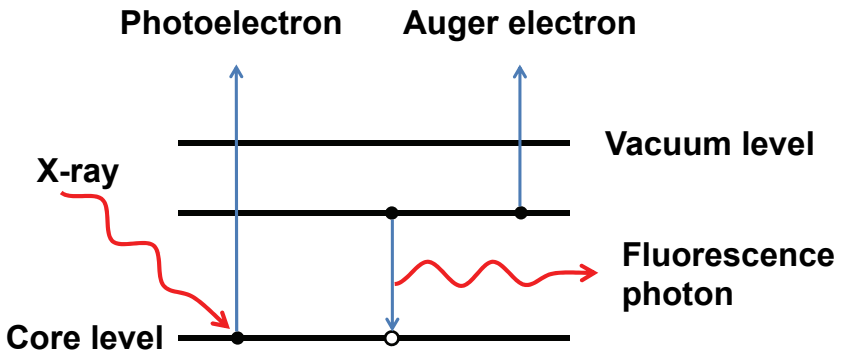

Figure 2.9 Energy diagram of the photoabsorption process and the subsequent filling of the core hole by emission of a photon or an Auger electron. Reproduced from [99].

To extract quantitative information about adlayers on a substrate raw NEXAFS spectra recorded have to be properly normalized. We typically apply the following procedure: first, the constant background signal, present without illumination (dark currents) is subtracted from the spectra. Then the spectrum recorded for the clean substrate is subtracted from the adlayer spectra. The resulting data is then divided by a spectrum recorded for a freshly sputtered gold film to compensate the energy dependence of the transmission function of the beamline. Finally, the intensities are normalized to an edge jump of 1, i.e. intensity difference between 275 and 330 eV in a case of C K-edge. This procedure provides information exclusively on the adsorbed layer.

3 Experimental

3.1 Sample preparation

There are various sample holders available to investigate both single crystal and powder samples. Sample holders are used for transporting of samples to UHV as well as for the heating and cooling treatments. Here the PTS-EB 1200 sample holder (Prevac, Poland, cf. Figure 3.1a) equipped for electron bombardment heating was used for measurements of cerium oxide single crystals. The samples mounted on this sample holder can be heated to 1200 K. The sample holders are mainly composed of molybdenum and tantalum, i.e. metals have a high stability at high temperatures, which meets the requirements for the cleaning of oxide single crystals at high temperatures. Figure 3.1a shows an EB sample holder, where the single crystal needs to be mounted on the heating plate with tantalum clips and the thermal couple (type K) is also attached on the sample surface. Figure 3.1b shows the PTS-H/K 1000 sample holder (Prevac, Poland) that is specially designed for IR transmission measurements. This kind of sample holder provides electric resistance heating and is used for our measurements on ceria powder samples. The powder particles are first pressed on a stainless steel mesh of 0.103 mm nominal aperture (Goodfellow, UK) and then mounted on the sample holder. This particular way of mounting powder particles in tiny metal mesh holes allows for maximal efficiency of heat transport between the mesh and the samples, thus resulting in a rapid cooling and heating.

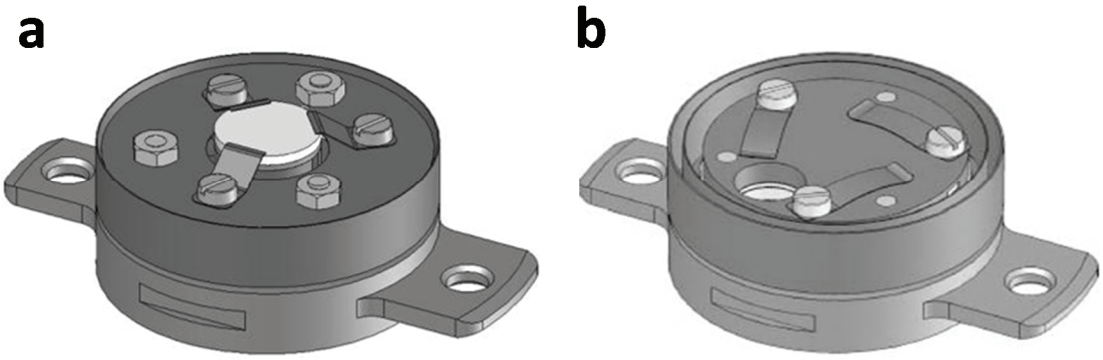

Figure 3.1 The specially designed sample holder (a) PTS-EB 1200 for reflection measurements, and (b) PTS-H/K 1000 for transmission measurements. Taken from the manual of Prevac.

Ceria single crystals (SurfaceNet GmbH, Germany) were prepared by repeated cycles of

sputtering with 1 keV Ar^+ and annealing at 800 K for 15 min in an O_2 atmosphere of 1×10^{-5} mbar for forming a stoichiometric surface, or alternatively without O_2 to create a reduced one. LEED (BDL800, OCI Vacuum Microengineering, Canada) was used to assure a well-defined surface crystallinity of the substrate as judged from sharp spots in the pattern. Additionally, XPS measurements were carried out to ensure sample cleanliness and to determine the oxidation state of cerium from Ce3d photoemission spectra prior to IRRAS measurements. Similarly, synchrotron-based XP spectra of Ce4d and valence bands were recorded before NEXAFS measurements.

Around 200 mg ceria powder particles were pressed into a stainless steel mesh (13 mm in diameter) with a hydraulic press under the pressure of 5 bar, and then mounted on a sample holder (cf. Figure 3.1b). Ceria powder samples were normally annealed at 773 K in the UHV chamber to remove the surface impurities (e.g. water and carbon contaminants) and then also checked with XPS to examine the surface cleanness and the oxidation state of cerium before IR measurements.

3.2 Dosing procedure

For IRRAS measurements of methanol adsorption on ceria single crystal surfaces, samples were cooled down to 120 K with liquid nitrogen or to 85 K with liquid helium. The base pressure of chamber for IR measurements was below 8×10^{-11} mbar. CH_3OH (99.9%, max. 0.002% H_2O, VWR International GmbH, Germany) and CD_3OD (99.8%, Alfa Aesar GmbH, Germany) were additionally cleaned via at least three pump-freeze-thaw cycles. Methanol vapor was introduced by backfilling the IR chamber up to 1.3×10^{-10} mbar using a leak-valve-based directional doser connected to a tube (2 mm in diameter) that terminated 3 cm from the sample surface and 50 cm from the hot-cathode ionization gauge. The actual pressure in front of the sample is about 2-3 orders of magnitude larger than the total pressure in the vacuum chamber displayed by the pressure gauges.

UHV-FTIRS measurements of CO on ceria single crystals, films as well as powders and NEXAFS measurements of CO_2 on ceria (110) single crystals were performed in two different UHV apparatuses. Exposure of the sample to gases was carried out by backfilling the measurement chamber through a leak valve. Exposures are given in units of Langmuir (L) (1 L = 1.33×10^{-6} mbar·s).

3.3 Ultrahigh vacuum apparatus THEO

THEO, manufactured by Prevac (Rogów, Poland), is a development of the UHV-IR apparatus designed at the Ruhr-Universität Bochum [102], which is dedicated to the spectroscopic characterization of oxides, single crystals as well as powders. The innovative design allows combining several surface-sensitive techniques in one apparatus. It is unprecedented that a UHV chamber can be inserted into the sample compartment of a conventional FTIR spectrometer (Bruker VERTEX 80v) to form a compact connection and thereby avoid the loss of beam intensity as little as possible. The construction of the new UHV-IR in Karlsruhe was benefit from Bochum's experience. Compared to Bochum machine, THEO has been equipped with a cryostat at the IR chamber enabling the sample to be cooled down to 60 K with liquid helium. Additionally, the spectrometer is equipped with a polarizer which makes it possible to measure with s- and p-polarized light. The metal oxide surfaces thus can be better examined in particular, as on these surfaces the surface selection rule, unlike metals, does not apply.

The UHV apparatus THEO (cf. Figure 3.2) consists of two big UFO-shaped distribution chambers, which are connected together by a reorientation chamber, and multifunctional chambers, such as load-lock, preparation, infrared, magazine and analysis chamber, are also attached. Here we can carry out additional characterizations by using combined measurement techniques including LEED, XPS, ultraviolet photoelectron spectroscopy (UPS), Auger electron spectroscopy (AES), and thermal desorption spectroscopy (TDS).

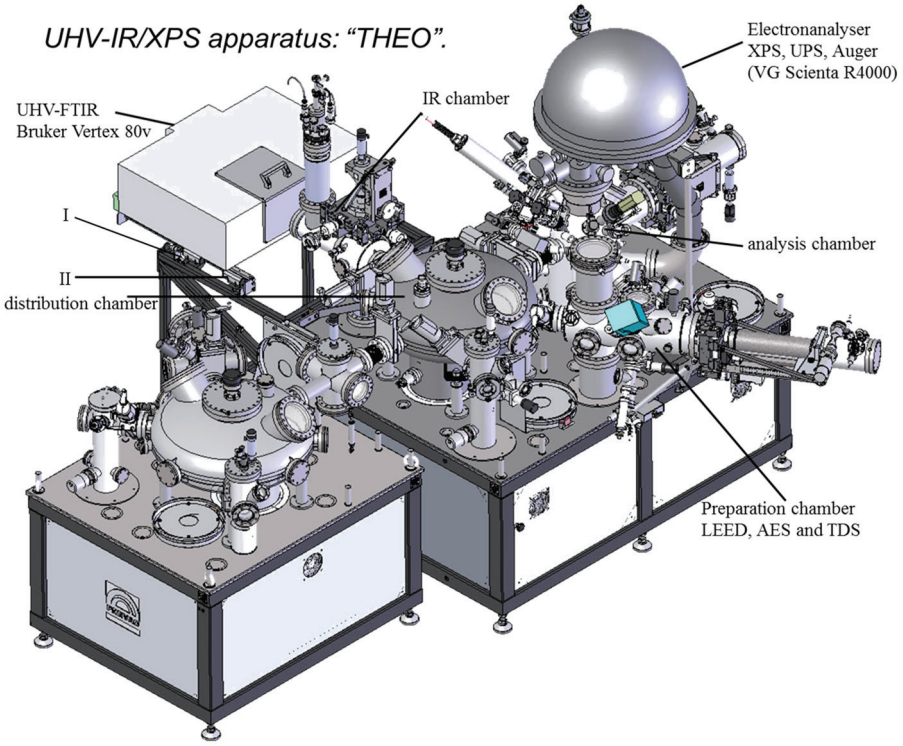

Figure 3.2 Technical drawing of UHV apparatus THEO.

After the single crystal is fixed on the sample holder and all contacts are checked, the sample can be introduced into THEO. For this purpose, one of the two load-lock chambers should be vented first. The venting of load-lock chambers is within 15 minutes, and the pumping down to 10^{-7} mbar possibly needs 7 minutes. One of the load lock chambers is designed for the use of a special transport box, which allows samples to be transported to another system under UHV conditions. Transferring the sample to different UHV chambers attached to the distribution chamber is accomplished via a delicate transfer mechanism, which comprises a rotary feed through with a special gripper allowing for a fast and reliable transport of sample holders between different UHV chambers, each of them separated from the distribution chamber by a gate valve.

In the preparation chamber connected to the distribution chamber 2, the sample can be heated, cooled and sputtered. Vapor deposition of organic molecules and metals is also possible. There is a quartz crystal microbalance sample holder, with which the evaporation rate of substances can be determined. In the preparation chamber connected to the distribution chamber 1, it is possible to directly determine the surface crystallinity and cleanness of single crystal samples by LEED and AES with a high resolution and sensitivity LEED/AES system (BDL800, OCI Vacuum Microenginering, Canada). With a quadrupole mass spectrometer

(RGA 200) of Stanford Research Systems, adsorbate adsorption and reactions on ceria surfaces can be monitored by TDS.

The most striking component of the analysis chamber is an electron energy hemispherical analyzer (Scienta R4000), which is used for various electron spectroscopy methods XPS, UPS and AES. A magnesium/aluminum anode acts as the X-ray source. An electrostatic charging of the sample can be reduced or avoided by bombardment with low-energy electrons (flood gun), so that even poor or non-conducting samples such as polymers and metal oxides can be examined with XPS. HeI or HeII radiation is used as a light source for UPS.

The heart of the UHV equipment is the IR chamber. The unique configuration enables UHV chamber to be directly coupled through differentially pumped KBr window flanges to an intact Bruker spectrometer VERTEX 80v, which has an actively aligned UltraScan interferometer, providing a spectral resolution of better than 0.2 cm^{-1}. Furthermore, the inner part of the spectrometer is evacuated to below 2 mbar. The differentially pumped windows between the UHV chamber and spectrometer sealed by Viton O-rings can be evacuated to a vacuum of better than 1×10^{-6} mbar. Thus, the entire optical path is kept in vacuum/UHV to avoid any absorption from atmospheric moisture and other gas species (e.g. CO_2). In addition, the acquisition of spectra at grazing incidence (80°) of sample substrates kept under UHV conditions is possible without introducing any new optical element in the path of the infrared light. It is considered to be crucial for the high performance of this IR/UHV combination and guarantees high-quality IR data with high sensitivity and long-term stability, which are required to detect the very weak IR bands on single crystalline oxide surfaces.

The samples can be measured in both reflection and transmission modes (cf. Figure 3.3). In order to measure in transmission mode (e.g. powder samples), the sample holder with a hole (cf. Figure 3.1b) is used, and the sample is fixed to cover the hole. During measurements, the sample holder is rotated by 90°, so that the beam after passing through the sample can be incident on the detector. The sample position is determined by a high precision 4-axis manipulator. The spectrometer is, in addition to the internal mid-infrared source (MIR), also equipped with a more powerful external light source. Another important component is the polarizer, with which one can measure using s- or p-polarized light and so it is possible to determine the molecule geometry on the surface. Time resolved step-scan and rapid-scan FTIR measurements can also be carried out in reflection and transmission modes, which can

help in the investigation of kinetic processes. The detector chamber is equipped with two detectors to meet the particular research requirements: a liquid nitrogen cooled mercury cadmium telluride (MCT) detector and a room temperature operated deuterated triglycine sulfate (DTGS) detector. In order to better detect OH vibrations, an indium stibnite (InSb) detector is also occasionally employed, since it is more sensitive in the interesting wavelength range. The MCT detector is the most frequently used one due to its relatively high detectivity (see Figure 3.4).

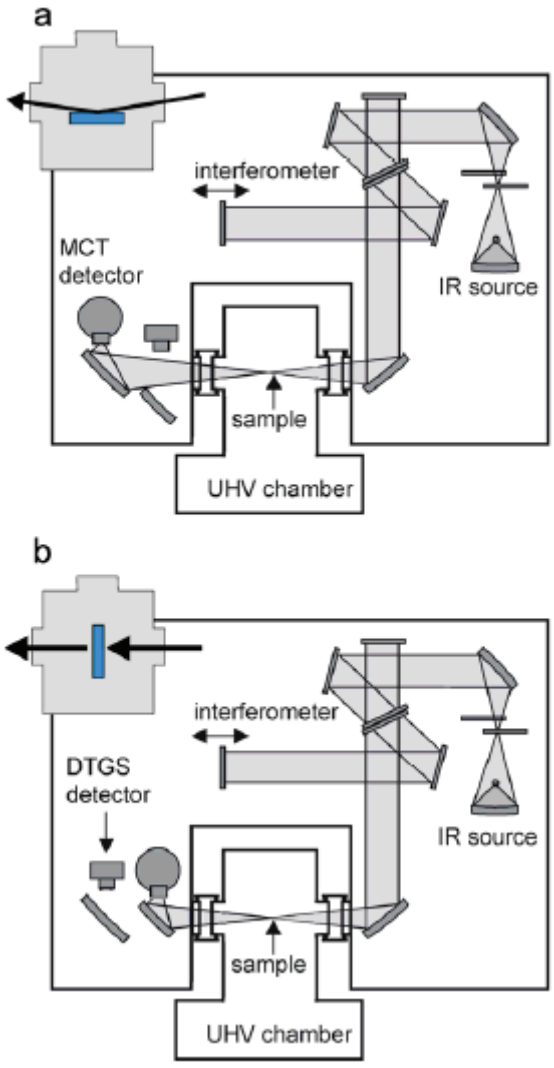

Figure 3.3 Schematic representation of different types of IR measurements: (a) reflection absorption at grazing incidence, (b) transmission. Modified from [102].

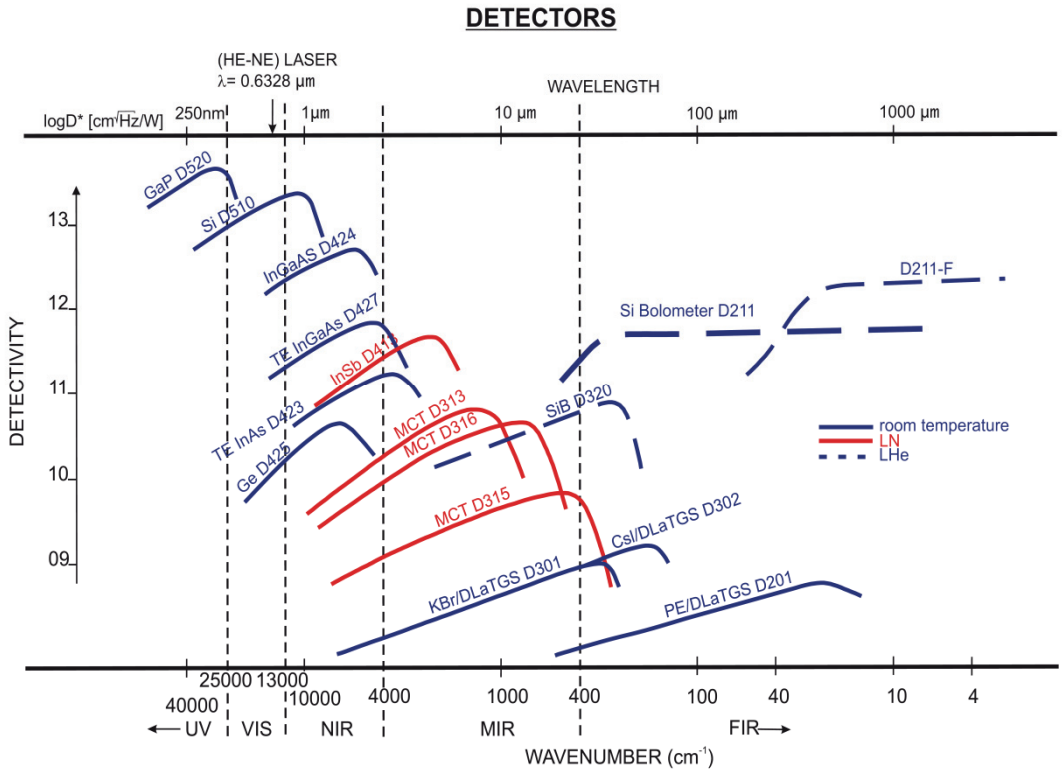

Figure 3.4 Detectivity of different detectors in the IR rang. Taken from the manual of Bruker.

The IR spectrometer is placed on a solid frame equipped with two sliders, permitting to move the spectrometer to two different positions (cf. Figure 3.2). When placed at position I, the IR spectra can be recorded in the conventional mode, i.e. samples can be installed in the sample compartment under ambient conditions and spectra can be recorded after closing the sample compartment as in the normal measurement procedure for the VERTEX 80v instrument. When the FTIR spectrometer is moved to position II, it is directly connected to an UHV chamber. The latter is located inside the sample compartment of the spectrometer and IR spectra can be recorded for samples in the UHV chamber. Having the option to operate the spectrometer at positions I and II was found to be rather crucial for an alignment of the IR spectrometer and for troubleshooting.

3.4 Experimental NEXAFS system

The apparatus used to measure NEXAFS spectra is additionally equipped with complimentary surface analytical techniques, namely XPS/UPS, LEED and TDS. Especially for more complex systems the possibility to characterize samples by additional methods has been shown to be crucial for providing a unique and reliable interpretation of the experimental NEXAFS data. The scheme of such rather complex, multichamber UHV-system used by us is

presented in Figure 3.5. It consists of the analysis chamber (5) for NEXAFS/XPS measurements, the preparation chamber (2) equipped by evaporators (3), ion sputter guns and LEED system (4), a sample transfer system, including the distribution chamber (7) with the park-station (8) and two load lock chambers (1). This NEXAFS/XPS apparatus was designed and built by PREVAC (Poland) and is operated at the HESGM beamline of synchrotron facility BESSY II (Berlin, Germany). A photo of the setup is presented in Figure 3.6.

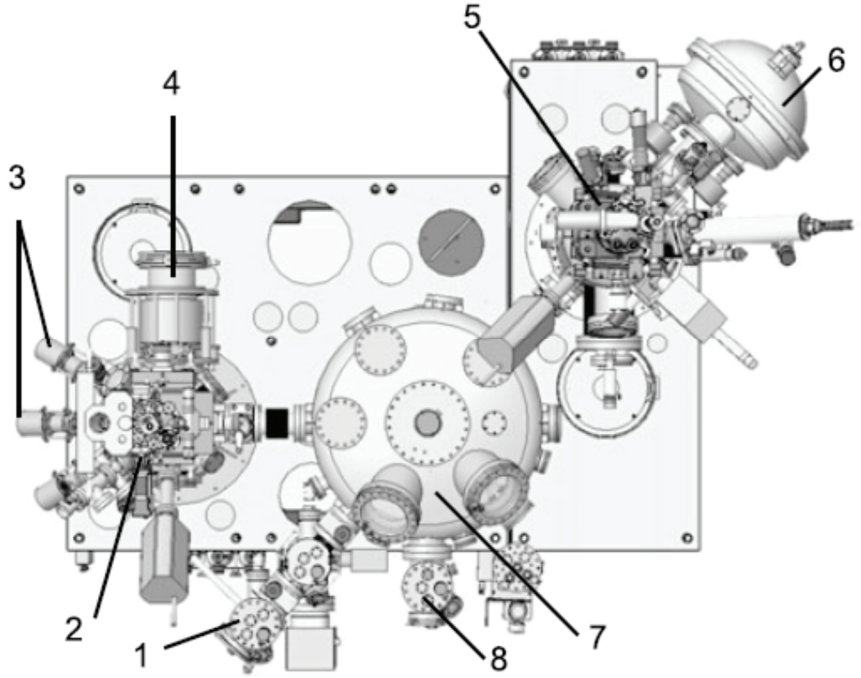

Figure 3.5 The drawing of XPS/NEXAFS system (top view). Adopted from [97].

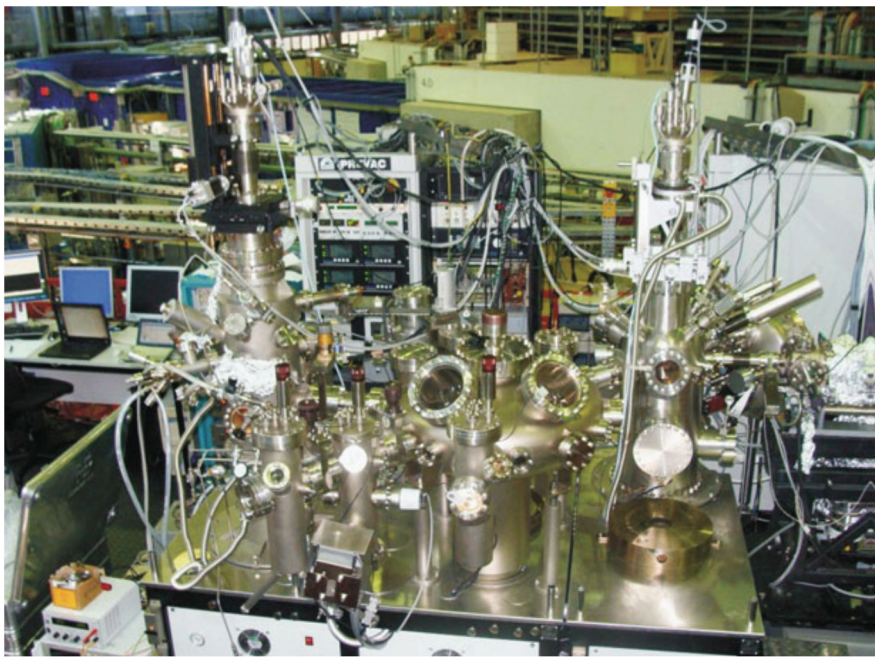

Figure 3.6 The view of XPS/NEXAFS end-station installed on HESGM beamline of synchrotron BESSY II in Berlin. Adopted from [97].

4 Carbon monoxide (CO) adsorption on ceria surfaces

Ceria, one of the most easily reducible materials [50], provides the basis for numerous applications ranging from heterogeneous catalysis (vehicle emission control, ethanol steam reforming [103], water-gas shift reactions [104-106]) over solar thermal hydrogen production from water [107, 108] and to the generation of CO from CO_2 [109]. In all cases, the oxidation reduction cycle (Ce^{4+}/Ce^{3+} cations – and the associated oxygen vacancies) is the most determining factor. The importance of this material has triggered numerous experimental and theoretical studies, in particular aiming at elucidating the properties of oxygen vacancies. Earlier pictures proposing the two electrons left behind by removing an oxygen atom from the surface to be localized at the surrounding cations (i.e. presence of two Ce^{3+} ions adjacent to the defect, see the Ce cations labeled 1 in Figure 4.1) had to be revised later [110] and recent theoretical work has revealed that the remaining electrons are actually localized at some distance away from the vacancy [111-115]. Though it is intuitive to believe that the density of oxygen vacancies may affect the chemical activity of ceria, direct experimental evidence is lacking and even the determination of O-vacancy densities represents a major experimental challenge. The most frequently used approach to determine the concentration of this active site crucial for all redox reactions occurring on this surface is to use carbon monoxide (CO) as a probe molecule and to deduce the nature of the cations it binds to from the frequency of the CO stretch vibration (ν_1). For ceria powder particles, this frequency can be determined conveniently from infrared spectroscopy [116-125]. Typically, the CO stretch frequency shows substantial variations upon changes in the charge state of the metal ion the CO is bound to. In the case of Cu ions, for example, the difference in stretch frequency between CO bound to Cu^{2+} and Cu^{+} amounts to about 70 cm^{-1} [126]. Although a large set of data exists for CO adsorbed on ceria powders, the extent of this shift for Ce-cations is still being discussed quite controversially [127]. For a reliable identification of the frequency shift urgently reference data for ceria single crystal surfaces are needed [128].

4.1 CO adsorption on ceria (111)

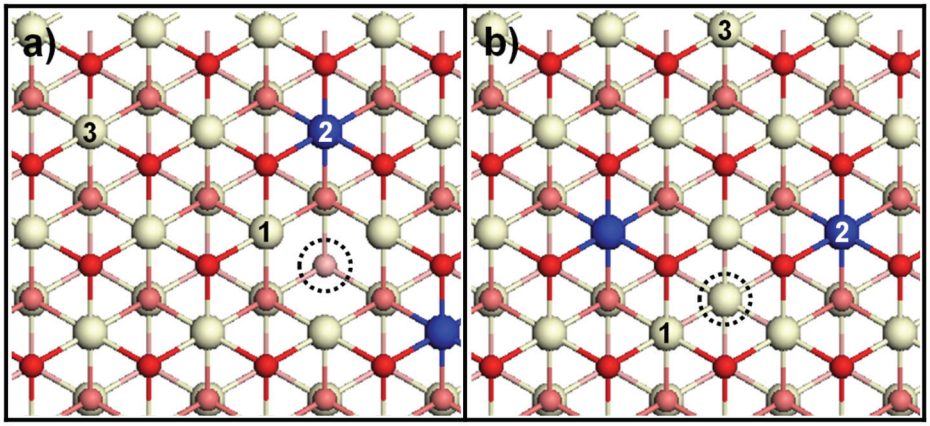

Figure 4.1 Ball-and-stick model of the CeO_2(111) surface (top view) with (a) top- or (b) subsurface oxygen vacancy (V_O). The position of the vacancy is indicated by the dashed circle. Color: red – top surface oxygen, light red – subsurface oxygen, white – Ce^{4+}, blue – Ce^{3+}.

The CeO_2(111) single crystal (SurfaceNet) surface was prepared following the receipt introduced in chapter 3. Exposure to CO at sample temperatures typically below 75 K was achieved by backfilling the IR chamber up to 10^{-9} mbar. The base pressure during acquisition of IR spectra was ~8×10^{-11} mbar. IR spectra were recorded with both s- and p-polarized light incident along the [-110] and [-211] crystallographic directions.

In this chapter, we first determined the stretch frequency of CO adsorbed on a fully-oxidized, single crystalline CeO_2(111) surface ("stoichiometric surface") using infrared reflection absorption spectroscopy (IRRAS). The single sharp band seen in Figure 4.2 indicates that the ν_1 mode for CO adsorbed on the fully oxidized CeO_2(111) surface amounts to 2154 cm^{-1}, thus allowing to correct previous assignments made on the basis of powder data (cf. Table 4.1).

It should be noted that the CO peak is negative, in accordance with IR-data recorded for CO adsorbed on other oxide surfaces [129]. Only a very weak, also negative, feature was observed for s-polarized light.

Table 4.1 Frequencies and assignments of CO bands on ceria powders.

ν (cm^{-1})	Assignments	References
2140	physisorbed CO	[116]
2150 and 2155	CO hydrogen-bonded to OH groups of different acid strengths	
2172	CO interaction with Ce^{4+} sites, but actually "more open surface sites"	
2148	physisorbed CO	[117]
2163	CO adsorbed on Ce^{3+} sites	
2148 (broad)	CO weakly interacting with the Ce^{4+} surface ions	[118]
2151 and 2170	CO on Ce^{4+} cations with different coordinative unsaturation	
2157	CO adsorbed on Ce^{3+} sites	
2140	liquid-like CO	
2145 (shoulder)	liquid-like CO phase	[119]
2159	non-specific interactions	
2169	Lewis centers	
2140	liquid-like CO (tridimensional phase)	[121]
2151–2157	physisorbed CO weakly interacting with the surface (bi-dimensional phase)	
2162–2168	CO coordinated to Ce^{4+} cations	
2143	physisorbed CO at 80 K	[120]
2149	perturbed adsorbed species	
2153–2157	CO bound to $Ce^{4+}(V_O)$, i.e. to Ce^{4+} in the vicinity of an oxygen vacancy	
2169–2176	CO bound to Ce^{4+}	
2148.5–2145.5	very weak interaction of CO with the surface	[122]
2161	$Ce^{3+}(CO)$ surface species	
2169	$Ce^{4+}(CO)$ surface species	
2150	CO adsorbed on Ce^{3+}	[123]
2170	CO adsorbed on coordinatively unsaturated Ce^{4+}	
2170–2150	CO linearly adsorbed on coordinatively unsaturated Ce^{4+} ions	[124]
2127–2120	CO-Ce^{3+} species and electronic transition	
2156	CO linearly adsorbed on Ce^{4+} in a more unsaturated coordination state	[125]
2177	CO linearly adsorbed on Ce^{4+}	
2162	CO on Ce^{3+}	[127]

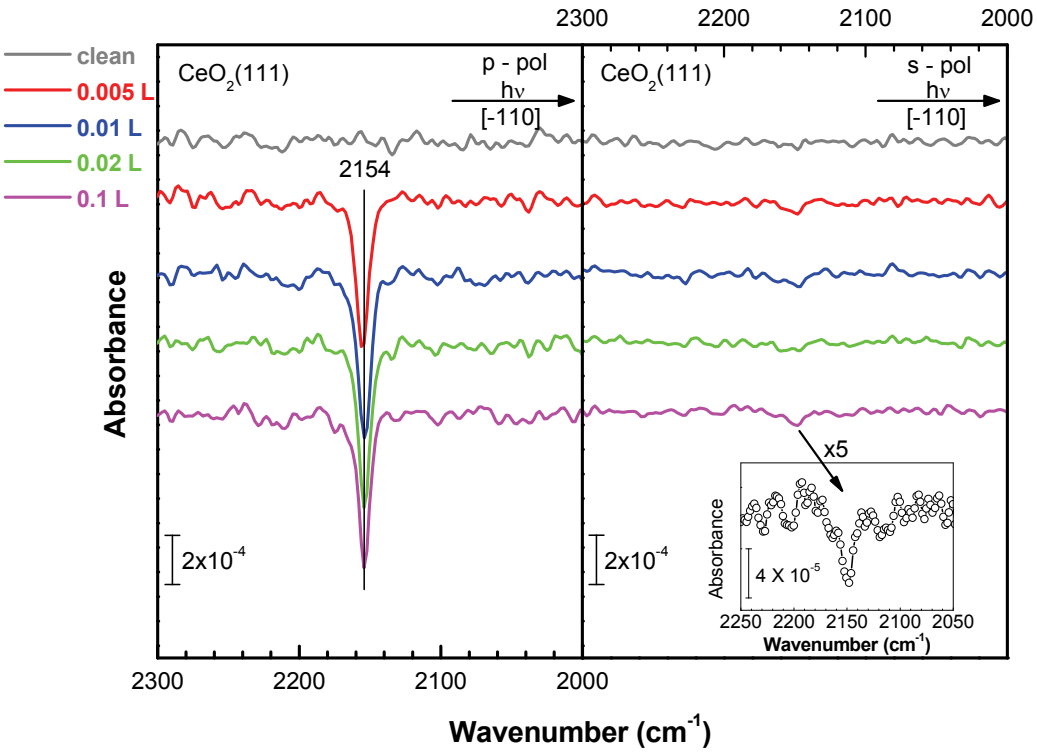

Figure 4.2 Experimental IRRA spectra of different doses of CO at 68 K on stoichiometric CeO_2(111) at a grazing incidence angle of 80° with (left) p- and (right) s-polarized light incident along [-110]. The inset shows a blow-up of the spectral region marked with an arrow.

In a next step, we deliberately introduced oxygen vacancies on the CeO_2(111) surface ("reduced surface"). The concentration of Ce^{3+} within the reduced CeO_{2-x}(111) surface can be determined from the fitting of XPS (cf. Figure 4.3). The Ce3d XP spectrum was fitted with ten peaks and the labels follow the convention established by Burroughs et al. [130], in which u and v refer to the $3d_{3/2}$ and $3d_{5/2}$ spin-orbit components, respectively. The u‴, u″, u, and v‴, v″, v peaks are attributed to Ce^{4+} final states, while the u′, u_0 and v′, v_0 are attributed to Ce^{3+} final states [131]. We fixed the peak positions based on the assignments of Preisler and coworkers [132]. Note that the contribution of the v_0 and u_0 peaks for Ce^{3+} can be disregarded in the spectrum with low Ce^{3+} ion concentrations [133].

$$Ce(III) = v' + v_0 + u' + u_0 \quad (4.1)$$

$$Ce(IV) = u''' + u'' + u + v''' + v'' + v \quad (4.2)$$

$$Ce(III) = \frac{Ce(III)}{Ce(III) + Ce(IV)} \quad (4.3)$$

The density of surface oxygen vacancies (V_O) on the reduced surface are determined as approximately 9% following the above equations [27].

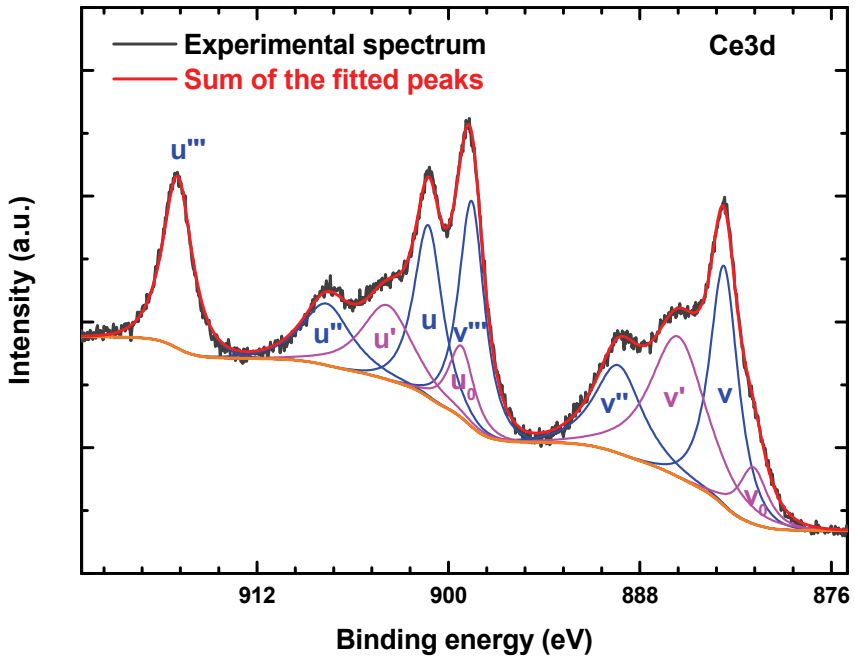

Figure 4.3 Fitted Ce3d XP spectrum of the reduced CeO_{2-x}(111).

For CO adsorption on the reduced surface, the data shown in Figure 4.4 clearly reveal the presence of a new species at 2163 cm^{-1}. Almost identical results were obtained for the [-211] azimuthal direction (not shown).

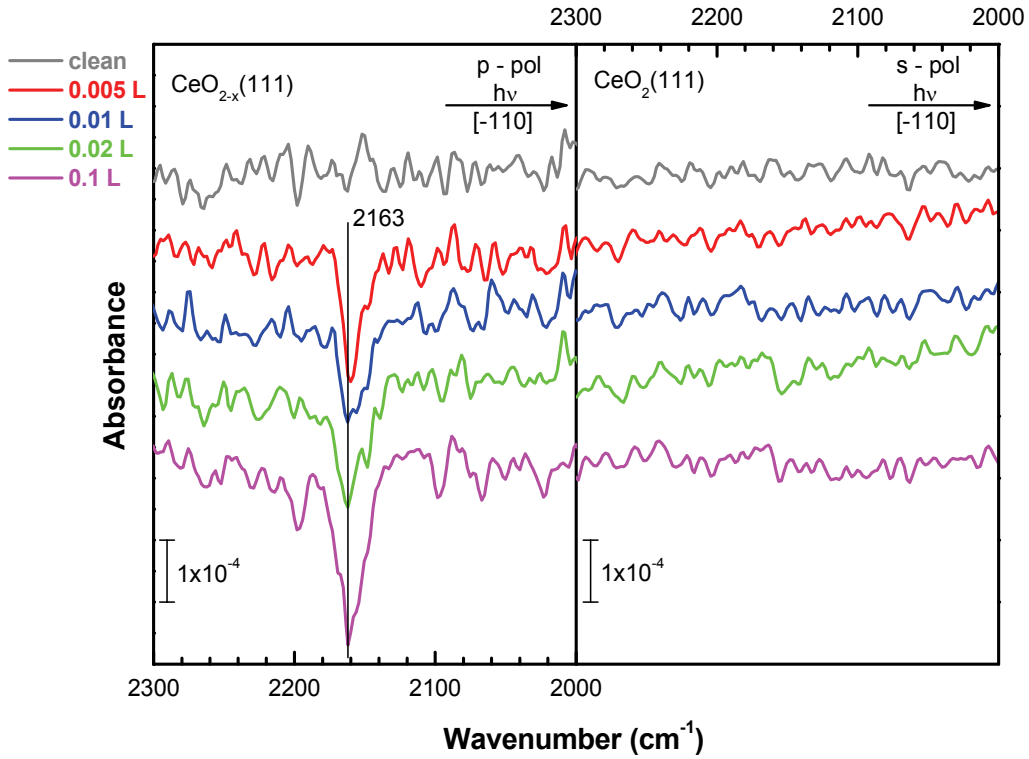

Figure 4.4 Experimental IRRA spectra of different doses of CO at 74 K on reduced CeO_{2-x}(111) at a grazing incidence angle of 80° with (left) p- and (right) s-polarized light incident along [-110].

IR-spectra recorded at different temperatures (cf. Figure 4.5) allow determining the binding energy of the two different CO species – a quantitative analysis using Redhead's equation [134] yields 0.27 eV and 0.31 eV, for the ideal and the defective site, respectively [135].

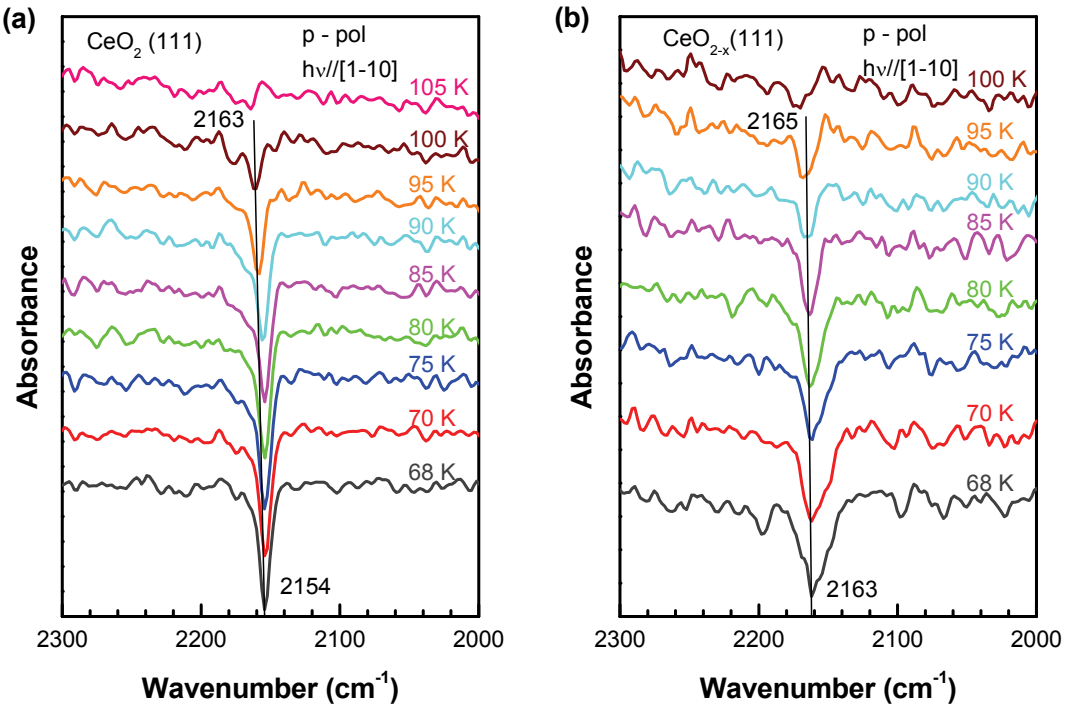

Figure 4.5 Experimental IRRA spectra recorded directly after dosing of 0.1 L CO at ceria surfaces (lowest traces). The samples were gradually heated and spectra were recorded at the temperatures indicated. (a) CO on fully oxidized ceria surface, (b) CO on reduced surface.

The blue-shift of around 10 cm^{-1} in the stretch frequency of the CO bound to the defect-induced surface is unusually small. In addition, it is surprising to observe a blue-shift for CO bound to a defective site, as on other oxides like TiO_2 the increased binding energy at defect sites (which is also observe here) is accompanied by a red-shift in frequency. In order to better understand the origins of this unexpected behavior and to assign the defect-induced band, Gong and coworkers have carried out first-principle density functional theory (DFT) calculations (cf. Table 4.2, for details of the calculations see Ref. [135]). The results of the calculation allow us to assign the defect-induced ν_1 to CO adsorbed at 6-fold coordinated Ce^{4+} ions in the direct vicinity of the vacancy (site 1 in Figure 4.1). An assignment to 7-fold coordinated Ce^{3+} ions further away from the vacancy (site 2 in Figure 4.1) can be ruled out.

Table 4.2 Calculated vibration frequencies ν and adsorption energies E_b of CO at various sites on the stoichiometric and reduced ceria (111) surface (one top-surface oxygen vacancy per supercell, experimental frequencies are listed for comparison) [135].

Substrate	Adsorption Site	DFT ν/cm^{-1} (E_b/eV)	Exp. (cm^{-1})
	Free molecule	2122.5	2143.5
Ideal	Ce^{4+}	2145.2 (0.28)	2154
Reduced (V_O surf)	Ce^{4+} at V_O (site 1) Ce^{4+} (3-fold site V_O) Ce^{3+} (site 2) Ce^{4+} (site 3)	2157.2 (0.40) 2169.6 (0.39) 2150.9 (0.27) 2143.1 (0.34)	2163

The calculated vibrational frequency of CO bound to the 7-fold coordinated Ce^{4+} on the stoichiometric surface amounts to 2145.2 cm^{-1}, which differs by ~9 cm^{-1} from the experimentally observed frequency of 2154 cm^{-1}. It can clearly be seen from Table 4.2 that the vibrational frequencies of CO adsorbed on defective surface sites shift to higher values, especially for CO adsorbed in a configuration allowing for direct interaction with the vacancy (site 1 in Figure 4.1 or center of V_O).

The calculated frequencies for adsorbed CO were corrected by multiplying the calculated values by a factor of 2143/2122.5 or 1.0097, corresponding to the ratio of the experimental and calculated values for gas-phase CO.

These calculations beautifully corroborate our above assignment, namely that the blue-shift of 10 cm^{-1} seen in the experiment when going from the stoichiometric to the reduced substrate has to be assigned to CO bound to Ce^{4+}-sites in direct vicinity of the vacancy.

Calculations carried out for different CO-coverages which in previous work [136, 137] has been found to affect both CO binding energies and stretch frequencies, revealed that the local CO concentrations have almost no effect on the CO binding energies. Since in previous assignments of IR-powder data a number of assignments has been reported for CO bound to a 6-fold coordinated Ce^{3+} (present only in a less stable defective surface configuration with the two excess electrons localized at nearest-neighbor Ce cations) [111], Gong et al. also considered this adsorption site. The adsorption energy was found to be 0.32 eV, i.e. lower compared to 6-fold coordinated Ce^{4+} (cf. Figure 4.5). However, this adsorption energy is slightly larger with respect to that on the 7-fold coordinated Ce^{3+} (cf. Figure 4.5b)

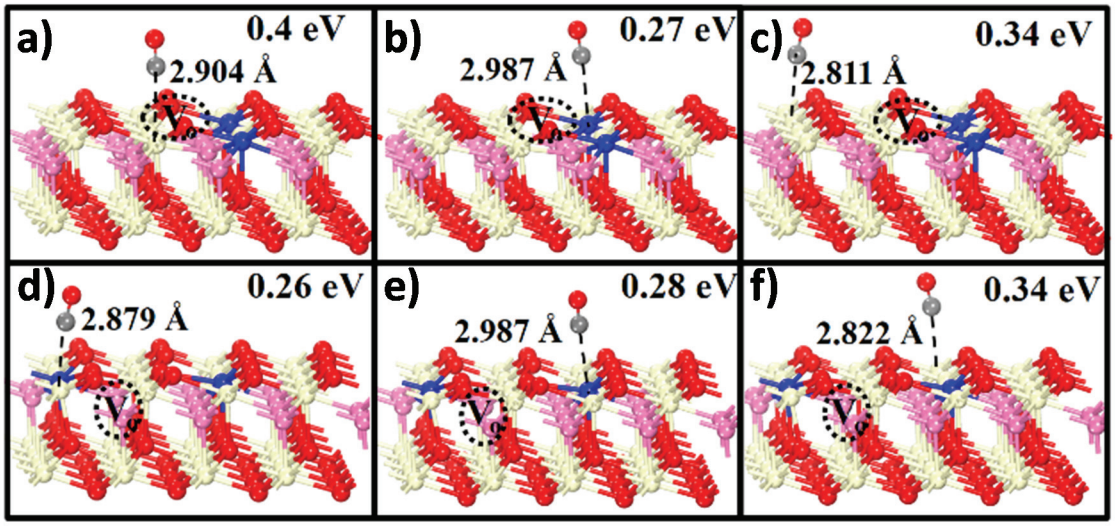

Figure 4.5 Calculated structures (side view) of CO adsorbed at different sites on the reduced CeO_{2-x}(111) with (a–c) top- and (d–f) subsurface O vacancy [135]. The calculated OC-Ce distances and adsorption energies are also presented. C atoms are in grey.

The experimental and theoretical observations provide a solid basis for the identification of stretch frequencies for CO bound to ceria (111) substrates. For CO bound to 7-fold coordinated (i.e. fully coordinated for a surface cation) Ce^{4+}-cations (denoted $Ce^{4+}{}_{7c}$ where c stands for "coordinated") within the stoichiometric surface, the stretch frequency, ν_1, amounts to 2154 cm^{-1}. The calculated adsorption energy of 0.28 eV for this species is in good agreement with the activation energy for desorption of 0.27 eV extracted from the temperature programmed desorption experiment.

Surprisingly, the CO species bound to defective parts of the surface exhibits a blue-shift (in contrast to other oxides). For Ce-ions in direct vicinity of the oxygen-vacancy, the corresponding blue-shift amounts to 10 cm^{-1}. We tentatively ascribe the increased adsorption energy and higher vibrational frequency observed for this species to electrostatic interactions resulting from a coupling of the CO dipole and the dipole of the top-surface-O-Ce double layer when the molecule moves inside the vacancy.

Based on the best agreement in the stretch frequency, we assign the band at 2163 cm^{-1} to CO at Ce^{4+} ions at the V_O site. Note also that the number of available $Ce^{4+}{}_{6c}$-sites is three times larger than that of the 3-fold hollow sites inside the vacancy. In fact, the spectra displayed in Figure 4.4 would be consistent with the presence of a weak feature at higher frequencies, where theory would predict the position of the stretch frequency for CO adsorbed within the

O-vacancies. As the calculated binding energy is very similar to the one calculated for adsorption on Ce^{4+} ions at the vacancy, one would expect that this site would be populated as well. Our results demonstrate that the coordination geometry can play a decisive role for weak chemical interactions on oxide surfaces. While on TiO_2 and many other oxides the frequency of adsorbed CO is mainly given by the charge state of the metal cation, the coordination geometry exhibits a more pronounced influence for CeO_2.

4.2 CO adsorption on ceria (110)

After the successful investigation of CO adsorption on CeO_2(111) surfaces, we also performed IRRAS measurements on CeO_2(110) single crystals. The oxidized CeO_2(110) surface was prepared by annealing at 800 K in 1×10^{-5} mbar O_2 atmosphere for 15 minutes. Figure 4.6 shows the IRRAS data of oxidized CeO_2(110) exposed to different doses of CO. The p-polarized spectra exhibit a sharp peak at 2170 cm^{-1}, which can be assigned in a straightforward fashion to CO molecules bound to Ce^{4+} cations embedded in a perfect single crystalline surface environment. It is astonishing that the frequency of adsorbed CO on oxidized CeO_2(110) surface is substantially different from the counterpart of CeO_2(111), and the difference between them reaches 16 cm^{-1}, which allows for discrimination of facet orientations. Additionally, weak features at 2154 cm^{-1} are observed in both p- and s-polarized spectra, which are caused by CO adsorption at a small amount of (111) step edges in the CeO_2(110) surface (see Figure 4.7).

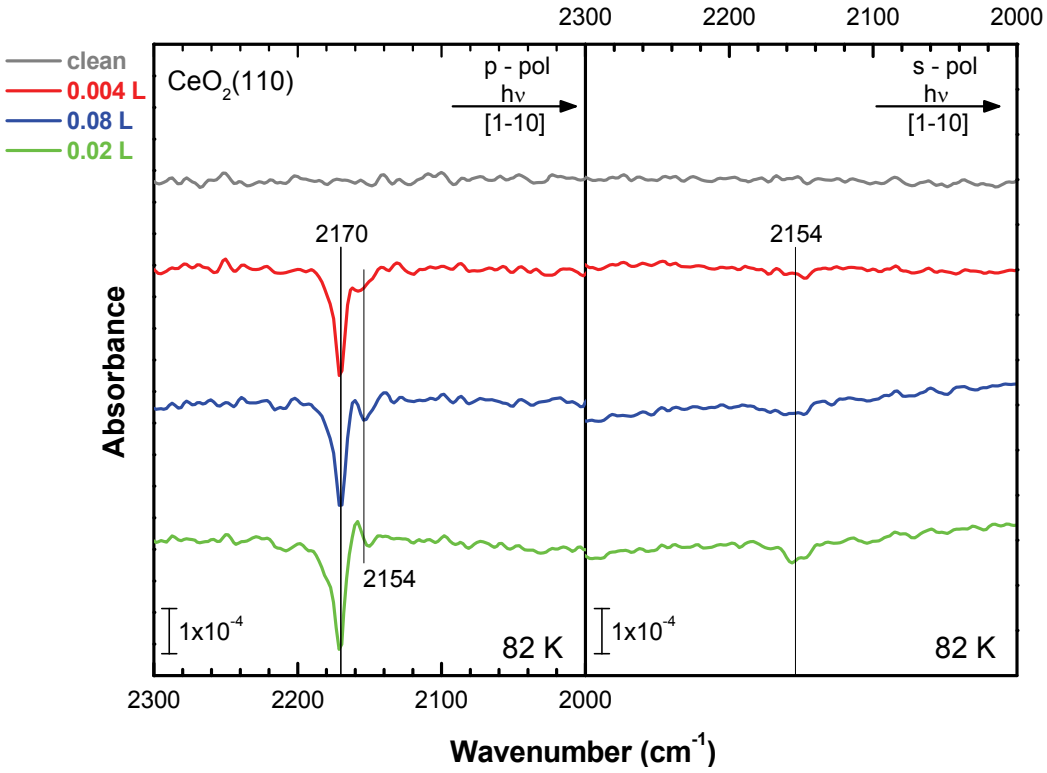

Figure 4.6 Experimental IRRA spectra of different doses of CO at 82 K on oxidized CeO_2(110) at a grazing incidence angle of 80° with (left) p- and (right) s-polarized light incident along [1-10].

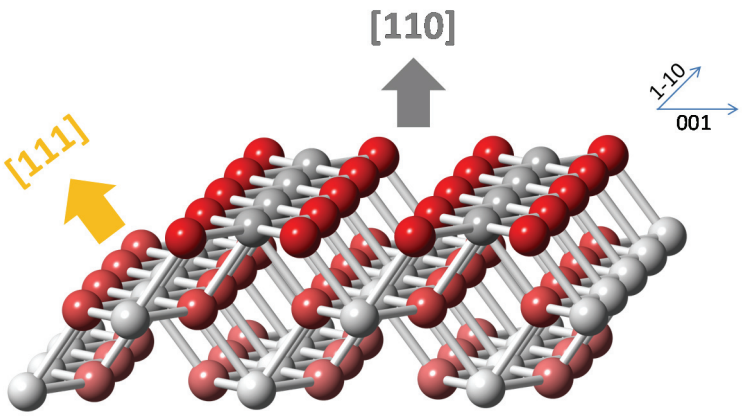

Figure 4.7 Ball-and-stick model of the CeO_2(110) surface. Color: red – top surface oxygen, light red – subsurface oxygen, grey – cerium.

Figure 4.8 shows the temperature-dependent IRRAS data obtained after CO adsorption on the oxidized CeO_2(110) surface at 82 K and subsequently heating to higher temperatures. The IR spectra demonstrate that upon heating the main band at 2170 cm^{-1} decreases in intensity until it vanishes at 100 K, and concurrently the small shoulder at 2182 cm^{-1} is then resolved and disappears completely at the temperature higher than 110 K. The component at high frequency is probably induced by CO adsorption on defective sites which exhibits a higher binding energy.

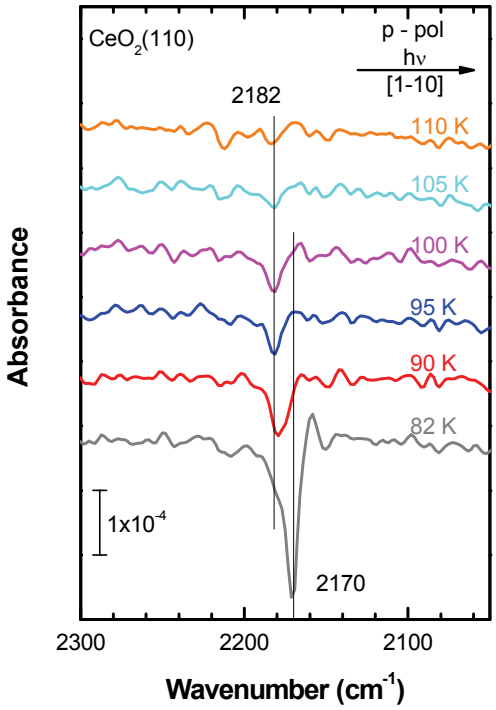

Figure 4.8 Experimental IRRA spectra recorded directly after dosing of 0.1 L CO at oxidized CeO_2(110) surface. The samples were gradually heated and spectra were recorded at the temperatures indicated.

Again we reduced the CeO_2(110) surface via annealing in the UHV without O_2. Based on the XPS results, the concentration of Ce^{3+} on the reduced surface was determined to be approximately 45% (cf. Appendix A1.1). The reduced sample was exposed to 0.005 L CO at 92 K, and the corresponding IRRA spectra are displayed in Figure 4.9, where one broad band at 2177 cm^{-1} is observed in p-polarization which can be fitted with two components at 2170 and 2182 cm^{-1}. In order to reasonably assign the defect-induced CO band, we have to draw support from first-principle density functional theory (DFT) calculations.

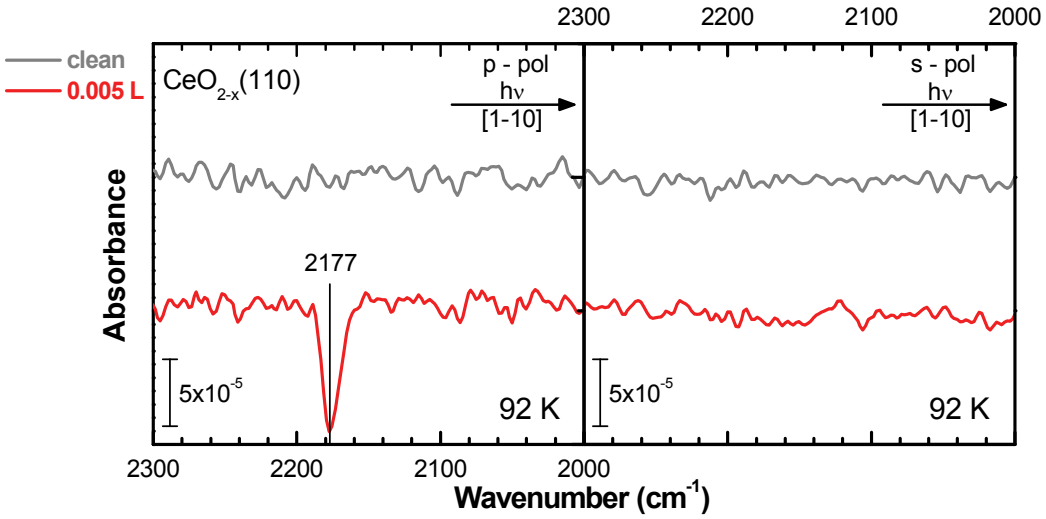

Figure 4.9 Experimental IRRA spectra of 0.005 L CO at 92 K on reduced CeO_{2-x}(110) at a grazing incidence angle of 80° with (left) p- and (right) s-polarized light incident along [1-10].

As shown in Figure 4.10, similar behavior in heating experiments for CO on reduced CeO_{2-x}(110) surface is observed. The component at low frequency side of the band at 2177 cm^{-1} disappears faster and the center of the band shifts to higher frequency (2182 cm^{-1}) with temperature increasing up to 110 K.

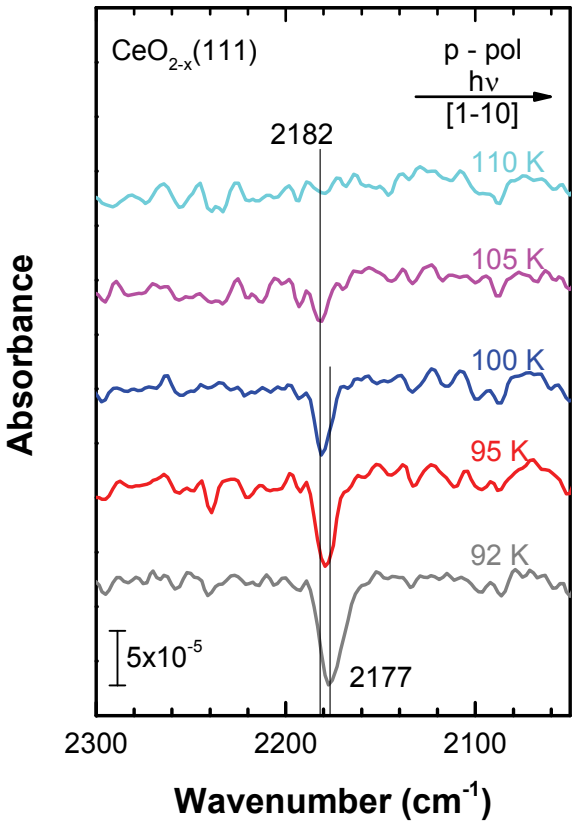

Figure 4.10 Experimental IRRA spectra recorded directly after dosing of 0.005 L CO at reduced CeO_{2-x}(110) surface. The samples were gradually heated and spectra were recorded at the temperatures indicated.

The repeated cycles of sputtering and annealing lead to continuous formation of (111) and (11-1) facets on the CeO_2(110) surface. We have also investigated these faceted surfaces by IRRAS with CO adsorption. Figure 4.11 shows the corresponding IRRA spectra, which monitor the evolution of CO vibrational bands with the coverage increasing. At the lowest CO coverage, the main band is located at 2170 cm^{-1} with a minor shoulder at 2180 cm^{-1}, which originates from CO bound to perfect and defective sites on the (110) terrace, respectively. As the CO coverage increases, the low-lying features (mainly at 2154 cm^{-1}) originating from CO adsorbed on (111) facets emerge and then become more intense with the inhibition of the (110) related CO bands. At the saturation coverage, the CO band at 2154 cm^{-1} is predominant indicating that the low energy facets (111) and (11-1) have been formed dominantly on the surface. In s-polarized spectra, the CO bands can be clearly resolved as two components at 2154 and 2163 cm^{-1}, which are assigned to CO species adsorbed at oxidized and defective sites of (111) facets, respectively. The simultaneous observation of four CO bands (Figure 4.12a) reveals the reconstruction of the reduced CeO_{2-x}(110) surface leading to the coexistence of partially reduced (110) terrace and (111) facets. Moreover, the fact that only

(111) facet-related CO bands are observed in that s-polarized spectra, provides further evidence for the formation of (111) and (11-1) micro-facets, where CO molecules are bound in a tilted geometry with respect to the normal of the substrate.

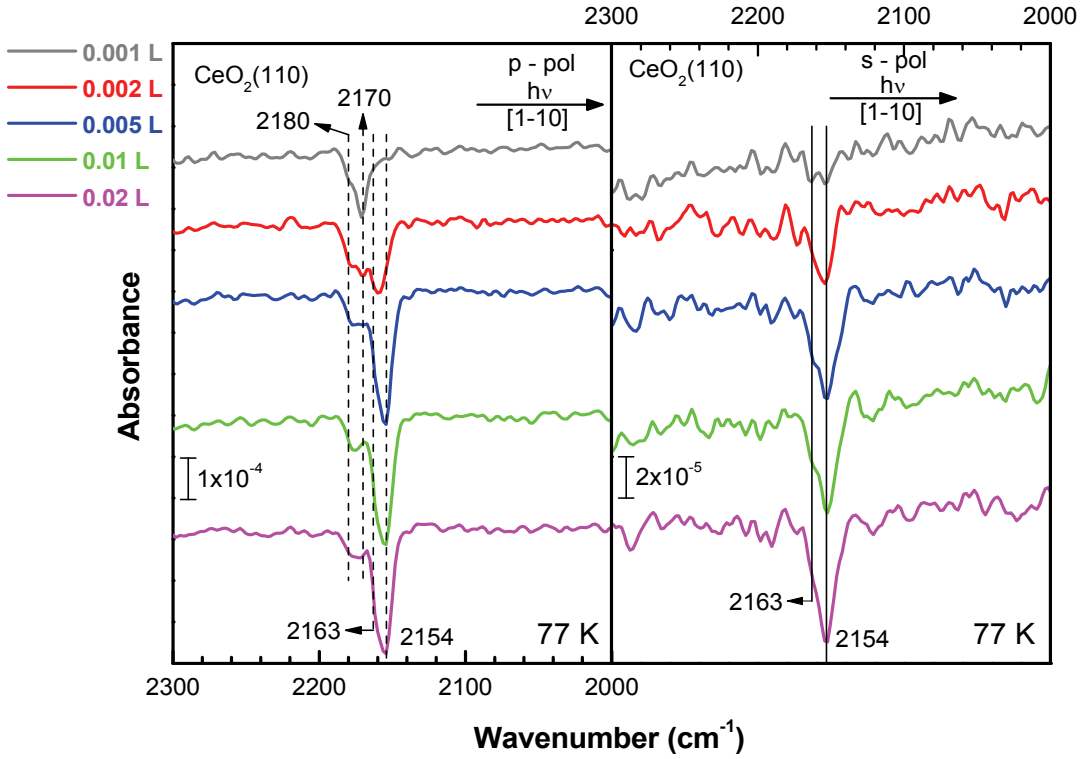

Figure 4.11 Experimental IRRA spectra of different doses of CO at 77 K on faceted CeO_2(110) at a grazing incidence angle of 80° with (left) p- and (right) s-polarized light incident along [1-10].

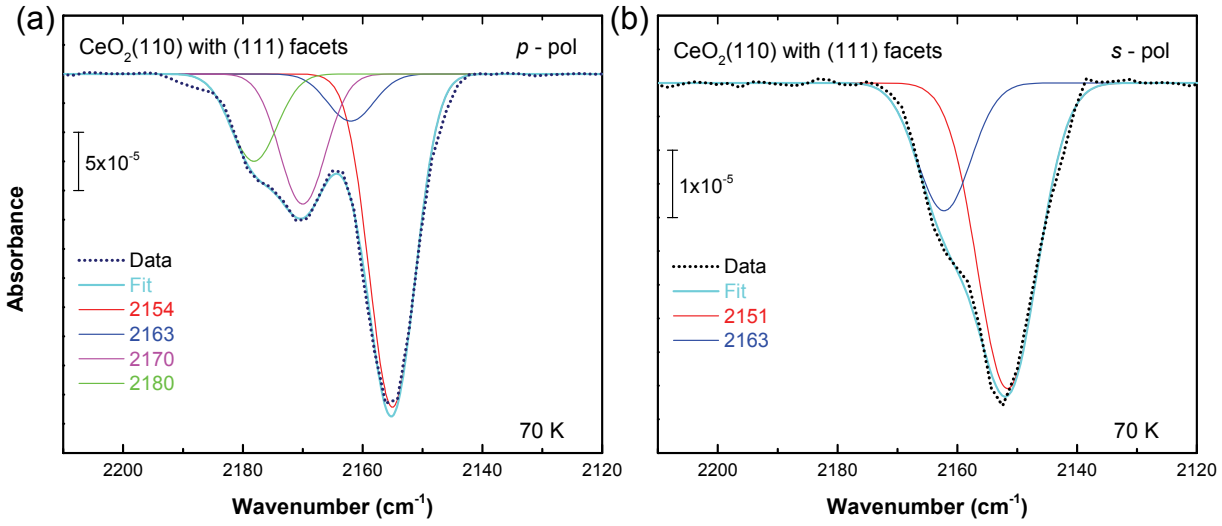

Figure 4.12 Fitting of p- and s-polarized spectra of 0.003 L CO at 70 K on faceted CeO_2(110).

After saturated with CO, the faceted sample substrate was stepwise heated to higher temperatures, and the obtained temperature-dependent IRRAS data are shown in Figure 4.13. By increasing temperature the (111) facet-related CO bands at 2154 and 2163 cm^{-1} decrease first and disappear completely at 85 and 90 K, respectively. They are less stable than CO species on flat (111) surfaces. We speculate that this unusual phenomenon might be due to the thermal diffusion of CO molecules from (111) and (11-1) facets to (110) terraces, since CO molecules are more strongly bound to the (110) surface with slightly higher binding energies. This conclusion is supported by the fact that the attenuation of the two low-lying CO bands is accompanied by the growth of the 2183 cm^{-1} band originating from CO adsorbed at the reduced sites of (110) terraces. The latter band is stable up to 102.5 K and disappears as the temperature increases to 110 K.

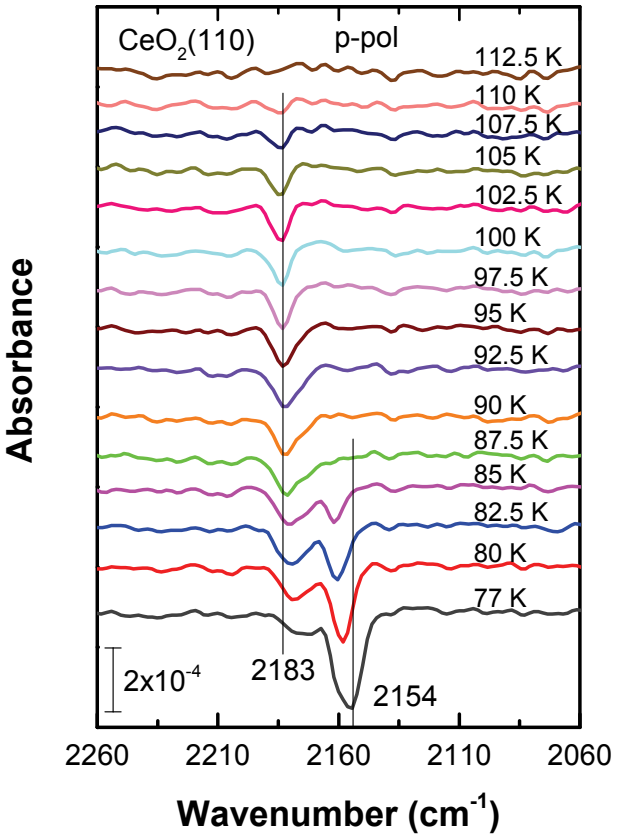

Figure 4.13 Experimental IRRA spectra recorded directly after dosing of 0.02 L CO at 77 K on faceted CeO_2(110) surface. The samples were gradually heated and spectra were recorded at the temperatures indicated.

4.3 CO adsorption on ceria (100)

The bulk-terminated (100) surface of CeO_2 is a type 3 unstable polar surface according to Tasker's polar surface notation (see Figure 1.3) [51], and its surface structure is still under debate. The LEED images also illustrate complex reconstructions occurring on this surface (cf. Appendix A1.2). CO adsorption measurements were first carried out on heavily reduced CeO_{2-x}(100) surface (~40% Ce^{3+}, see Appendix A1.3) and the corresponding IRRAS data are shown in Figure 4.14. At low coverages an IR signal at 2170 cm^{-1} is observed. With increasing doses, the CO band shifts gradually to lower frequencies, accompanied by a substantial increase in intensity. When the surface is saturated with CO at 70 K, the ν(C-O) vibration is centered at 2164 cm^{-1} with a shoulder at lower frequency side. By drawing an analogy with CeO_2(111) and (110), where the IR bands of CO adsorbed on defective sites are always located at higher frequencies than those on perfect sites, here the dominant band 2164 cm^{-1} is probably induced by surface defects, while the small shoulder might originate from CO adsorption on perfect sites of the surface as minority species. The 2164 cm^{-1} band is also observed for s-polarized light, indicating that CO is bound to the reduced sites on CeO_{2-x}(100) in a tilted configuration.

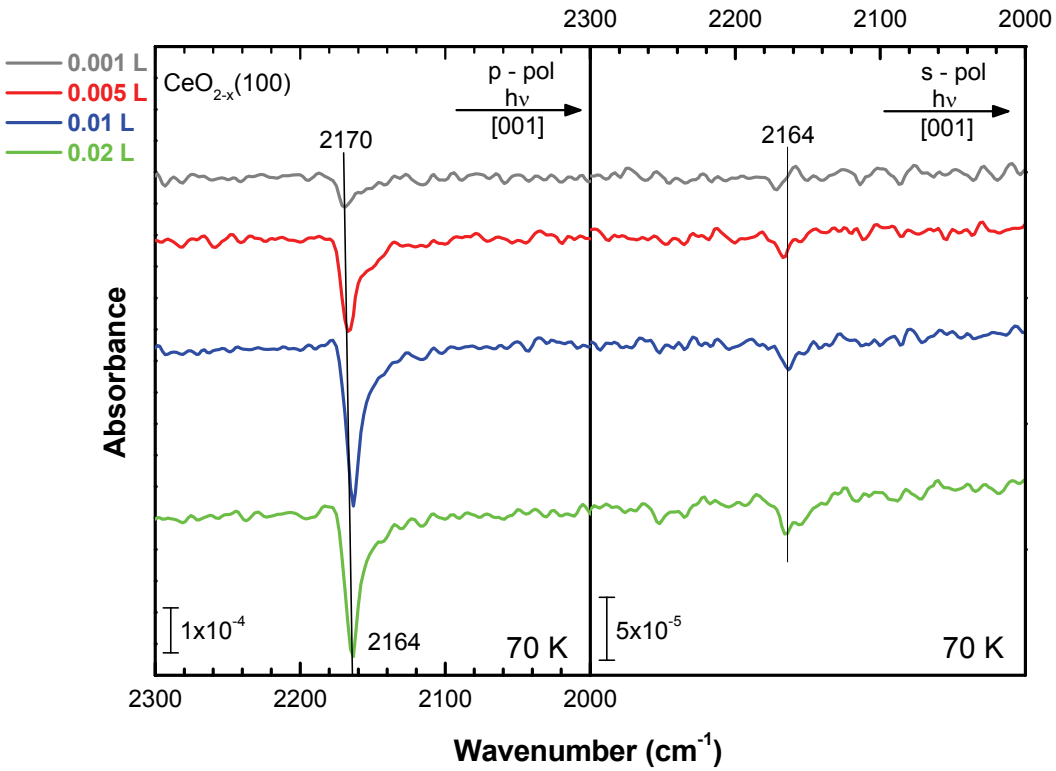

Figure 4.14 Experimental IRRA spectra of different doses of CO at 70 K on reduced CeO_{2-x}(100) at a grazing incidence angle of 80° with (left) p- and (right) s-polarized light incident along [001].

We have also performed heating experiments (cf. Figure 4.15) to investigate the thermal stability of CO species and the influence of CO coverage on its vibrational frequency. Upon heating to 90 K, the CO vibrational frequency shifts upwards by 9 cm^{-1} to 2173 cm^{-1}, and the large decrease of the band intensity reveals the desorption of CO molecules. Interestingly, the thermal stability of CO on reduced CeO_{2-x}(100) surface is markedly lower than that of CO on the other reduced CeO_{2-x} surfaces, which is probably related to the (100) surface reconstructions lowering the surface energy.

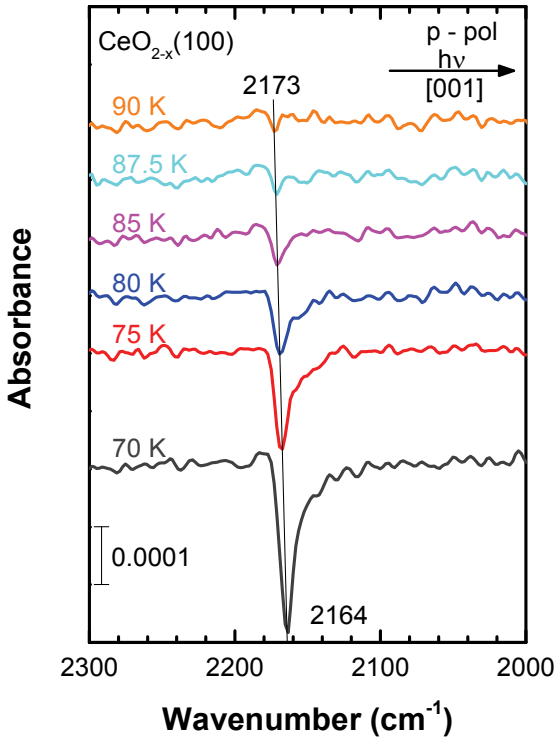

Figure 4.15 Experimental IRRA spectra recorded directly after dosing of 0.02 L CO at heavily reduced CeO_{2-x}(100) surface. The samples were gradually heated and spectra were recorded at the temperatures indicated.

By exposing the reduced CeO_{2-x}(100) surface to molecular oxygen (O_2) at 110 K and then heating up the substrate to room temperature, we oxidized the sample surface to some extent (cf. Appendix A1.4). The IRRA spectra of CO adsorption on partially oxidized CeO_2(100) surface are shown in Figure 4.16. In the p-polarized spectra, apart from the main peak at 2164 cm^{-1}, the shoulder at 2150 cm^{-1} grows significantly and another new band emerges at 2182 cm^{-1}, which suggests that at least three different adsorption sites exist on the partially oxidized CeO_2(100) surface.

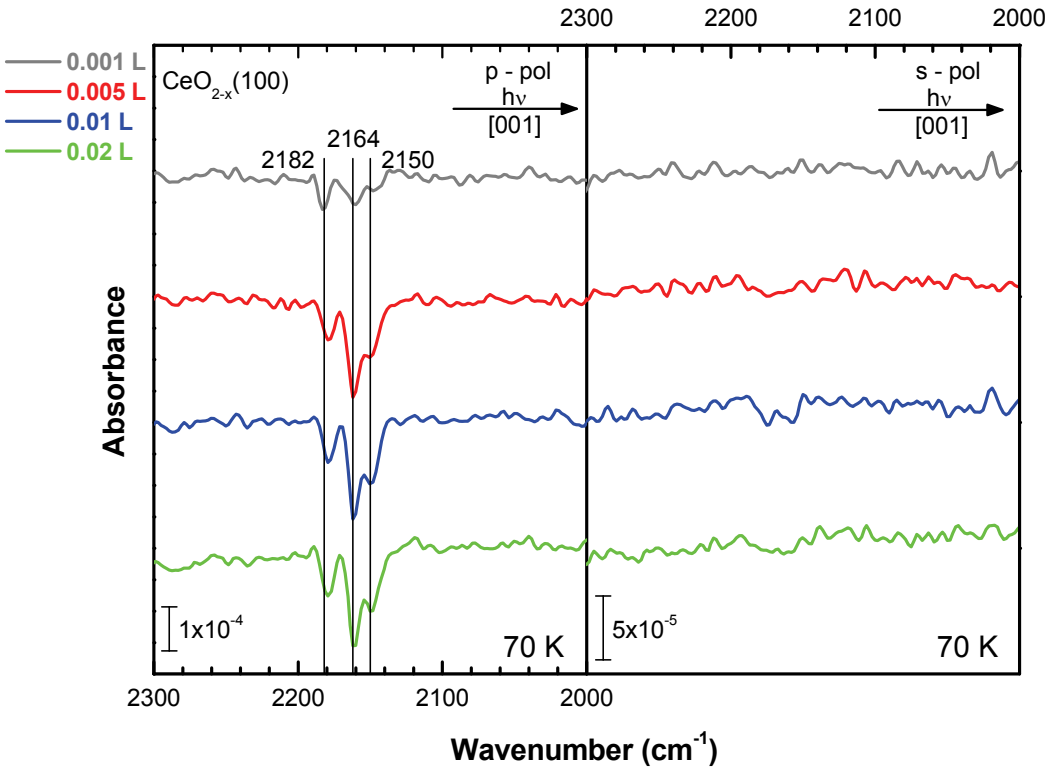

Figure 4.16 Experimental IRRA spectra of different doses of CO at 70 K on partially oxidized CeO_2(100) at a grazing incidence angle of 80° with (left) p- and (right) s-polarized light incident along [001].

After CO adsorption on partially oxidized CeO_2(100) at 70 K, the sample was subsequently heated to higher temperatures. The corresponding spectra are displayed in Figure 4.17. The two CO species with lower vibrational frequencies (2162 and 2148 cm^{-1}) decrease nearly simultaneously in intensity during temperature elevating process but both remain unchanged in frequency, while the CO vibrational band at 2179 cm^{-1} shifts to higher frequencies with decrease of the intensity. Moreover, the CO species with highest frequency surviving till 100 K is apparently more stable than the other two CO species on the surface.

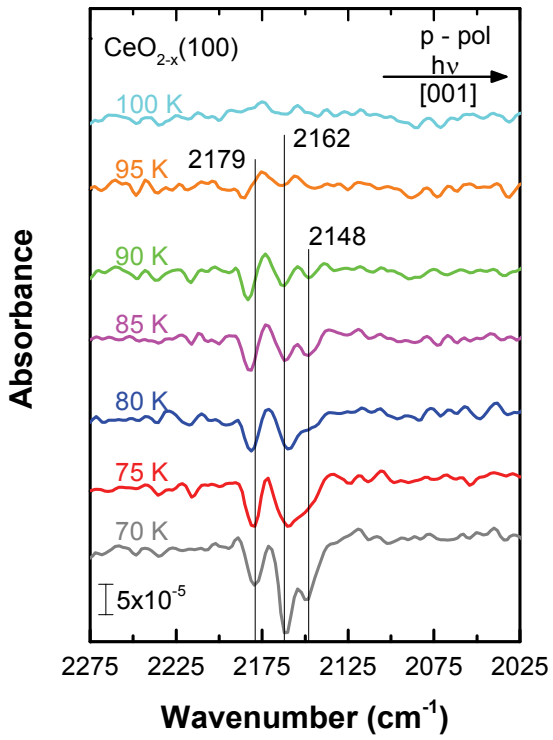

Figure 4.17 Experimental IRRA spectra recorded directly after dosing of 0.02 L CO at partially oxidized CeO_2(100) surface. The samples were gradually heated and spectra were recorded at the temperatures indicated.

4.4 CO adsorption on ceria films

4.4.1 CO adsorption on thin ceria film

Since the complex structure of technical catalysts and their difficulties in characterization impede the attempt to describe the detailed mechanisms of reactions taking place at the catalyst surfaces, one has to resort to a systematic model approach. Therefore the so-called surface science approach out of the full modern arsenal of surface sensitive techniques was developed, which has achieved spectacular successes during the last 60 years via transfer of the information from well-defined single crystal surfaces to identify many of the molecular ingredients of important catalytic reactions [7, 138]. Nevertheless, only since around 1990, intensive studies have been carried out on planar model surfaces of metal oxides due to their low electrical and thermal conductivity resulting in charging and cooling problems [15]. In order to tackle these problems, growth of oxide thin films with well-ordered surfaces on metallic substrates then has been introduced into surface science studies [16, 17]. However, there is a long controversy over whether physical and electronic structures of oxide thin films can mimic those of the corresponding bulk phases [139]. It is claimed that thin films exceeding a critical thickness (e.g. 10 ML) can closely resemble the corresponding bulk material, whereas the oxide films with smaller thickness exhibit new properties [140, 141], because the influence from metal substrate and metal oxide interface on the intrinsic properties of the oxide is probably inevitable [142, 143] and some amount of the buried substrate atoms might diffuse onto the film surface [144].

Here we use CeO_2 as a case study to illustrate the difference between bulk single crystals and corresponding thin films. We present results of the comparison of the IRRAS data measured for CO adsorbed on single crystal CeO_2(111) with those obtained in a case of ceria thin film. The obtained results clearly demonstrate that thin oxide films, especially exhibiting the high density of defects, are not perfect alternatives to the single crystals.

Figure 4.18 shows experimental IRRA spectra recorded on a reduced and stoichiometric CeO_2(111) single crystals under UHV conditions after the exposure to 2.6×10^{-7} Pa CO for 50 seconds [135] and the data obtained for the (oxidized) ceria film at 0.267 Pa (2 mTorr) CO background pressure [127]. Together with the experimental data acquired for the CeO_2(111) single crystal and ceria film, transmission spectrum recorded for ceria powder at 77 K at a

background pressure of 1×10^{-2} Pa CO is also displayed [121]. The CO stretch frequency on the stoichiometric single crystal amounts to 2154 cm^{-1}, whereas the small contribution corresponding to CO adsorbed on reduced parts of the crystal is blue-shifted by approximately 10 cm^{-1} to 2163 cm^{-1}. For CO adsorbed on the reduced ceria crystal, both bands at 2154 cm^{-1} and 2163 cm^{-1} corresponding to the adsorption on the pristine and reduced parts of the surface respectively, have comparable intensities resulting in significant peak broadening. When adsorbing CO on ceria powder at 77 K, two bands at 2168 cm^{-1} and 2157 cm^{-1} are observed. These two bands, albeit slightly blue shifted due to coverage effect, are in good agreement with results for CO on CeO_2(111) single crystal and could be assigned to CO on defective and perfect sites, respectively. However, the spectrum of the oxidized film in 0.267 Pa (2 mTorr) CO displays appreciable intensity only at 2162 cm^{-1}, i.e. only the signature of CO adsorbed on reduced parts of ceria. The absence of the signal arising from CO adsorbed on "regular" sites (away from oxygen vacancies) in a case of the ceria thin film could be explained by i) a high density of the surface defects or ii) a desorption of CO molecules from "regular" sites of CeO_2 surface at 90K.

In order to clarify this situation we simulated dependences of the relative CO coverage on the substrate temperature for different CO background pressures. According to refs. [145-149] the rates of adsorption and desorption are given by

$$r_{\mathrm{a}} = \frac{\sigma_{\mathrm{A}} d\theta_{\mathrm{r}}}{d_{\mathrm{t}}} = \frac{p}{\sqrt{2\pi m k T}} s_0 \exp\left(-\frac{E_{\mathrm{a}}}{kT}\right) f(\theta_{\mathrm{r}}) \tag{4.4}$$

$$r_{\mathrm{d}} = \frac{\sigma_{\mathrm{A}} d\theta_{\mathrm{r}}}{d_{\mathrm{t}}} = -\nu_{\mathrm{n}} \sigma_{\mathrm{A}}^{n} \exp\left(-\frac{E_{\mathrm{d}}}{kT}\right) \theta_{\mathrm{r}}^{n} \tag{4.5}$$

where E_a and E_d are the activation energies for adsorption and desorption respectively, p is the (partial) gas pressure, m the mass of the adsorbed species, k the Boltzmann constant, T the temperature, s_0 the initial sticking probability, σ_A the density of adsorption sites, $\theta_r=\theta/\theta_{sat}$ the relative coverage ($0 < \theta_r < 1$), and ν_n the frequency factor for n-order reaction.

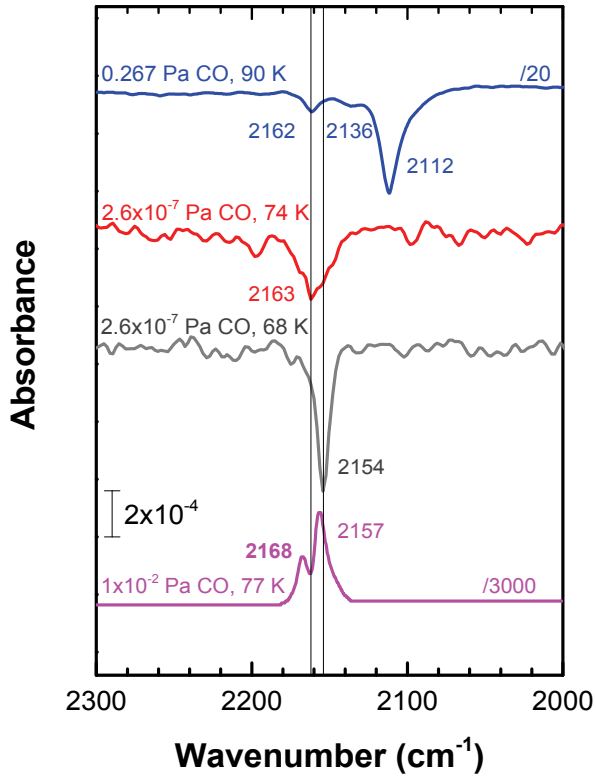

Figure 4.18 IRRA spectrum of a oxidized thin ceria film at 90 K (blue) at a background pressure of 0.267 Pa (2 mTorr) CO (blue) [127], spectra recorded on a reduced CeO_{2-x}(111) single crystal containing 10% oxygen vacancies under UHV at 74 K (red) and a stoichiometric CeO_2(111) single crystal in UHV at 68 K (grey) after exposure to 2.6×10^{-7} Pa CO for 50 seconds [135], and IR transmission spectrum of ceria powder at 77 K at a background pressure of 1×10^{-2} Pa CO (magenta) [121].

In adsorption-desorption equilibrium the rates of adsorption and desorption are equal, i.e. $r_a + r_d = 0$. For first order desorption assuming "hit and stick" adsorption (Langmuir), the sticking probability, s, for non-dissociative adsorption is proportional to the number of unoccupied sites: $f(\theta_r) = 1 - \theta_r$. Equating (4.4) and (4.5) and resolving for the relative coverage θ_r yield:

$$\theta_r(T,p) = \frac{b_1(T)p}{1+b_1(T)p} \quad , \tag{4.6}$$

b_1 is defined as the following function:

$$b_1 = \frac{s_0 \exp(q_{st}/kT)}{\nu_1 \sigma_A \sqrt{2\pi mkT}} \quad , \tag{4.7}$$

where q_{st} is the isosteric heat of adsorption, ν_1 the frequency factor for first order Langmuir adsorption.

In order to estimate the relative coverage of CO on pristine parts of a CeO_2(111) surface in the

temperature range of 60 K to 100 K, the following values are used:
$s_0 \approx 1$, $\nu_1 = 10^{13}$ s^{-1}, $q_{st} = 25.9$ kJ/mol (~0.27 eV, the binding energy of CO on pristine CeO_2(111)) [135], $m = 4.649 \times 10^{-26}$ kg, $k = 1.3806 \times 10^{-23}$ J/K, $\sigma_A = 7.89 \times 10^{18}$ m^{-2} (the density of surface Ce sites).

For the relative coverage as a function of temperature, we obtain for (a) p(CO)=2.6×10^{-7} Pa, i.e. UHV conditions,

$$\theta_r(T) = \frac{2.6 \times 10^{-7} \times \exp\frac{3115}{T}}{1.58 \cdot 10^8 \times \sqrt{T} + 2.6 \times 10^{-7} \times \exp\frac{3115}{T}}$$

and for (b) p(CO)=0.267 Pa (2 mTorr), i.e. relatively high pressure conditions compared to UHV,

$$\theta_r(T) = \frac{0.267 \times \exp\frac{3115}{T}}{1.58 \cdot 10^8 \times \sqrt{T} + 0.267 \times \exp\frac{3115}{T}}$$

Figure 4.19 displays these simulated isobars (solid lines), which for the case of the low CO background pressure (labeled UHV) match quite well to the experimental data (scattered points) deduced from IRRAS experiments [135], especially considering that the model relies on the generic frequency factor of 10^{13} s^{-1} for lack of experimental data. Hence, the employed rather simple model seems to reflect the experiment to a sufficiently accurate level. The curve at the elevated pressure of 0.267 Pa (2 mTorr) clearly demonstrates that the temperature stability of adsorbed CO is greatly increased and desorption is not expected below 120 K. Consequently, one would expect to observe in IR spectra the corresponding CO stretch frequency of CO adsorbed at stoichiometric parts of the surface in a background pressure of 0.267 Pa (2 mTorr) even at temperatures exceeding 90 K, where it would be desorbed under UHV conditions.

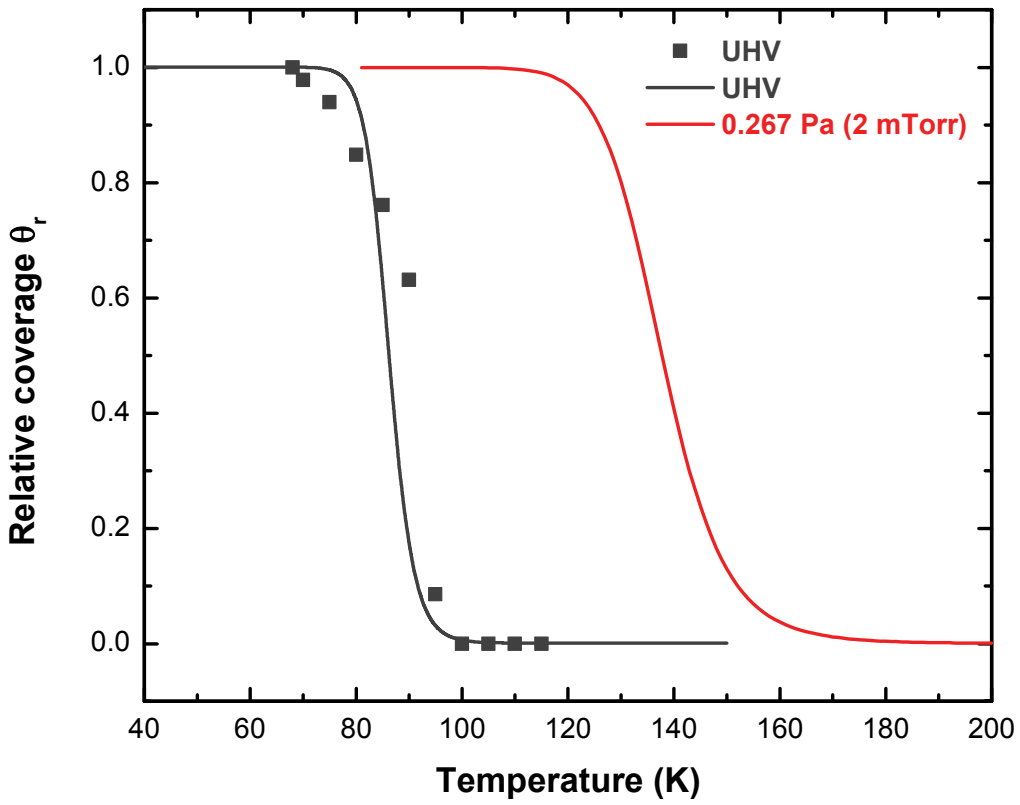

Figure 4.19 Simulated isobars (solid lines) and experimental data (scattered points).

As demonstrated by the simulated isobars in Figure 4.19, the absence of a signal arising from CO adsorbed on "regular" sites (away from oxygen vacancies) cannot be explained by the instability of this species – only under UHV conditions would these species desorb at around this temperature. It must be due to the lack of regular adsorption sites. To conclude, these data nicely demonstrate that for CeO_2 the differences between epitaxially grown thin films and single crystals remain substantial in that the films exhibit a much higher defect density even than deliberately reduced single crystal surfaces.

4.4.2 CO adsorption on thick ceria film

Actually, even for thick films, the experimental observations of CO adsorption are not identical with those of ceria single crystals. Figure 4.20 shows the IRRA spectra of CO adsorption on the oxidized CeO_2(111) film (thickness ~250 nm) grown on a Si(111) substrate [150]. Before IRRAS measurements, the thick ceria film sample was sputtered and annealed repeatedly to decrease the usually rather high density of defects and imperfections as holes or limited continuity.

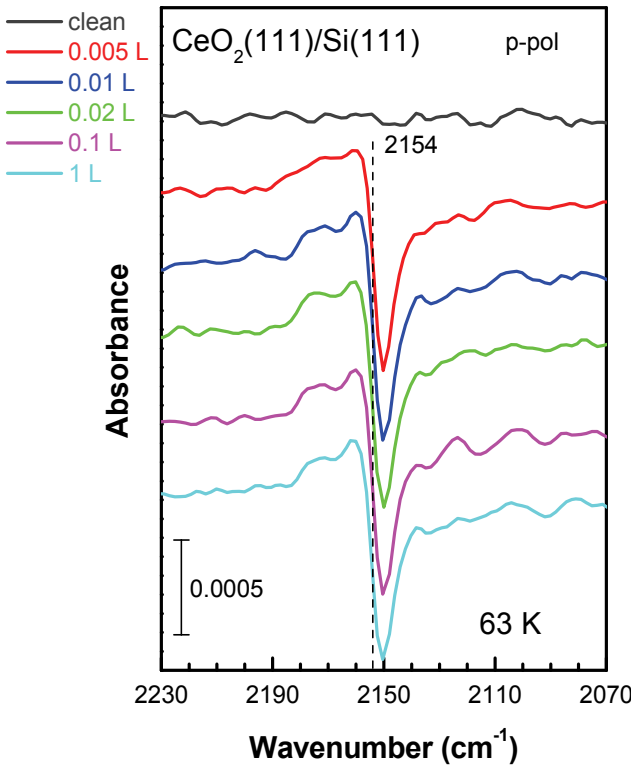

Figure 4.20 Experimental IRRA spectra of different doses of CO at 63 K on oxidized CeO_2(111) thick film at a grazing incidence angle of 80° with p-polarized light.

The biggest difference with single crystal CeO_2(111) is that CO peaks exhibit asymmetric Fano lineshapes due to the different dielectric properties of ceria films. The actual vibrational frequency of CO is close to the point of the maximum slope [151], 2154 cm^{-1}, which is in perfect agreement with the vibrational frequency of CO adsorption on the oxidized single crystal CeO_2(111) surface (cf. Figure 4.2). Additionally, the band intensity for a saturated CO adlayer on ceria thick film is almost twice as high as that of ceria single crystal.

Overall, using CO as the IR-probe molecule, our UHV-IRRAS can distinguish ceria surface orientations and probe surface oxygen vacancies. Based on the obtained vibrational frequencies of CO adsorption on all three low index orientated surfaces of ceria single crystals, the controversial assignments of CO IR-bands derived from previous ceria powder data can be clarified. Both thin and thick ceria films do not exhibit identical IRRA spectra with those of ceria single crystals upon CO adsorption due to either high density defects or different dielectric properties, which indicates that ceria films are not perfect alternatives to the single crystals.

5 Carbon monoxide (CO) adsorption on ceria nanocrystals

In recent years, many studies have reported improved activity of CeO_2 catalysts through synthesis of CeO_2 nanostructures with controlled morphology [152, 153]. The controlled morphology usually can expose well-defined low index (110) and (100) crystallographic planes, which are less stable and thus more reactive than the (111) surface. Ceria nanocrystals with various shapes including octahedra, cubes and rods were first synthesized by using hydrothermal method [154, 155]. Specifically, ceria nanoparticles generally have octahedral shapes mainly exposing stable (111) facets [156]. Ceria cubes preferentially expose active (100) planes [157]. The surface structure of ceria nanorods is more complex and still under debate. It has been proposed that ceria rods expose (100) and (110) surfaces and grow along the [110] direction [154, 155, 158]. However, more recently, it was suggested that ceria rods can also expose (111) surfaces as well as small portion of (100) facets [159]. The discrepancy in surface structure of ceria rods is probably induced by different synthesis and post-treatment conditions and could cause confusion when assigning structure dependent properties.

Microscopic studies have shown the presence of (111) nanofacets on single crystal ceria (110) [72], on ceria (110) thin films grown on Si(100) [160], and on (110) planes of ceria nanoparticles [82, 161]. It is known that the surface energy of CeO_2(110) amounts to 1.41 eV, which is higher than that of CeO_2(111) (1.01 eV) [56]. Therefore, it is energetically favorable for the (110) surface to form a large amount of (111) with lower surface energy.

As presented in chapter 4, CO is capable of probing surface oxygen vacancies and distinguishing facet orientations. In this chapter, we will demonstrate that, on the basis of IRRAS results for various CeO_2 single crystal surfaces, CO can be used as probe molecule to resolve the uncertainty about surface structures of ceria nanocrystals (an intermediate system between single crystals and commercial powders), especially on ceria rods.

The ceria nanoparticle samples (rods, cubes, and conventional powders) were provided by Prof. Alessandro Trovarelli's group at Università di Udine in Italy and were characterized with BET, XRD and HRTEM. For the XPS and IR measurements, around 200 mg ceria nanoparticles were pressed into a stainless steel mesh (13 mm in diameter) with a hydraulic press under the pressure of 5 bar, and then mounted on a sample holder, which was specially designed for the transmission FTIR measurements. Each sample was annealed at 773 K

(nanorods at 723 K) in the UHV chamber to remove the surface impurities (e.g. water and carbon contaminants) and then checked with XPS to ensure the surface cleanness and to determine the oxidation state of cerium.

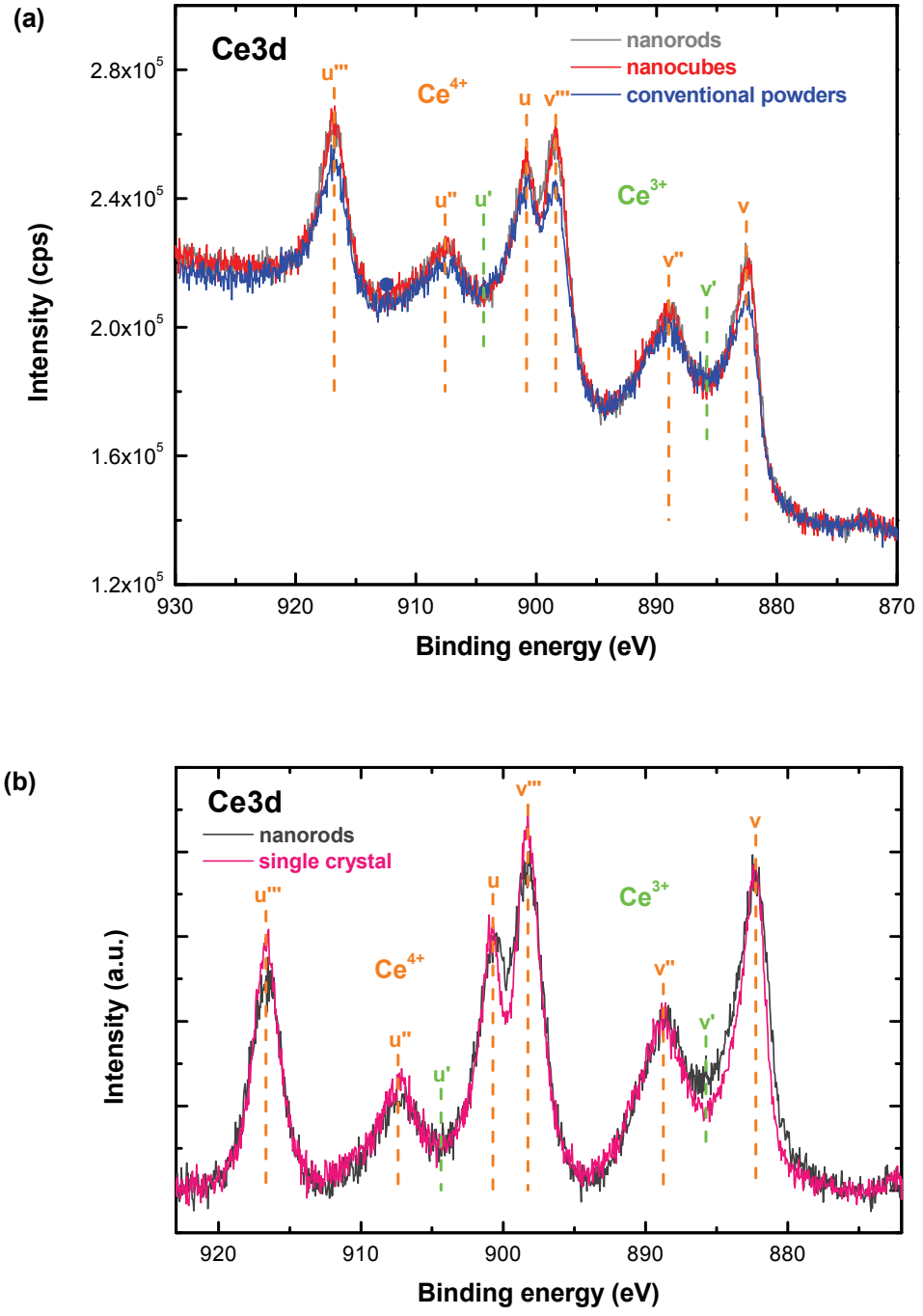

Figure 5.1 (a) Ce3d XP spectra of ceria nanocubes and conventional ceria nanoparticles annealed at 773 K, ceria nanorods at 723 K, for one hour under the UHV condition, (b) comparison of normalized Ce3d XP spectra of ceria nanorods and a fully oxidized ceria single crystal.

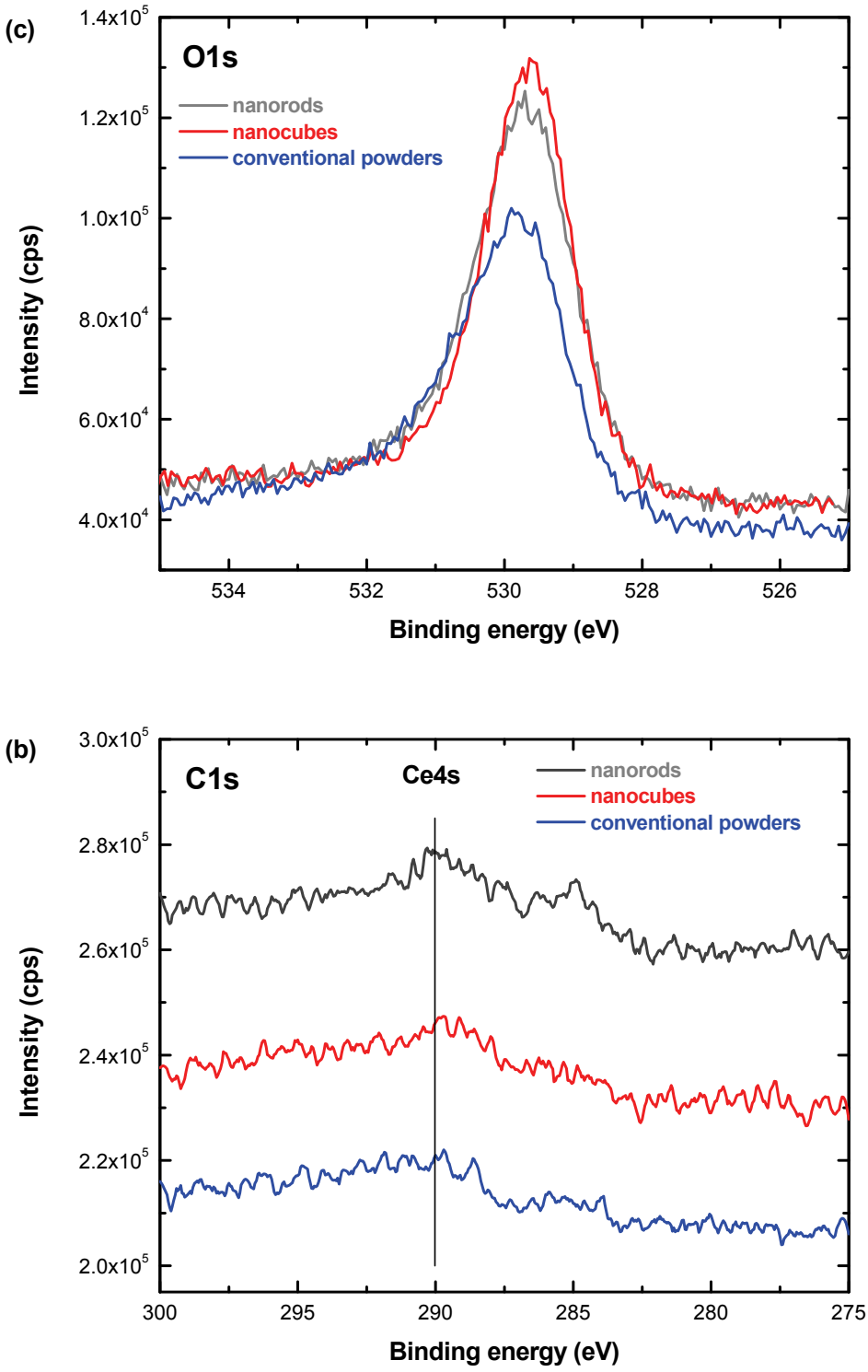

Figure 5.2 O1s (a) and C1s (b) XP spectra of ceria nanocubes and conventional ceria nanoparticles annealed at 773 K, ceria nanorods at 723 K, for one hour under the UHV condition.

Figure 5.1a shows the Ce3d core-level XP spectra of ceria nanoparticles after pretreatments as described above. The Ce3d spectra show that both nanorods and nanocubes are dominated by the v‴, v″, v peaks ($Ce3d_{5/2}$) as well as the u‴, u″, u peaks ($Ce3d_{3/2}$), which are

characteristics for the Ce^{4+} state, indicating a very slight reduction after UHV-annealing, while conventional ceria nanoparticles contain higher amount of Ce^{3+} as confirmed by the typical v_0/u_0 and v´/u´ doublets. This is further supported by the comparison of Ce3d spectra of nanorods with that of a fully oxidized CeO_2 single crystal (see Figure 5.1b).

Figure 5.2 shows the O1s and C1s core-level XP spectra of ceria nanoparticles. Apart from the intense lattice oxygen peak at 529.5 eV, the O1s spectra show weak shoulder at 532 eV, which can be mainly assigned to the residual OH groups on sample surfaces [162]. In the C1s region, we observed a broad peak of Ce4s centered at 290 eV, whereas the typical carbon peak at 285 eV is too weak to be detected, although a higher pass energy (200 eV) was used for this region (the Ce3d and O1s spectra were collected at 100 eV pass energy). This indicates that carbon containing contaminants on sample surfaces were almost completely removed via UHV-annealing at 773/723 K.

After XPS characterization, the samples were transferred into IR chamber and checked with UHV-FTIR in transmission mode. Figure 5.3 shows UHV-FTIR single channels of ceria nanoparticles. All three spectra display rather similar absorption bands despite different intensities. The set of bands between 3800 and 3500 cm^{-1} are stretching vibrations of surface hydroxyl groups coordinated with different number of cerium cations [163]. The intense bands at ~1460 and 1395 cm^{-1} originate from the bulk carbonaceous impurities [124]. The band at 1060 cm^{-1} can be ascribed to the first overtone of fundamental ν(Ce-O) mode at 530 cm^{-1} [36]. It is expected that for the reduced ceria a band at 2125 cm^{-1} appears and is attributed to the forbidden $^2F_{5/2} \rightarrow {}^2F_{7/2}$ electronic transition of Ce^{3+} [36]. However, it is not detected in Figure 5.3, which is consistent with the XPS results that show predominately oxidized Ce^{4+} cations for all ceria nanoparticle samples.

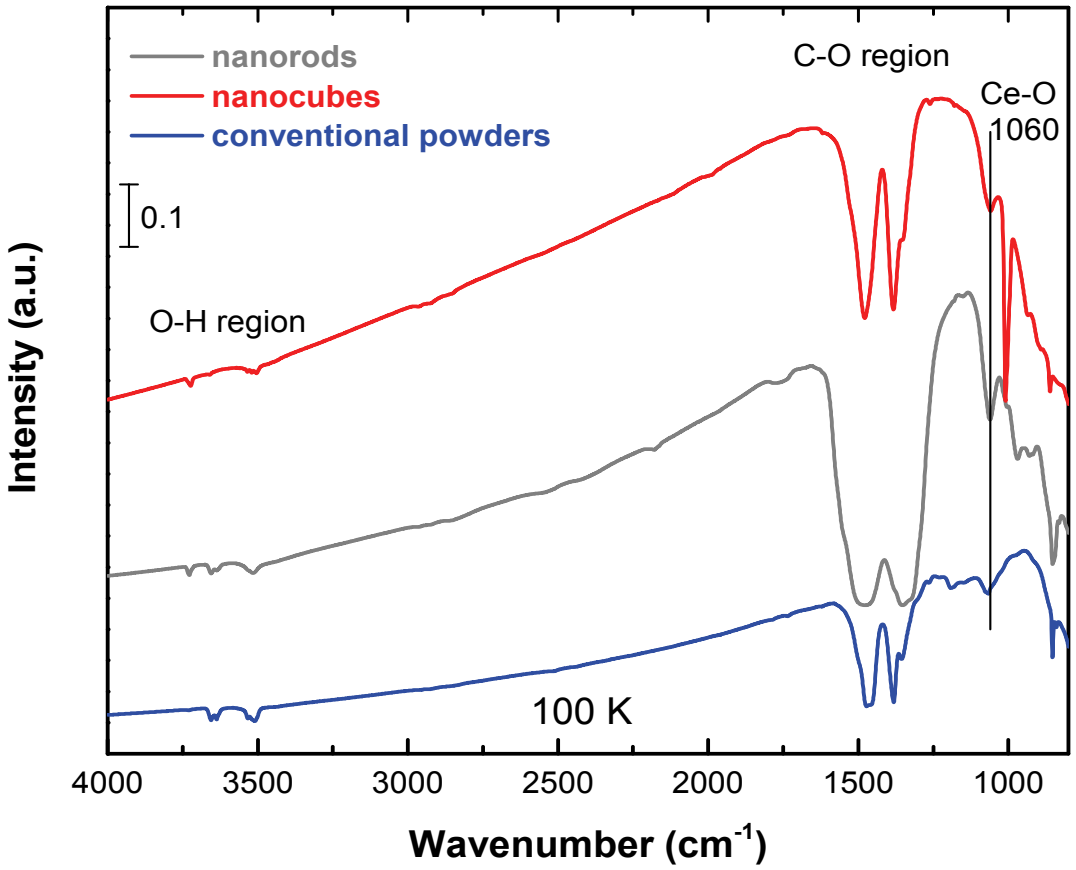

Figure 5.3 UHV-FTIR single channels of ceria nanocubes and conventional ceria nanoparticles after pretreatments as described above.

5.1 CO adsorption on ceria nanorods

UHV-FTIR measurements of CO adsorption were performed at 105 K on the ceria nanorods, which were pre-annealed at 723 K. The corresponding results are shown in Figure 5.4. After exposure to CO, a broad feature emerged in the range between 2140 and 2190 cm^{-1}. A closer analysis allows us to resolve two main components centered at 2176 and 2157 cm^{-1}.The former band shows a slight red-shift to 2174 cm^{-1} upon increasing CO doses. With reference to our results of CO adsorption on ceria single crystals, these two components can be presumably assigned to CO on Ce^{4+} sites of (110) and (111) facets, respectively [135].

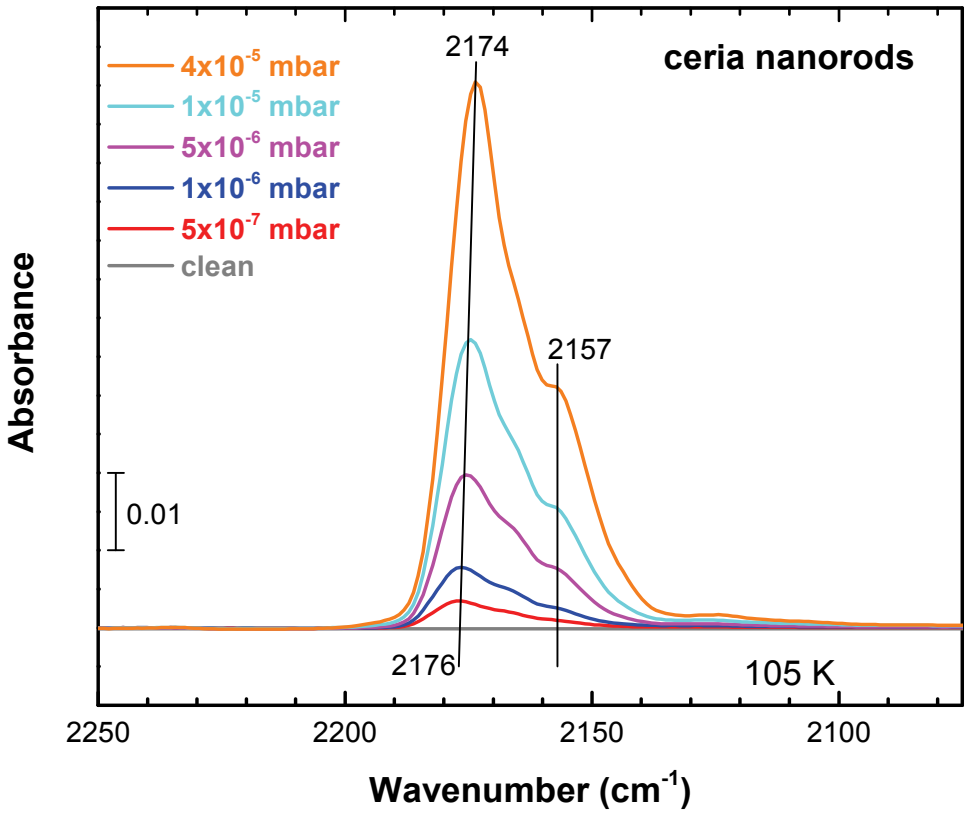

Figure 5.4 UHV-FTIR spectra recorded after exposing the ceria nanorods to different doses of CO at 105 K. The sample was annealed at 723 K for one hour under the UHV condition to remove surface impurities.

After in-situ IR measurements of CO adsorption on ceria nanorods at 105 K, the IR chamber was evacuated down to 10^{-10} mbar range, and then the sample was stepwise heated up to 170 K. In parallel, the IR spectra were recorded at different elevated temperatures (see Figure 5.5). The 2157 cm^{-1} band disappeared first upon heating to 130 K, while the band at 2176 cm^{-1} vanished only after annealing to 160 K indicating a higher binding energy of the corresponding CO species.

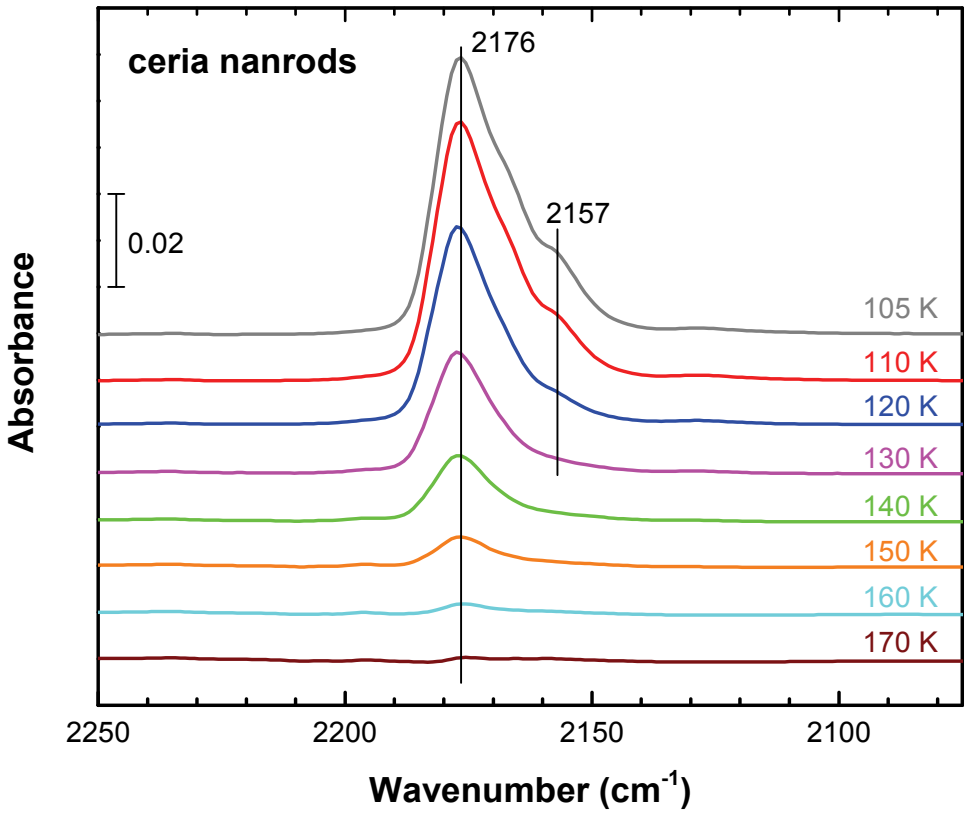

Figure 5.5 UHV-FTIR spectra recorded after exposing the ceria nanorods to CO (4×10^{-5} mbar) at 105 K and subsequently heating to higher temperatures.

Considering the rather small binding energy of CO on metal oxides, liquid helium was used to cool the sample further down to 60 K and repeated the CO adsorption measurements on ceria nanorods. The corresponding in-situ FTIR spectra are shown in Figure 5.6. Two intense CO bands are clearly observed at 2170 cm^{-1} and 2152 cm^{-1}, which shift to lower frequency compared to those observed at 105 K (see Figure 5.5), indicating an increase of the CO coverage at 60 K. Additionally, the intensity of the band at lower frequency is relatively higher than that of the 2170 cm^{-1} peak. According to the assignments derived from CO adsorption on ceria single crystals, the bands at 2170 and 2152 cm^{-1} can be definitively assigned to CO bound to the oxidized Ce^{4+} sites of (110) and (111) surfaces, respectively. Moreover, a weak IR band at around 2140 cm^{-1} is resolved, which is in agreement with the frequency of liquid-like CO on the surface. It suggests that the temperature is so low that CO is frozen at some local surface regions, which needs extra energy to overcome a diffusion barrier for the uniform distribution of CO on the surface.

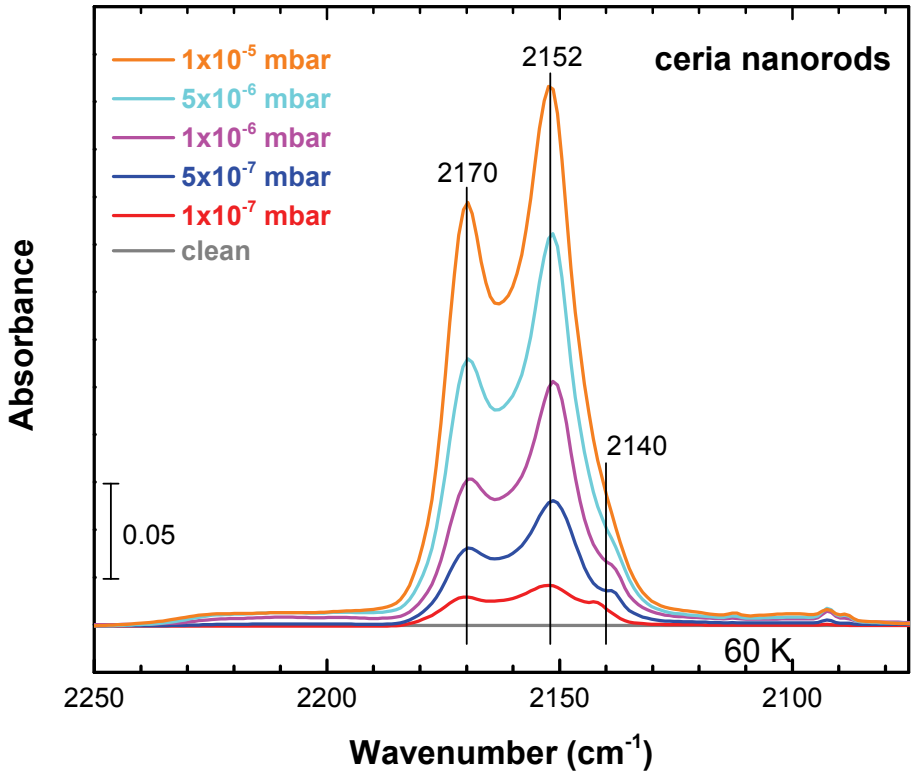

Figure 5.6 UHV-FTIR spectra recorded after exposing the ceria nanorods to different doses of CO at 60 K. The sample was annealed at 723 K for one hour under the UHV condition to remove surface impurities.

Similarly, after exposure to CO at 60 K, the IR chamber was evacuated down to 10^{-10} mbar range and then the sample was stepwise heated up to 100 K. The spectra acquired at different elevated temperatures are shown in Figure 5.7. Surprisingly, instead of decrease, the intensities of CO bands become even higher upon heating to 65 K, indicating a restructuring process of the adsorbed CO layer from non-uniform distribution at extremely low temperature (60 K) to a more homogeneous molecular environment and thereby an increase in ordering. It is interesting that upon further annealing the CO band at 2152 cm^{-1} is gradually lowered, while the 2172 cm^{-1} band increases in intensity up to 75 K. This finding suggests a thermal diffusion of adsorbed CO species from (111) nanofacets to (110) terraces, in line with the observations for CO adsorption on faceted CeO_2(110) single crystal surfaces (see chapter 4). Further heating to higher temperatures leads to the desorption of CO molecules, as demonstrated by the attenuation of both CO bands and their blueshift in frequency. Overall, on the basis of the IRRAS data obtained for various CeO_2 single crystal surfaces, the CO bands observed on ceria nanorods can be unambiguously assigned, which provides direct spectroscopic evidence that the (110) terminated ceria nanorods expose a large amount of (111) facets, as supported by Prof. Alessandro Trovarelli's HRTEM results (not shown).

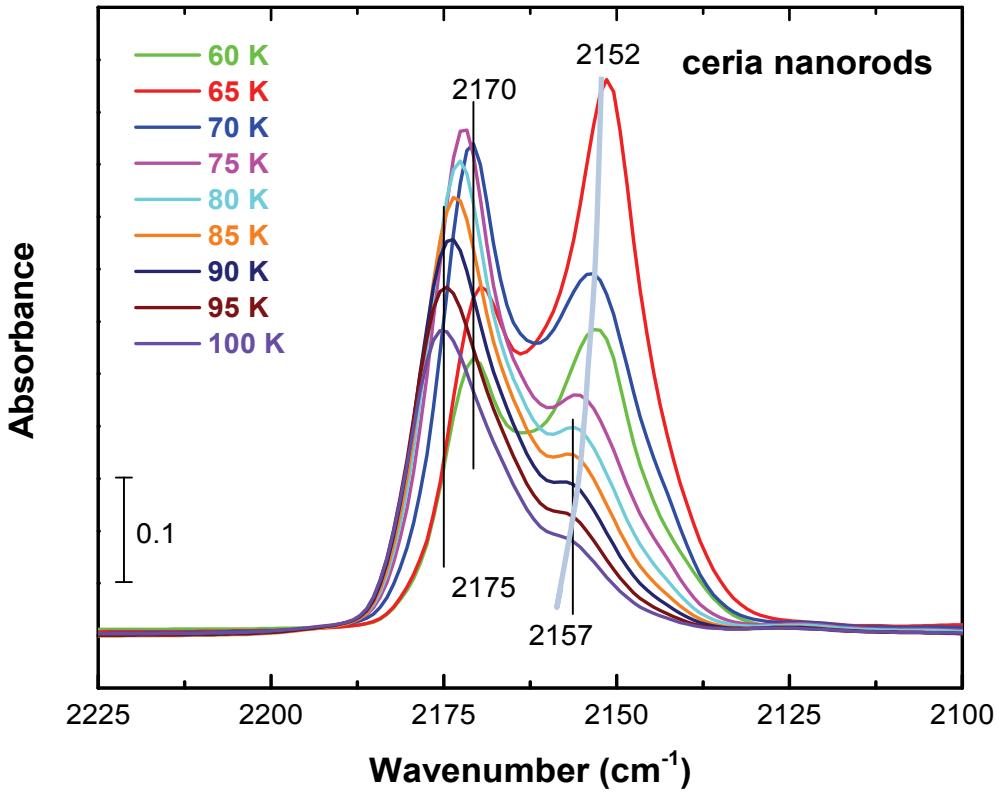

Figure 5.7 UHV-FTIR spectra recorded after exposing the ceria nanorods to CO (1×10^{-5} mbar) at 60 K and subsequently heating to higher temperatures.

5.2 CO adsorption on ceria nanocubes

Following the same procedures, ceria nanocubes were first activated by annealing to 773 K and subsequently exposed to CO of different pressures at 100 K. The corresponding in-situ IR spectra (Figure 5.8) show a predominant CO stretching mode centers at 2170 cm^{-1}, which is nearly the same frequency as that of CO adsorbed on ceria nanorods. Similar observations were also reported by previous DRIFTS work regarding room temperature CO adsorption at ceria nanorods and cubes, where CO on both nanocrystals also exhibits the same frequency at 2170 cm^{-1} [164]. On the basis of our IRRAS data obtained for well-defined single crystals (see chapter 4), this band is attributed to CO species bound to Ce^{4+} sites on (110) facets, since no CO band at around 2170 cm^{-1} was observed on the CeO_2(100) single crystal surface. Moreover, the IRRAS data shown in chapter 4 reveal that the binding energy of CO adsorbed on (100) surface is lower (complete desorption at 90 K) than that of (110) surface where CO is stable till up to 100 K. Therefore, a sample temperature of 100 K might be too high to stabilize plenty of CO molecules on (100) facets. Additionally, in the IR spectra a minor shoulder appears at 2154 cm^{-1}, which might be caused by CO adsorption on (111) and/or (100)

facets in light of the single crystal data. The difference of CO frequencies on (111) and (100) facets is not so large, and the IR bands of CO on both facets might overlap, especially considering the possibility of frequency shift caused by CO coverage and cerium oxidation states. Nevertheless, it should be noted that surface energies of these two orientations are dramatically different and therefore the probability of the presence of (100) facets especially on conventional ceria powders should be much lower than (111) facets.

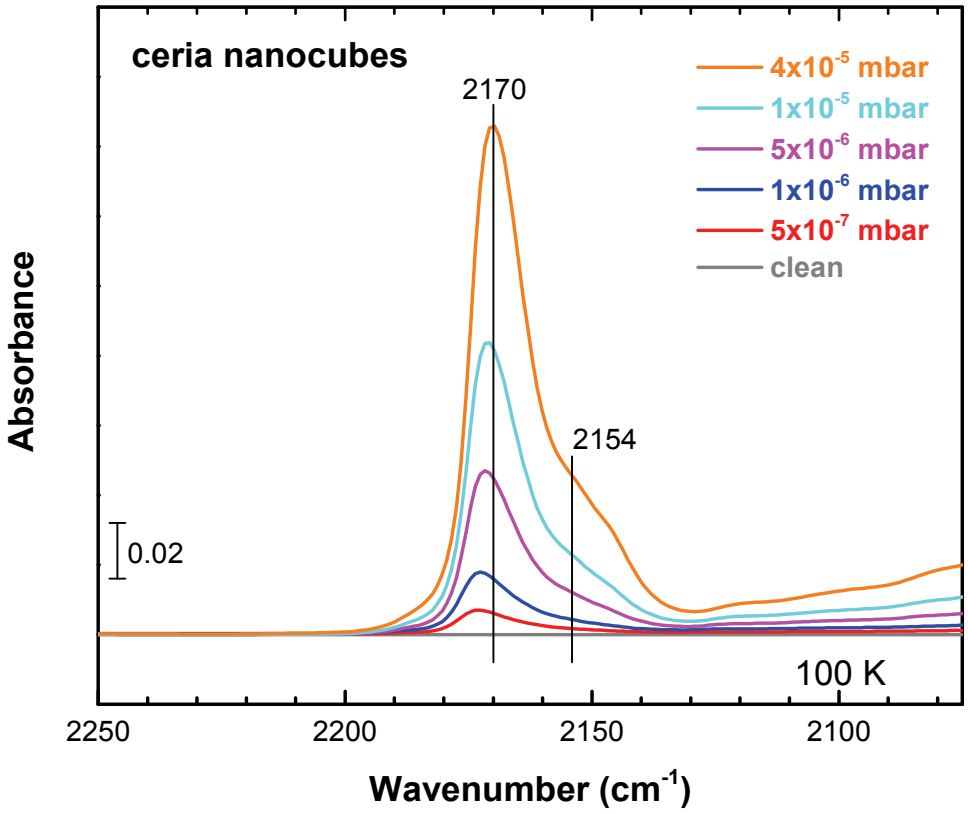

Figure 5.8 UHV-FTIR spectra recorded after exposing the ceria nanocubes to different doses of CO at 100 K. The sample was annealed at 773 K for one hour under the UHV condition to remove surface impurities.

Thermal desorption IR measurements were also conducted after CO dosing at 100 K (see Figure 5.9) and the evolution is similar as that for ceria nanorods. It is worth noting that at elevated temperatures a weak band at 2186 cm^{-1} is resolved which vanishes again upon heating to 160 K. We can safely assigned this band to CO on reduced CeO_2(110) surface on the basis of our single crystal results, which further confirms the existence of (110) facets on ceria nanocubes.

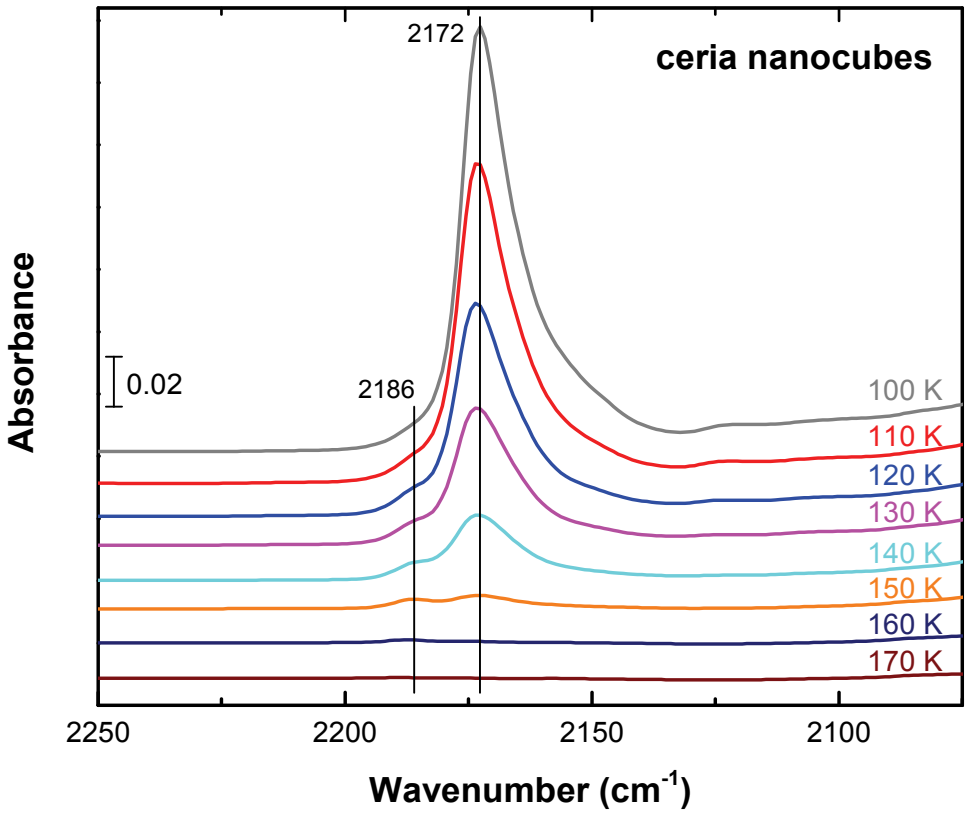

Figure 5.9 UHV-FTIR spectra recorded after exposing the ceria nanocubes to CO (4×10^{-5} mbar) at 100 K and subsequently heating to higher temperatures.

5.3 CO adsorption on conventional ceria nanoparticles

We also investigated CO adsorption on the conventional ceria nanoparticles at 100 K and the corresponding results are shown in Figure 5.10. Before exposing to CO the sample was activated by heating to 773 K in the UHV chamber. Three bands at 2172, 2164, and 2155 cm^{-1} are resolved, which can be assigned to CO bound to Ce^{4+} sites on (110) facets, to Ce^{4+}_{6c} and Ce^{4+}_{7c} sites on (111) facets, respectively. The appearance of the band at 2164 cm^{-1} is consistent with the higher reduction of the conventional nanoparticles (see Figure 5.1a) [135]. The most intense band is observed at 2172 cm^{-1}, indicating that the nanoparticles with ill-defined morphology also contain a large amount of (110) facets, even if this facet was claimed to have higher surface energy. Afterwards, thermal desorption IR measurements were performed and the data is shown in Figure 5.11.

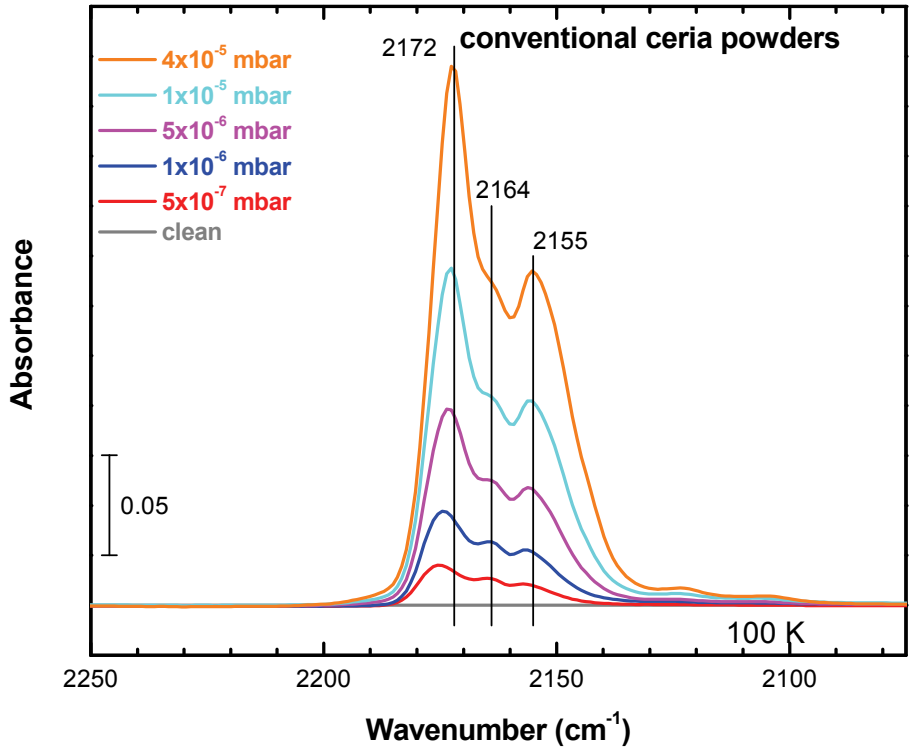

Figure 5.10 UHV-FTIR spectra recorded after exposing the conventional ceria nanoparticles to different doses of CO at 100 K. The sample was annealed at 773 K for one hour under the UHV condition to remove surface purities.

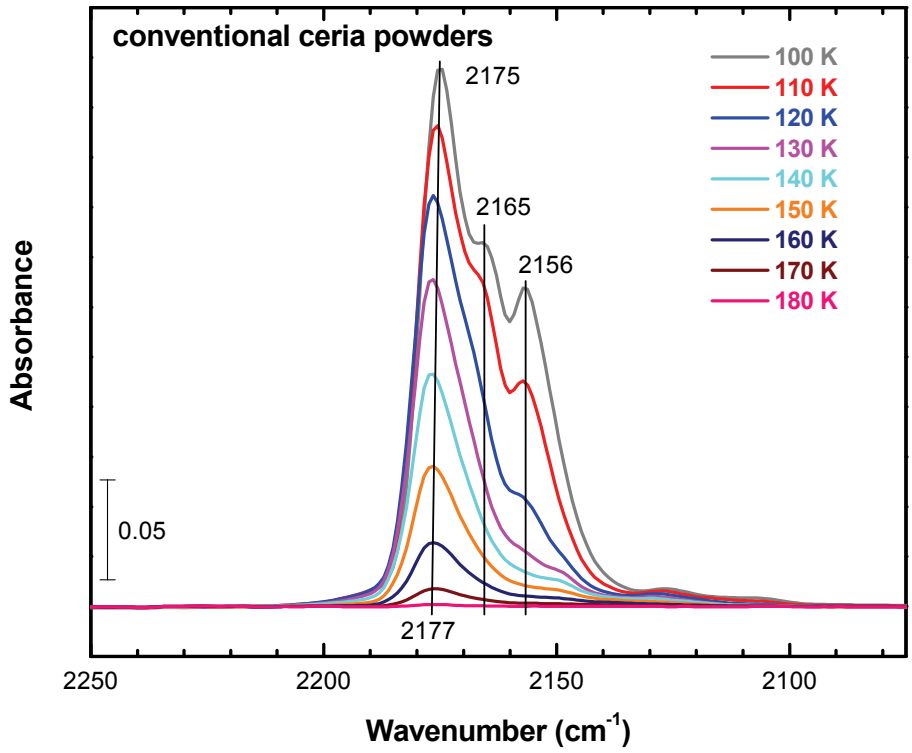

Figure 5.11 UHV-FTIR spectra recorded after exposing the ceria nanoparticles to CO (4×10^{-5} mbar) at 100 K and subsequently heating to higher temperatures.

In summary, compared the FTIR results of CO adsorption on ceria nanoparticles with those of CO on ceria (111), (110) and (100) single crystal surfaces, we can conclude that

1. Ceria nanorods are (110) terminated and expose a large amount of (111) facets. The (111) nanofaceting on (110) plane was also observed in HRTEM images.
2. Ceria nanorods and cubes show similar frequency of CO stretching mode at 2170 cm^{-1} at ~100 K, indicating that ceria nanocubes also contain substantial (110) facets. The (100) facets maybe are difficult to detect due to the lower binding energy of CO on this surface.
3. For conventional ceria nanoparticles, the CO species at 2172 cm^{-1} is also the most abundant, which suggests that these nanoparticles also contain a high density of (110) facets.

These results on ceria nanocrystals testify that our UHV-FTIRS has the capability of distinguishing surface orientations and detecting oxygen vacancies on ceria nanocrystals by using CO as IR probe. Additionally, the results here highlight that oxide nanocrystals are not always perfectly structured, in contradiction to previous assumptions. Instead, surface reconstruction, nanofaceting, and surface vacancies have to be taken into account when constructing the structure-catalysis relationship for oxide nanomaterials.

6 Methanol adsorption on ceria (110) and ceria (111)

Studying the adsorption of methanol on metal oxide surfaces is of great value, because it acts as a sensitive chemical probe to the active sites of solid catalysts [165, 166]. Among the commonly employed metal oxides, ceria (CeO_2) attracts particular interest due to its high reducibility [31]. The latter property is largely responsible for the functioning of ceria in technical applications such as three-way automotive catalysts (see, e.g. [44]).

Previous theoretical studies [167, 168] considered monomeric methanol adsorption structures at pristine and defective CeO_2(111) surfaces. The results were compared with experimental spectra obtained for polycrystalline ceria [164, 169, 170], thin films [64, 171-175], and supported nanoparticles [175]. Typically, these systems are characterized by infrared (IR) signals in the stretching region of C-O single bond between 1000 and 1200 cm^{-1} (see, e.g. [176]).

For methanol at polycrystalline ceria, references [169] and [170] discuss different IR signals at 1108, 1065 (-43), and 1015 (-93) cm^{-1} (300 K), which were attributed to atop, bridging, and tridentate methoxide species, respectively. The values in parenthesis indicate the shift of wavenumbers with respect to ν(C-O) of the supposedly monodentate methoxide. At 473 K, conversion into a formate species is observed, which comes with intense bands at ca. 1360 and 1600 cm^{-1} [64, 169, 177]. For thin films with (111) orientation, peaks similar to polycrystalline data at 1105, 1054 (-51), and 1025 (-80) cm^{-1} are observed at saturation coverage [64]. Reference [174] reports only two peaks for methanol on ceria (111) films at 1104 and 1080 (-24) cm^{-1}, while [175] reports two peaks for comparable ceria (111) films at 1108 and 1038 (-70) cm^{-1} at 100 K. Overbury and coworkers [164] studied methanol adsorption at nanocrystallites exposing different surface planes: ceria “rods” (ideally) exposing (110) and (100) facets, as well as ceria cubes and octahedra (ideally) exposing (100) and (111) facets, respectively. In the CO stretching region, IR spectra with similar features were observed for ceria rods and cubes: an intense band at ca. 1105 cm^{-1} and another broader band centered at 1035 (-70) cm^{-1}. Ceria octahedra, on the other hand, only showed a very weak band at 1109 cm^{-1}. It should be noted, however, that the nanocrystallites do not exclusively expose only one surface type. Therefore, the assignment of the vibrational features to specific ceria surface orientations is not straightforward.

To overcome the difficulties in assigning vibrational frequencies to specific ceria surface planes encountered in the interpretation of nanocrystal data [164], in this work we use macroscopic bulk single crystals exposing either (110) or (111) surfaces. Using scanning probe microscopies (STM and AFM) as well as density functional theory (DFT), previous studies revealed that the most stable step edges of nanoislands and pits on the ceria (111) surface match (110) and (100) facets as depicted in Figure 6.1 [83, 177-179]. Therefore, methanol adsorption at these step edges will also be considered in the present work.

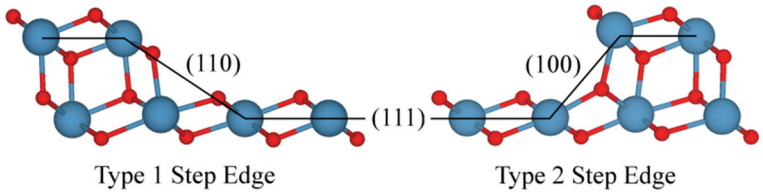

Figure 6.1 Side view along $[01\bar{1}]$ on the step edges in the ceria (111) surface studied by Neyman and coworkers [178, 179]. Black lines represent low index surface planes.

6.1 Methanol adsorption on oxidized CeO_2(110) and CeO_2(111)

Samples can be cooled down to 120 K with liquid nitrogen or to 85 K with liquid helium. The base pressure of chamber for IR measurements was below 8×10^{-11} mbar. CH_3OH (99.9%, max. 0.002% H_2O, VWR International GmbH, Germany) and CD_3OD (99.8%, Alfa Aesar GmbH, Germany) were additionally cleaned via at least three pump-freeze-thaw cycles. Methanol vapor was introduced by backfilling the IR chamber up to 1.3×10^{-10} mbar using a leak-valve-based directional doser connected to a tube (2 mm in diameter) that terminated 3 cm from the sample surface and 50 cm from the hot-cathode ionization gauge. The actual pressure in front of the sample is about 2-3 orders of magnitude larger than the total pressure in the vacuum chamber provided in Figure 6.2 and Figure 6.3. IR spectra were recorded without polarizer. Each CeO_2(110) spectrum was averaged over 1,024 scans at a resolution of 4 cm^{-1}. For the CeO_2(111) specimen, the number of scans had to be increased to 10,240 due to the smaller sample size.

Figure 6.2a shows the IRRA spectra of CH_3OH at a fully oxidized single crystalline CeO_2(110) surface at a temperature of 125 K. Only one intense band was observed at 1108 cm^{-1}. This band can be assigned in a straightforward fashion to methoxy monomers bound to the surface as monodentates (**A1**, see Figure 6.7). Figure 6.2b shows the

corresponding IRRA spectra recorded after adsorption of CD_3OD. A simple estimate considering the mass change from CH_3 to CD_3 yields a frequency shift of the CO stretch band to 1075 cm^{-1} (factor 0.97), in reasonably good agreement with the experimentally observed band at 1060 cm^{-1}. The band at 1125 cm^{-1} is assigned to CD bending modes. Almost identical results were obtained for the IR light incident along the [001] azimuthal direction (not shown).

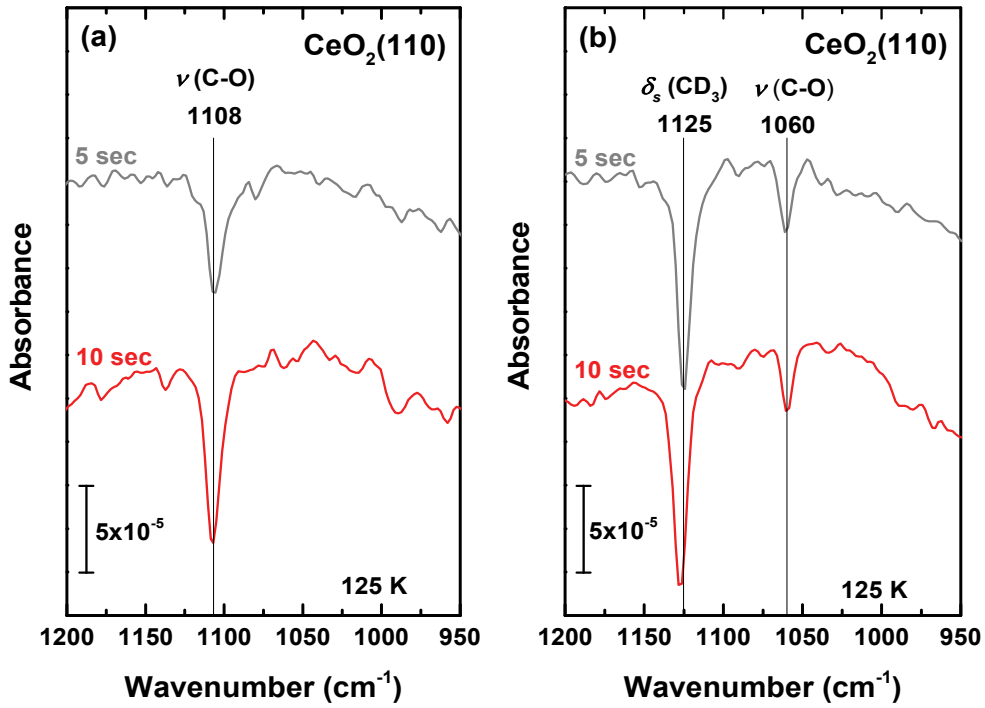

Figure 6.2 IRRA spectra of methanol (a) and deuterated methanol (b) at the fully oxidized $CeO_2(110)$ surface with the IR light incident along $[1\bar{1}0]$ azimuthal direction. The sample was exposed to 1.3×10^{-10} mbar methanol (CH_3OH or CD_3OD) vapor for 5 seconds (grey) and 10 seconds (red) at 125 K.

Figure 6.3a shows the IRRA spectra of methanol at a fully oxidized $CeO_2(111)$ surface as a function of substrate temperature. At both temperatures, strong peaks are observed at 1085 and 1060 cm^{-1}. A weak feature is visible at 1108 cm^{-1}. The intensity of this feature varied from measurement to measurement. We assign this very weak band to methanol adsorption at the small amount of (110) facets exposed at step edges in the $CeO_2(111)$ surface. Independent support for this assignment comes from measurements of the stretch frequency of carbon monoxide adsorbed on the same surface. In addition to the strong band at 2154 cm^{-1} corresponding to CO adsorption on stoichiometric $CeO_2(111)$ surface [135] a second weak band is observed at 2170 cm^{-1} (see Figure 6.4). This small band has the same frequency as

observed for CO adsorption on the fully oxidized CeO_2(110) surface. Experiments carried out for CD_3OD adsorption revealed three peaks at 1117, 1040, and 1020 cm^{-1} as shown in Figure 6.3b. The peaks at 1040 and 1020 cm^{-1} are close to the values expected for the isotope shifts (1053 and 1029 cm^{-1}, factor 0.97). The peak at 1117 cm^{-1} is assigned to a CD bending mode, as in the case of the CeO_2(110) surface. The corresponding CH bending modes are very weak and could for CH_3OH only be seen in the multilayer data (see Figure 6.5).

The observation of two bands at 1085 and 1060 cm^{-1} is unexpected. The relative intensity of these bands did not vary substantially from measurement to measurement. Performing the measurements at different temperatures (87 K and 120 K) also did not lead to changes in the relative intensity. Sauer and coworkers successfully made an assignment of these peaks based on detailed theoretical analysis described below [180]. Measurements at higher temperatures cannot be carried out on the fully oxidized surfaces, because interaction of ceria surfaces with methanol would lead to surface reduction even at around 200 K [64, 164, 171, 172, 181].

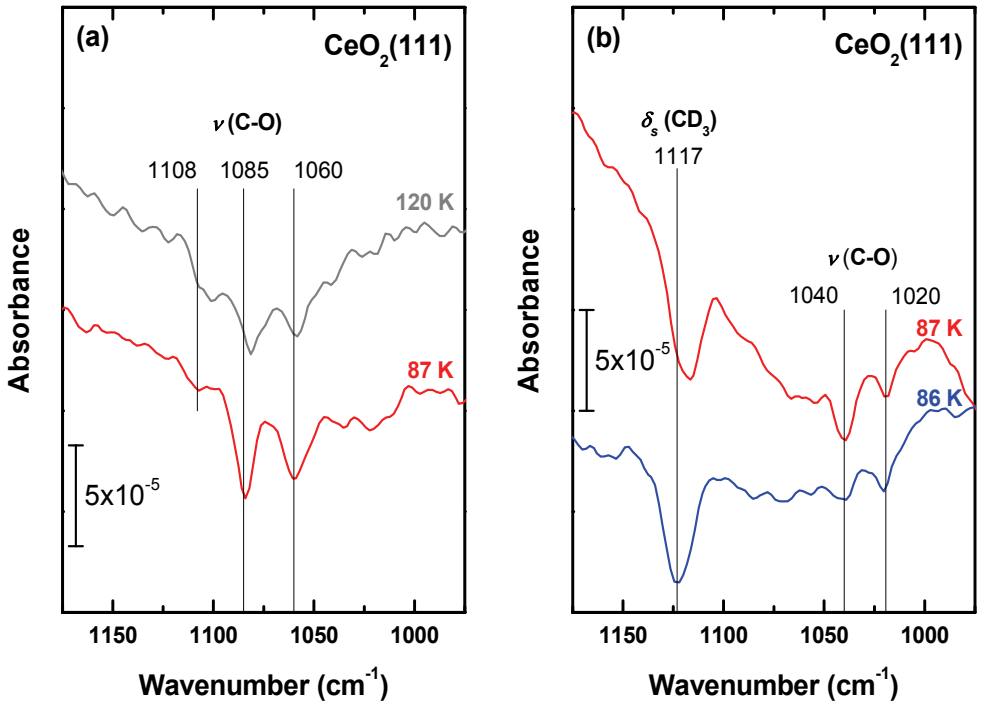

Figure 6.3 IRRA spectra of methanol (a) and deuterated methanol (b) at the fully oxidized CeO_2(111) surface. The sample was exposed to 1.3×10^{-10} mbar methanol (CH_3OH and CD_3OD) vapor for 5 seconds at indicated temperatures.

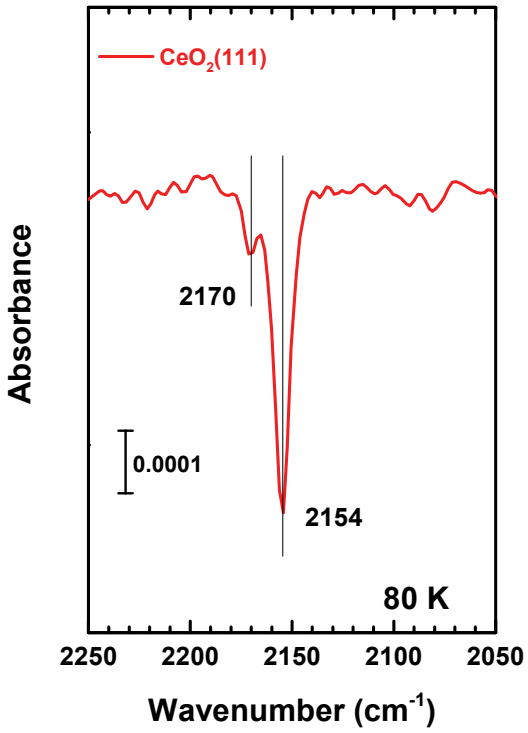

Figure 6.4 IRRA spectra of CO adsorption on the $CeO_2(111)$ (red). The sample was exposed to 1.3×10^{-10} mbar CO for 50 seconds at 80 K.

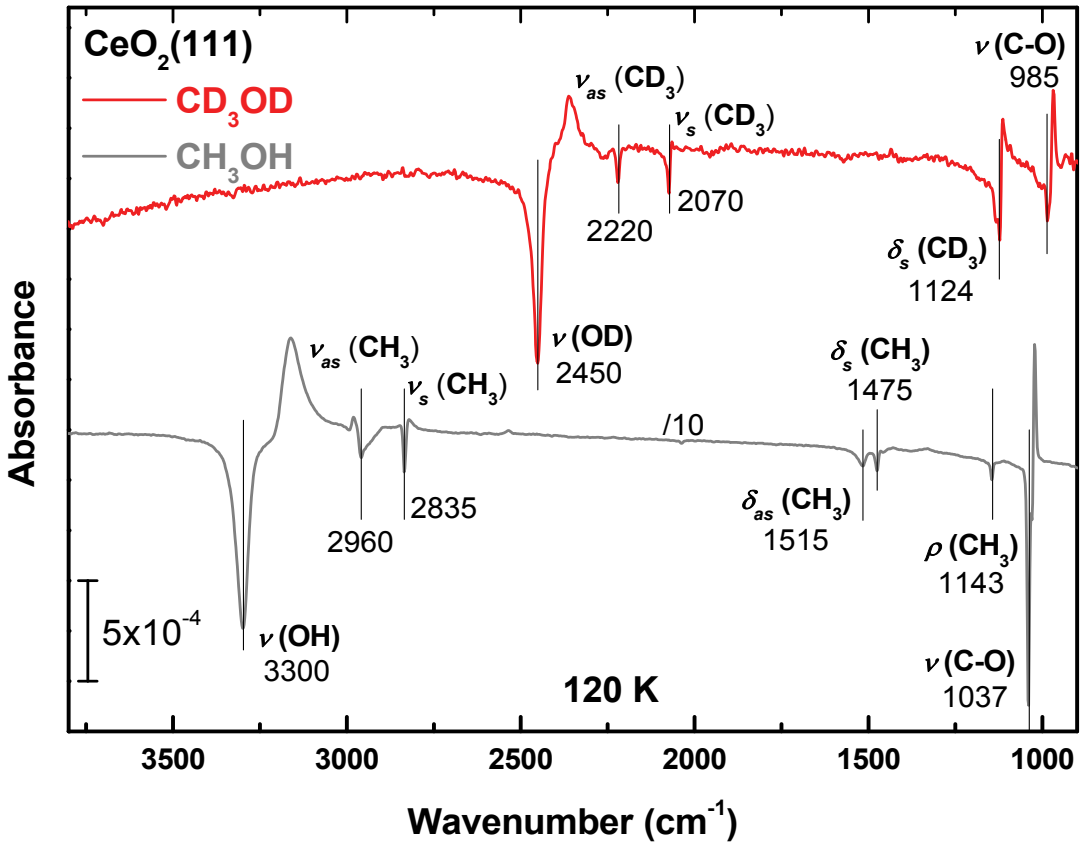

Figure 6.5 IRRA spectra of multilayer methanol (grey) and deuterated methanol (red) at the oxidized $CeO_2(111)$ surface at the substrate temperature of 120 K.

(1) First-principles calculations

First-principles calculations were conducted by Sauer and coworkers [180], and this part is adapted from the same publication.

Methanol adsorption structures on the ceria (111) surface considered by theoreticians include monomers at the pristine (**P1**), hydrogenated (**H1**), and defective (**D1**) ceria surface as well as dimers at the pristine (**P2**) and hydrogenated (**H2**) surface. Furthermore, structure **P4** (four methanol molecules on a *p*(2×2) surface slab) is used to simulate higher coverages close to a monolayer. These structures are shown in Figure 6.6 along with relevant H bond distances. Hence, they introduce the nomenclature **P*n*** (*n* = 1, 2, 4) and **H*m*** (*m* = 1 and 2), where *n* and *m* refer to the number of adsorbed methanol molecules. **D1**, **S1**, and **T1** represent adsorption structures at morphological defects such as oxygen vacancies (**D1**) and step edges (**S1** and **T1**) at low methanol coverage.

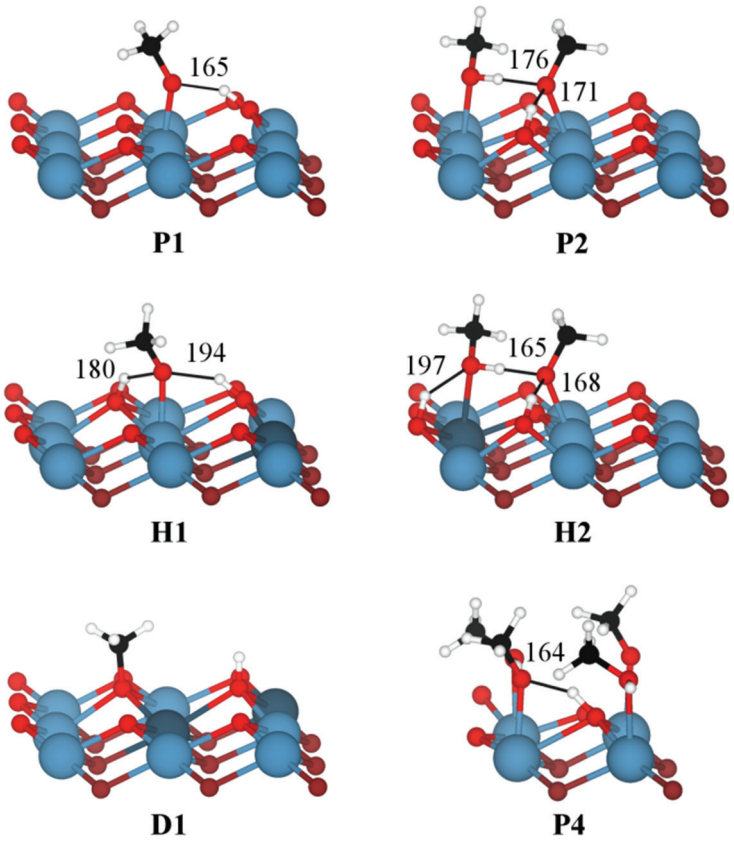

Figure 6.6 Cutouts of monomeric and dimeric methanol adsorption structures (bond distance in pm) at pristine (**P1**, **P2**), hydrogenated (**H1**, **H2**), and defective (**D1**) *p*(4×4) surface cells. Structure **P4** is calculated using a *p*(2×2) surface cell. Color code used throughout this chapter: C (black), Ce^{3+} (dark blue), Ce^{4+} (blue), H (white), and O (red).

Neyman and coworkers [178, 179] reported that hexagonal nanoislands on the ceria (111) consist of two different types of step edges: a thermodynamically more stable type 1 step edge resembling (110) facets, and a less stable type 2 step edge resembling (100) facets. This is shown in Figure 6.7.

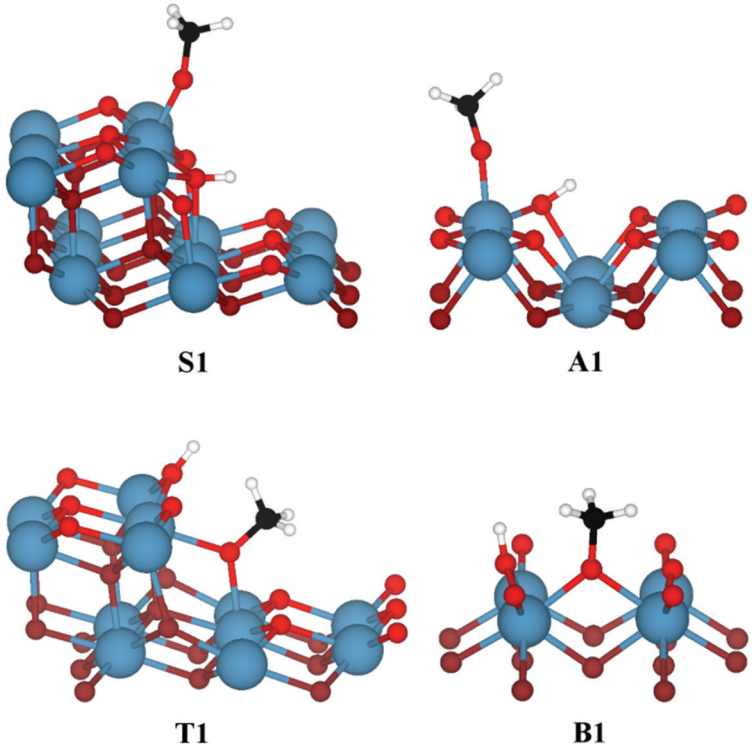

Figure 6.7 Cutouts of the methanol adsorption structures at step edges in the CeO_2(111) surface (**S1**, **T1**) as well as methanol adsorption at the ceria (110) surface (**A1**) and the (100) surface (**B1**, cf. [182]).

The surface layer of the ceria (110) surface contains both Ce and O ions. See [48, 54, 56] for a more detailed description of the (110) surface. Structure **A1** is formed upon dissociative adsorption of methanol at this surface. As shown in Figure 6.7, the surface OH group does not form a H bond to the methoxide, which is coordinated by a single Ce ion.

The methanol adsorption structures are characterized by their vibrations in the CO stretching region, i.e. CO stretching modes (ν) and methoxy rocking modes (r). CO stretching wavenumbers obtained with dispersion-corrected PBE+U are compiled in Table 6.1.

Table 6.1 Adsorption energies (E_{ads}) in kJ/mol normalized on number of methanol molecules as well as wavenumbers of CO stretching modes in cm^{-1} obtained with harmonic calculations ($\tilde{\upsilon}_{HO}$) and molecular dynamics simulations ($\tilde{\upsilon}_{MD}$). Relative shifts to the most blue-shifted mode are given in parenthesis, and relative shifts to gas phase CH_3O^- / CH_3OH ($\Delta\tilde{\upsilon}_{HO}$) are given as well.

		E_{ads}	$\tilde{\upsilon}_{HO}$	$\Delta\tilde{\upsilon}(CH_3O^-)$	$\Delta\tilde{\upsilon}(CH_3OH)$	$\tilde{\upsilon}_{MD}$
Reference				1130	1047	
Monomers:						
A1	(Ce)–**O**–CH_3 [a]	137	1099 (±0)	-31	+52	
S1	(Ce)–**O**–CH_3	124	1093 (-6)	-37	+46	1084 (-6)
P1	(Ce, H)–**O**–CH_3	88	1069 (-30)	-61	+22	1063 (-27)
H1	(Ce, 2H)–**O**–CH_3	76	1056 (-43)	-74	+9	
B1	(2Ce)–**O**–CH_3 [b]	187	1035 (-64)	-95	-12	
T1	(2Ce)–**O**–CH_3	178	1035 (-64)	-95	-12	
D1	(3Ce)–**O**–CH_3	231	1012 (-87)	-118	-35	1004 (-86)
Oligomers:						
H2	(Ce, 2H)–**O**–CH_3 [c]	91	1037 (-62),	-93	-10	1029 (-61),
	(Ce, H)–**HO**–CH_3 [c]		1012 (-87)	-118	-35	1012 (-78)
P2	(Ce, 2H)–**O**–CH_3 [c]	83	1042 (-57),	-88	-5	
	(Ce)–**HO**–CH_3 [c]		1016 (-83)	-114	-31	
P2'	(Ce, 2H)–**O**–CH_3 [c]	78	1053 (-46),	-77	+6	
	(Ce)–**HO**–CH_3 [c]		1014 (-85)	-116	-33	
P4	(Ce, 2H)–**O**–CH_3 [c]	82	1075 (-24),	-55	+28	1072 (-18),
	(Ce, 2H)–**O**–CH_3 [c]		1055 (-44),	-75	+8	1057 (-33),
	(Ce, H)–**HO**–CH_3 [c]		1020 (-79),	-110	-27	1022 (-68)
	(Ce, H)–**HO**–CH_3 [c]		1015 (-84)	-115	-32	

[a] Ceria (110) surface; [b] ceria (100) surface [182]; [c] coupled modes.

(2) Assignment of the IR bands

Methanol on the (110) Surface Only one adsorption species is observed after exposing the ceria (110) surface to methanol, which exhibits an IR band at 1108 cm^{-1}. This band is assigned to the CO stretching mode of **A1** (1099 cm^{-1}), i.e. a monodentate methoxy species with no H bond. The harmonic frequency obtained with PBE+U is 9 cm^{-1} lower than the experimental value, which is well within the expected range of accuracy for the theoretical approach [180]. Upon deuteration, the CO stretching band is red-shifted by 48 cm^{-1}, which is similar to the redshift predicted by DFT (66 cm^{-1}). The additional band at 1125 cm^{-1} is assigned to a CD bending mode of deuterated **A1** (1113 cm^{-1}).

Methanol on the (111) Surface Unexpectedly, two strong peaks at 1085 and 1060 cm^{-1} are observed for the fully oxidized (111) surface in addition to a weak shoulder at 1108 cm^{-1}. The assignment of the two strong peaks is not straightforward. Neither of them agrees in frequency with the single band observed for the monodentate methoxy species on the ceria (110) surface, the shift amounts to at least 20 cm^{-1}. At first, this observation appears to question the existence of monodenate methoxy species on this surface. The DFT results show, however, that the methoxy band for the (111) surface is substantially red-shifted relative to the (110) surface. According to DFT calculations, all CO stretching modes for methanol adsorption structures at the ceria (111) surface are predicted to occur between 1099 and 1012 cm^{-1}. Methoxy rocking modes have frequencies between 1150 and 1100 cm^{-1}, and the CH bending modes occur between 1500 and 1400 cm^{-1}. These findings are compiled in Figure 6.8.

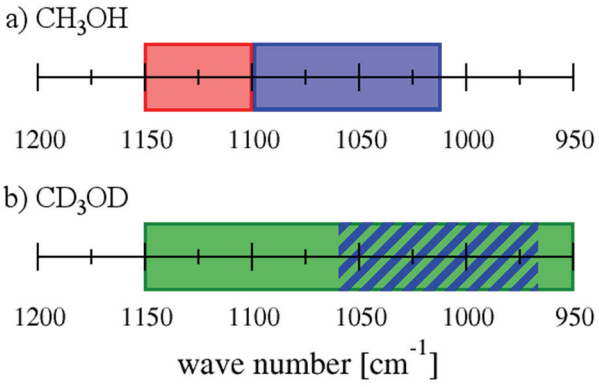

Figure 6.8 Wavenumber ranges in cm^{-1} for CH_3OH (a) and CD_3OD (b) adsorption structures at the ceria (111) surface obtained with dispersion-corrected PBE+U using the following color code: blue (CO stretching), green (CD bending), and red (methoxy rocking).

When using deuterated methanol, CO stretching modes are red-shifted by a factor of 0.97 and both CH bending and rocking modes are red-shifted by a factor of 0.71–0.75. Because of that, methoxy rocking modes occur at wavenumbers smaller than 850 cm^{-1}, while CD bending modes are observed between 1150 and 950 cm^{-1}.

On the basis of the theoretical results, Sauer and coworkers thus assign the experimental band at higher frequency (1085 cm^{-1}) to the monodentate methoxide species on the CeO_2(111), i.e. **P1**. They explain the fact that this frequency is 20 cm^{-1} lower than on the CeO_2(110) surface by the different local structure of the (111) surface, which is shown in Figure 6.9.

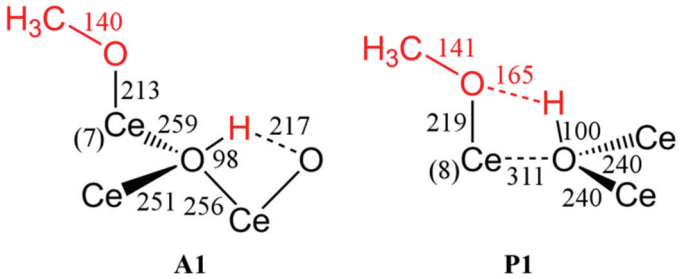

Figure 6.9 Local structure surrounding the adsorbed methoxides **A1** and **P1** with bonds lengths in pm. Coordination numbers are given in parentheses, and atoms originating from methanol are red.

The assignment of the vibration at 1060 cm^{-1} is less straightforward. According to the calculations, a second adsorption site for methoxide species is not available on the pristine (111) surface. They also feel that defects within the CeO_2(111) substrate (oxygen vacancies, step edges, etc.) do not have a sufficiently high concentration to explain the fact that this second band exhibits roughly the same intensity as the methoxide peak at 1085 cm^{-1}. A low density of defects is evidenced by the fact that when CO is adsorbed on the same surface, only one sharp vibrational band is seen, which is clearly different from the broadened band seen after intentional introduction of defects [135]. Hence, they rule out an assignment of the 1060 cm^{-1} band to any defect-induced species. The best agreement among the remaining cases studied computationally is with structure **P4**, where the high methanol coverage leads to a coupling between neighboring methoxides. The asymmetric stretching band (1055 cm^{-1}) is red-shifted by 20 cm^{-1} relative to the symmetric one (1075 cm^{-1}). Both bands are predicted to have similar intensities [180], which is in perfect agreement with the experimental spectra (Figure 6.3). Thus, they assign the unexpected second band at 1060 cm^{-1} to the CO stretch vibration of methoxy species at high coverage. This assignment yields a very good agreement between experiment and theory.

Table 6.2 summarizes the assignment to the observed bands. Note, that type 1 step edges in the ceria (111) surface resemble (110) facets. The corresponding methanol adsorption structures **S1** and **A1** are alike (cf. Figure 6.7) and yield the same CO stretching wavenumbers within the numerical accuracy of our approach (1099 and 1093 cm^{-1}). Thus, the weak experimental band at 1108 cm^{-1} is assigned to **S1**, i.e. a methoxide adsorbed at type 1 step edges. Due to the low number of coordinating ions (one Ce, no H), the CO stretching wavenumber of this methoxide species is close to the one of a methoxide anion (1130 cm^{-1}).

Table 6.2 Assignment of experimentally observed wavenumbers (cm^{-1}) to monomeric methanol adsorption structures at (110) facets (**A1**), (111) facets (**P1**), step edges (**S1**), and oxygen defects (**D1**) as well as the methanol monolayer **P4**.

$\tilde{\upsilon}_{Obsd.}$	Assignment, $\tilde{\upsilon}_{HO}$	Also observed for
1108 (±0) in Figures 6.2a, 6.3a (weak)	**A1**, 1099 (±0); **S1**, 1093 (-6)	nanoparticles: 1104 cm^{-1} [164]; polycrystallites: 1103 cm^{-1} [169], 1108 cm^{-1} [170]; thin films: 1105 cm^{-1} [64], 1104 cm^{-1} [174], 1108 cm^{-1} [175]
1085 (-23) in Figure 6.3a	**P1**, 1069 (-30); **P4**, 1075 (-24)	nanoparticles: 1077 cm^{-1} [164]; thin films: 1080 cm^{-1} [174]
1060 (-48) in Figure 6.3a	**P4**, 1055 (-44);	polycrystallites: 1050 cm^{-1} [169], 1065 cm^{-1} [170]; thin films: 1058 cm^{-1} [64]
1037 (-71) in Figure 6.5	**P4**, 1020 (-79, weak); molecular (cf. SI)	nanoparticles: 1037 cm^{-1} [164]; polycrystallites: 1031 cm^{-1} [169]; thin films: 1038 cm^{-1} [175]
	D1, 1012 (-87)	nanoparticles: 1016 cm^{-1} [164]; polycrystallites: 1015 cm^{-1} [170]; thin films: 1027 cm^{-1} [64]

The assignment proposed above is in agreement with Badri et al. [170], though it should be noted that H bonds and the number of coordinating Ce ions affect the CO stretching mode (cf. Table 6.1). These different adsorption sites arise from surface defects such as nanoislands and oxygen vacancies.

CD_3OD adsorption yields a large peak at 1117 cm^{-1} and two smaller peaks at 1040 and 1020 cm^{-1}. The latter are attributed to the shifted CO stretching modes, and the band at 1117 cm^{-1} is caused by CD bending modes, which are shifted into CO stretching region upon deuteration.

6.2 Methanol adsorption on reduced CeO_{2-x}(110) and CeO_{2-x}(111)

Figure 6.10 shows the IRRA spectrum obtained after methanol adsorption at a partially reduced single crystalline CeO_{2-x}(111) surface at a temperature of 120 K (for the degree of reduction see chapter 4). Albeit higher noise level, the spectrum still clearly demonstrates two bands located at 1075 and 1057 cm^{-1}, which only slightly downshift compared to the IR bands of fully oxidized surface. The two bands presumably are attributed to methanol adsorption on the perfect sites of (111) surface. Features at around 1020 cm^{-1} are not observed, where one expects C-O the bands of the methoxide anion in tridentate coordination to surface Ce ions (**D1** see Figure 6.6) arising from methanol adsorbed into the oxygen vacancy sites. According to a recent theoretical study [168], the tridentate methoxide does not show IR-active vibrations in this region which may explain the absence of CO vibrational bands.

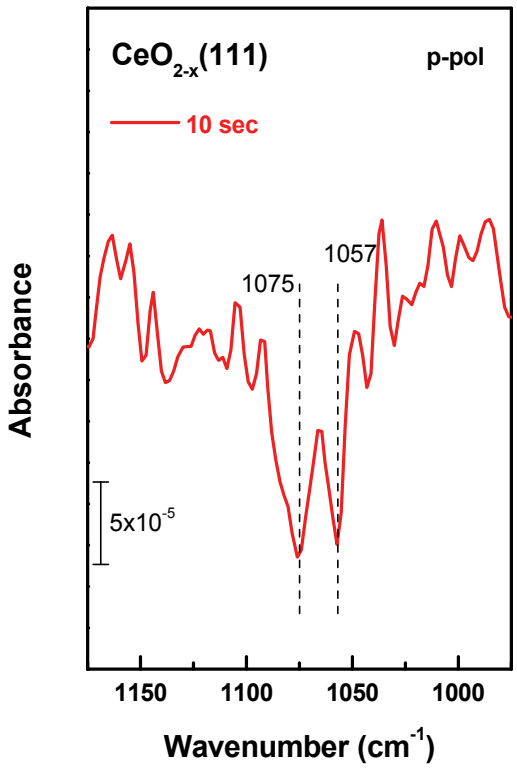

Figure 6.10 IRRA spectrum of methanol at the partially reduced CeO_{2-x}(111) surface. The sample was exposed to 1.3×10^{-10} mbar CH_3OH vapor for 10 seconds at 120 K.

Figure 6.11 shows the IRRA spectra of methanol adsorption at a partially reduced single crystalline CeO_{2-x}(110) surface at 115 K (for the degree of reduction see chapter 4). Apart from the band at 1108 cm^{-1} originating from monodentate methoxy species (**A1**, see

Figure 6.6) on perfect sites of (110) surface, one additional band appears at 1070 cm^{-1}. Considering it is facile to form (111) facets during CeO_2(110) reduction by high temperature annealing under UHV conditions (see chapter 4), the band at lower frequency might be assigned to methoxide species formed on (111) facets (**P1**). As the methanol coverage increases, another band at 1055 cm^{-1} caused by molecularly adsorbed methanol arises (not shown).

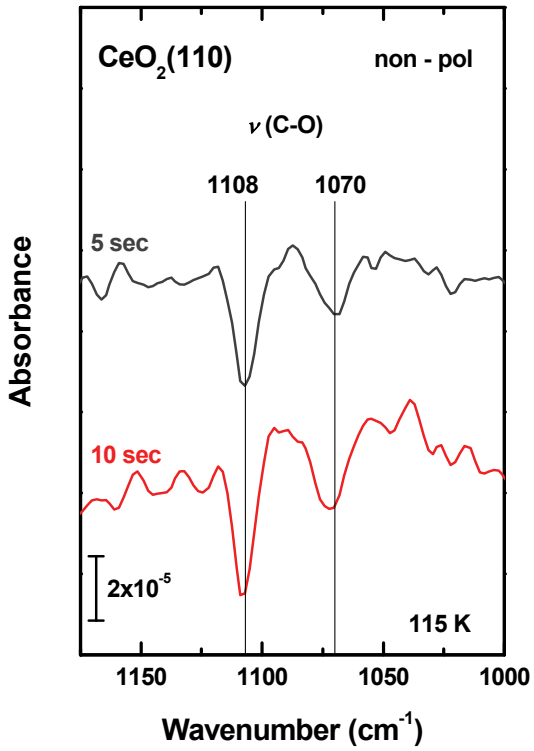

Figure 6.11 IRRA spectra of methanol at the partially reduced CeO_{2-x}(110) surface with the IR light incident along [001] azimuthal direction. The sample was exposed to 1.3×10^{-10} mbar methanol (CH_3OH) vapor for 5 seconds (grey) and 10 seconds (red) at 115 K.

In brief, for methanol adsorbed at the oxidized ceria (110) surface, infrared reflection adsorption spectra show a single band at 1108 cm^{-1}, which is assigned to a monodentate methoxide species. For the fully oxidized (111) surface, two peaks are observed at 1085 and 1060 cm^{-1} in addition to a weak signal at 1108 cm^{-1}. The latter is assigned to methanol adsorbed at step edges on the ceria surface, which resemble (110) facets. According to the Density functional theory (DFT) calculations, the two strong bands are assigned to a methanol monolayer at the pristine (111) surface that consists of H-bonded methoxide as well as molecularly adsorbed methanol species. Ab initio MD simulations for this monolayer yield

two strong bands at 1075 and 1055 cm^{-1} that correspond to the symmetrically and asymmetrically coupled CO stretching modes of neighboring methoxide species.

For methanol adsorbed at partially reduced ceria (111) surface, no new bands were observed in spite of a slight redshift of both bands. The absence of tridentate methoxide bands correlating with oxygen vacancies is probably due to its IR-inactive character. For the reduced ceria (110) surface, a new band at around 1070 cm^{-1} appeared, which might be attributed to methanol adsorption on (111) facets formed on the reduced ceria (110) surface.

7 CO_2 adsorption on ceria (110)

Carbon dioxide (CO_2) studies were motivated by not only the mitigation of this greenhouse gas but also the potential utilization of CO_2 as a feedstock for the chemical industry [183]. Nowadays, CO_2 is industrially employed to produce chemicals such as urea, methanol, ethylene carbonate, and salicylic acid. A detailed understanding of the surface chemistry of carbon dioxide is crucial for the design and optimization of catalysts [184-186].

Ceria, as one of the most reducible metal oxides, has proven to be a viable catalyst for CO_2 involved reactions. Graciani et al. reported a highly active copper–ceria catalyst with Cu(111) after depositing ~0.2 ML of CeO_x nanoparticles for methanol synthesis from CO_2 [187]. Hilaire et al. measured the water-gas shift reaction rates for Me/CeO_2 (Me: Pd, Ni, Fe, Co), and pure ceria [188]. Yamanaka and coworkers demonstrated the direct partial oxidation of methane to synthesis gas by cerium oxide [189]. Sharma et al. claimed that CO_2 is able to oxidize reduced ceria [190]. Makkee and co-workers studied the oxygen exchange mechanism between $C^{18}O_2$ and ceria on both Pt/CeO_2 and bare CeO_2 samples [191].

Besides studies at high-surface-area CeO_2 catalysts under realistic reaction conditions, the fundamental research which takes a surface science approach regarding CO_2 adsorption and reactions at surfaces of well-ordered CeO_2 single crystals or oriented thin films has also been conducted.

In Senanayake and Mullins's study of the redox pathways for formic acid decomposition over CeO_2(111) surfaces, they also examined the adsorption of CO_2 on CeO_2(111) in order to make a distinction between carbonate (CO_3^{2-}) and formate ($HCOO^-$) species [192]. Carbonate and formate have similar binding energies of C1s at ~290 eV. However, C K-edge NEXAFS can unambiguously distinguish between carbonate and formate which have their resonances of π^* transition at 290.5 and 288 eV, respectively. Libuda and coworkers have investigated adsorption and activation of CO_2 on ceria and magnesia/ceria thin films using various photoelectron spectroscopies and have also demonstrated the re-oxidation of reduced ceria by CO_2 [193-195]. They exposed pure reduced CeO_{2-x}(111) to CO_2 at room temperature resulting in two peaks in the C1s region at 289.5 and 285.8 eV, which were assigned to carbonate (CO_3^{2-}) and carboxylate ($CO_2^{\delta-}$), respectively [193]. However, the carboxylate peak (285.8 eV) was observed only after CO_2 exposure higher than 4000 L. Under such high exposures to CO_2,

they think partial re-oxidation of reduced ceria by CO_2 occurs with high reaction probability even at temperatures as low as 300 K, on pure ceria in the absence of both supported noble metal particles and surface hydroxyl groups [195]. They also determined that the surface carbonate species on reduced ceria samples decomposes upon annealing above 400 K. Stoichiometric CeO_2(111), by contrast, did not adsorb CO_2 at room temperature [194]. No C1s signal appeared even after exposing stoichiometric CeO_2(111) to 14,200 L of CO_2. Hutter and coworkers have investigated the adsorption properties of CO_2 on a CeO_2(111) surface with standard DFT calculations using the PBE exchange-correlation functional and concluded that CO_2 adsorbs onto the CeO_2(111) surface as monodentate carbonate species up to a coverage of 1/3 ML, though the adsorption energy is relatively weak (0.31 eV) [196]. A CO_2 molecule adsorbed in a bent configuration (carboxylate or carbonate species) acts as a Lewis acid which accepts electronic charge from the ceria surface at all coverages. Higher coverages of CO_2 adsorption result in the formation of a linear, physisorbed CO_2 species. The average binding energy in such configurations has been shown to increase marginally at 1 ML, since the first partial layer of linear CO_2 is stabilized by the pre-adsorbed monodentate carbonate species.

More recently, Mullins and coworkers [197] have revealed a much stronger interaction of CO_2 with both oxidized and reduced ceria (100) film surfaces. Synchrotron-based XPS and C K-edge NEXAFS combined with DFT+U calculations determined that CO_2 is adsorbed as a tridentate carbonate with the molecular plane parallel to the (100) surface. For the reduced $CeO_{1.7}$(100) exposed to CO_2 at 180 K, no CO desorbs during the CO_2 TPD, which indicates that CO_2 does not re-oxidized $CeO_{1.7}$(100) surface under the measuring conditions.

To date only theoretical study on ceria (110) surface has been reported. Cheng et al. [198] have explored various adsorption sites and configurations for CO_2 on stoichiometric and reduced ceria (110) using density functional theory with the Hubbard U correction. Eleven different configurations for CO_2 adsorption on the stoichiometric (110) surface were examined and they found that the molecule does not form carbonate but is physisorbed as CO_2. By contrast, carbonate species is formed on reduced CeO_{2-x}(110). They considered two different models for the reduced CeO_{2-x}(110) surface with either an in-plane oxygen vacancy or a split oxygen vacancy. The in-plane O-vacancy is formed by simply removing an O from the surface, while the split O-vacancy is produced when an O adjacent moves toward that vacancy into a bridge site between two Ce cations. CO_2 adsorbs at the in-plane vacancy as a

carboxylate with the C and one O atom in the molecule bound to two Ce cations. However, CO_2 adsorption at the split vacancy leads to the formation of a monodentate carbonate with higher adsorption energy.

In this chapter, the first experimental results of CO_2 adsorption onto a bulk single crystal $CeO_2(110)$ are reported. C1s and O1s synchrotron-based XPS and C K-edge NEXAFS data indicate that CO_2 adsorbed predominantly as carbonate species on both oxidized $CeO_2(110)$ and partially reduced $CeO_{2-x}(110)$ at low temperatures.

The $CeO_2(110)$ single crystal was prepared by repeated cycles of sputtering with 1 keV Ar^+ and annealing at 800 K for 15 min in an O_2 atmosphere of 1×10^{-5} mbar to form a stoichiometric surface, or alternatively without O_2 to create a reduced one. The degree of reduction has been estimated to be ~60% Ce^{3+} ($CeO_{1.7}(110)$) in chapter 4, which is reproducible. Figure 7.1 shows the valence band photoemission spectra of oxidized and reduced ceria (110) surfaces. For temperature monitoring, a K-type thermocouple was directly attached on the sample surface. XPS measurements were carried out to ensure sample cleanliness and to determine oxidation state of cerium from Ce4d and valence band photoemission spectra. XP spectra can only be recorded at the sample temperature above 150 K since lower temperatures induce severe charging problems.

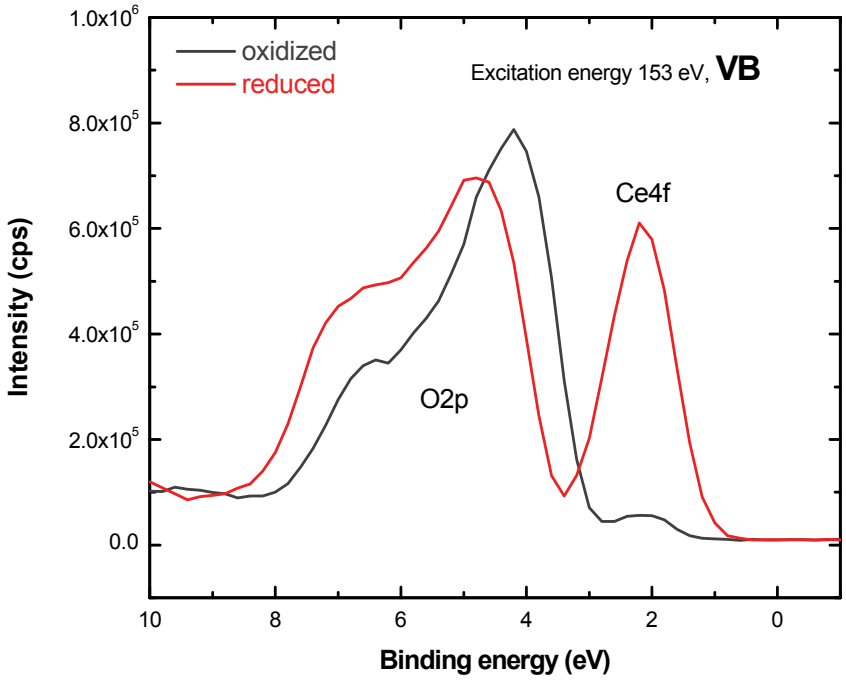

Figure 7.1 Valence band photoemission spectra of oxidized $CeO_2(110)$ (grey) and a surface that has been reduced to ~60% Ce_{3+} ($CeO_{1.7}(110)$).

NEXAFS measurements only were performed after desired Ce oxidation state as judged by XPS. Exposure to 5 L CO_2 at sample temperatures typically below 120 K was achieved by backfilling the analysis chamber up to 10^{-9} mbar. Typical base pressures during acquisition of NEXAFS and XP spectra were 2×10^{-10} mbar. NEXAFS and XP spectra after CO_2 exposure were firstly recorded at low temperatures. And then the sample temperature was elevated to a set of given temperatures and the corresponding spectra were acquired during thermal desorption process.

7.1 CO_2 adsorption on reduced CeO_{2-x}(110)

The XPS and NEXAFS measurements of CO_2 adsorption were firstly performed on reduced CeO_{2-x}(110) surfaces. Figure 7.2 shows C1s core-level XP spectra for CO_2 adsorption on reduced CeO_{2-x}(110). The reduced CeO_{2-x}(110) was exposed to 5 L of CO_2 at 120 K and subsequently heated to the indicated temperatures. All spectra were recorded at the elevated temperatures. The spectra consist of a primary peak at 290.5 eV.

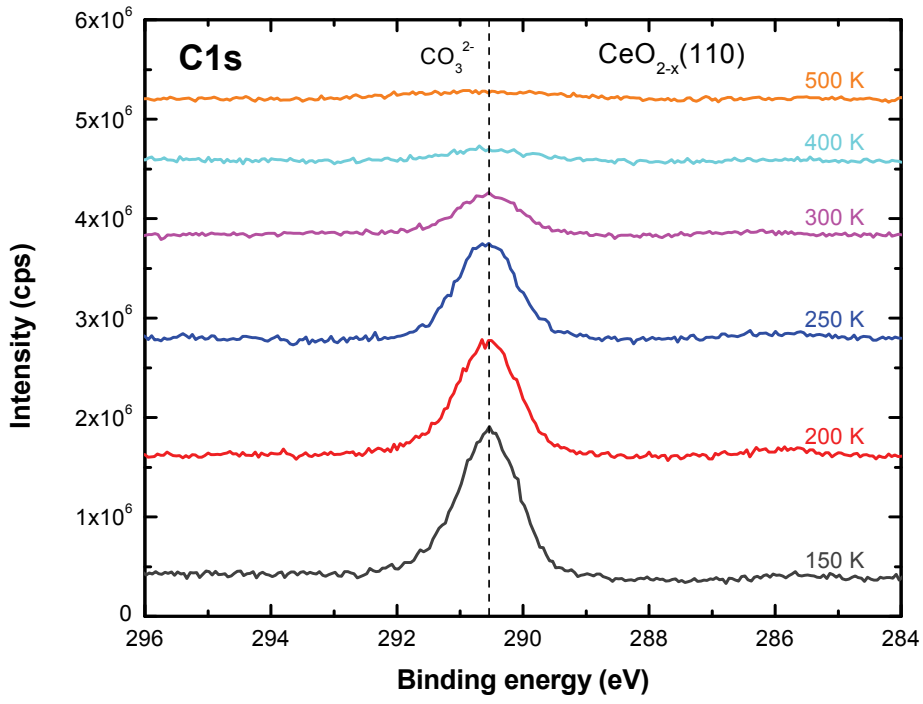

Figure 7.2 C1s core-level XP spectra following a dose of 5 L CO_2 at 120 K and annealed as indicated on reduced CeO_{2-x}(110).

As shown in Figure 7.2, one C1s peak is observed at 290.5 eV which is assigned to carbonate (CO_3^{2-}) species. Similar assignment has been made for carbonates on α-Cr_2O_3(10-12) [199]

and ZnO [200, 201]. This assignment is also in agreement with that of Mullins et al. for CO_2 adsorption onto CeO_2(111) [192] and CeO_2(100) [197] films at low temperatures, and also with Rodriguez et al. for CO_2 adsorption onto CeO_x/Au(111) – ceria nanoparticles supported on Au(111) [202]. A small shoulder at ~292 eV in the 150 K spectrum is ascribed to a tiny amount of physisorbed CO_2, which was totally desorbed by heating up to 250 K. The intensity of the peak at 290.5 eV dwindled with rising of temperature and was extinguished entirely by 500 K. Neither a significant shift of this peak in the binding energy nor the emergence of any new features with annealing temperature was observed.

Figure 7.3 presents O1s core-level XP spectra for CO_2 adsorption on reduced CeO_{2-x}(110). Peaks at 535.2, 533.0, and 531.0 eV are assigned to molecularly physisorbed CO_2, carbonate (CO_3^{2-}), and lattice O, respectively [197]. The intensity of the carbonate O1s peak at 533.0 eV decreased with increasing temperature in a qualitatively similar manner as that of the carbonate C1s peak (cf. Figure 7.2); the peak intensity diminished gradually over the temperature range from 150 to 500 K, until the peak became nearly extinct by 500 K. The variation of the lattice O intensity is due to both attenuation of lattice O induced by the covered carbonate and conversion of surface (lattice) O to carbonate following CO_2 adsorption.

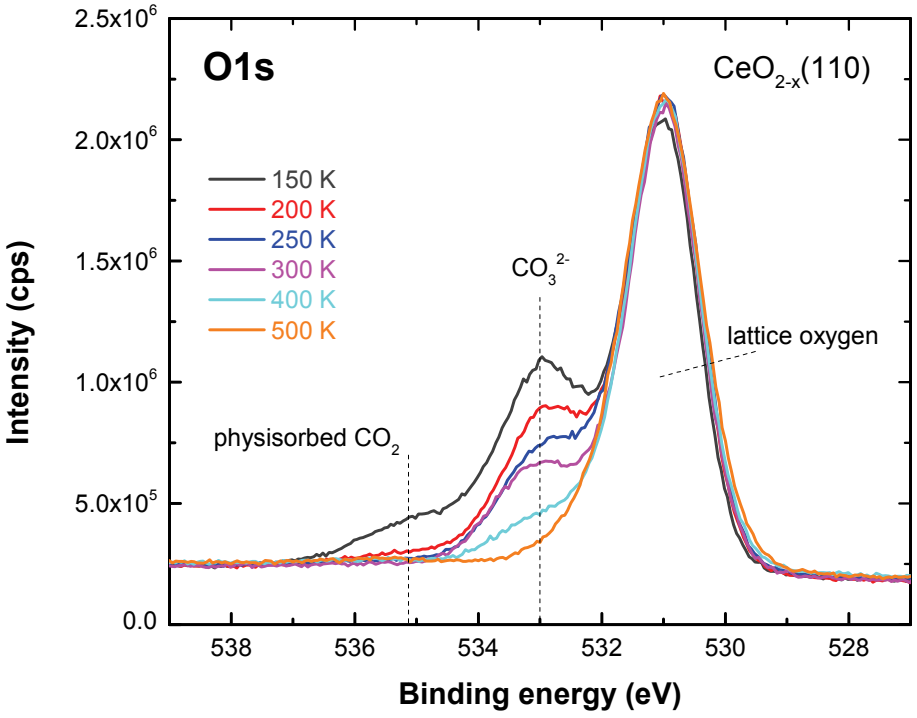

Figure 7.3 O1s core-level XP spectra following a dose of 5 L CO_2 at 120 K and annealed as indicated on reduced CeO_{2-x}(110).

Near-edge X-ray absorption fine structure (NEXAFS) spectra at different angles (30, 55, 90°) of incidence were acquired (data not shown). However, obvious angular dependence was not observed indicating that the adsorbed species have no preferential orientation on reduced CeO_{2-x}(110) surface. The C K-edge NEXAFS spectra for the reduced CeO_{2-x}(110) surface exposed to 5 L of CO_2 at 120 K and subsequently annealed to 200 and 300 K are shown in Figure 7.4, where each spectrum is the average of spectra recorded at different angles. One single peak at 290.5 eV and another broader, shallower peak at around 301.5 eV are assigned to π* and σ* transition of carbonate (CO_3^{2-}), which is in agreement with the assignments of Mullins and coworkers for CO_2 adsorption on CeO_2(111) [192] and CeO_2(100) [197]. The noise of the spectra in the σ* transition range results from subtraction of third-order X-ray excitation at the Ce M_{IV} and M_V edges (absorption peaks at photon energies of 295 and 301.5 eV, respectively) from the raw NEXAFS spectra. The spectral intensities have been normalized to the absorbance or "jump" at 320 eV. The primary effect of annealing the sample was a decrease in the carbonate coverage. The C K-edge NEXAFS data confirmed our assignment of carbonate as the only species on the surface for temperature above 250 K. The π* transition for carbonate at 290.5 eV was clearly distinguished from that of either carboxylate [203, 204] or formate [192, 205] whose π* resonance would occur at 288–289 eV. The π* peak due to carbonate was located at a similar photon energy on various ZnO single crystal surfaces; specifically, 290.5, 290.4 ± 0.2, and 290.4 ± 0.5 eV for ZnO(10-10) [206], ZnO(000-1)-O [207], and ZnO(0001)-Zn [208], respectively.

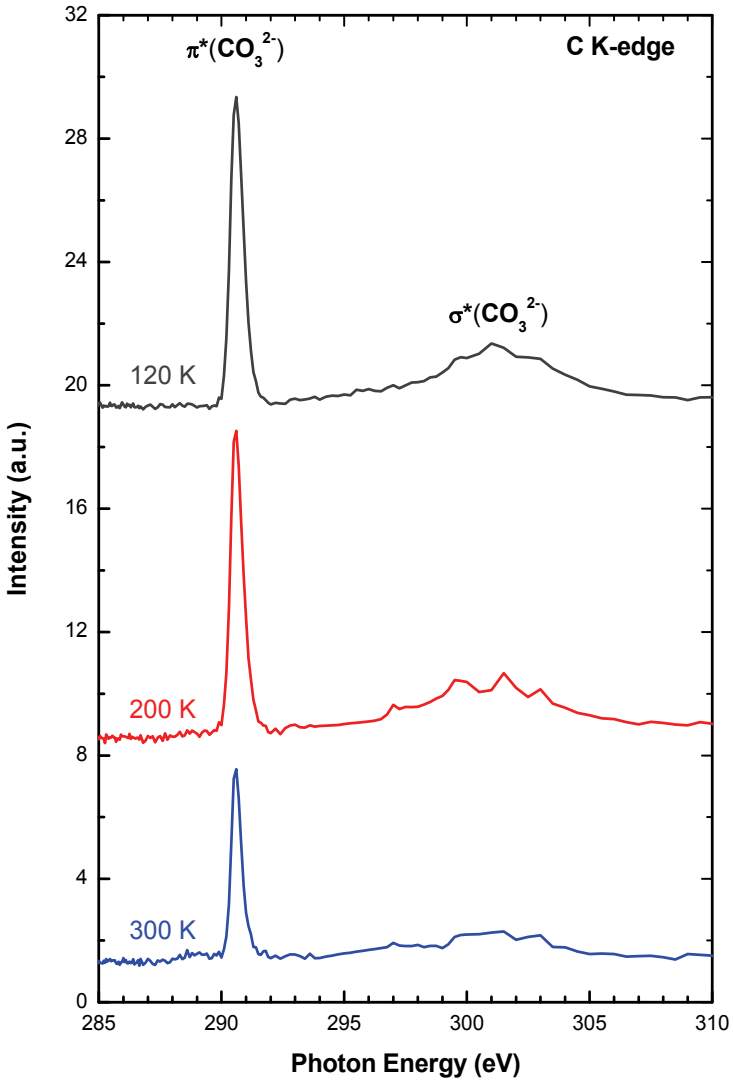

Figure 7.4 Near-edge X-ray absorption fine structure (NEXAFS) spectra at the C K-edge following a dose of 5 L CO_2 at 120 K and annealed as indicated on reduced CeO_{2-x}(110).

It is surprising that CO_2 can be readily adsorbed on reduced CeO_{2-x}(110) surface at room temperature (cf. Figure 7.5). C1s and O1s XP spectra show the same main features as those of CO_2 adsorption on reduced CeO_{2-x}(110) at low temperatures. The adsorbed species are carbonate, as evidenced also by their stabilization at high temperatures, since carboxylate ($CO_2^{\delta-}$) species are believed not stable in UHV at room temperature [187].

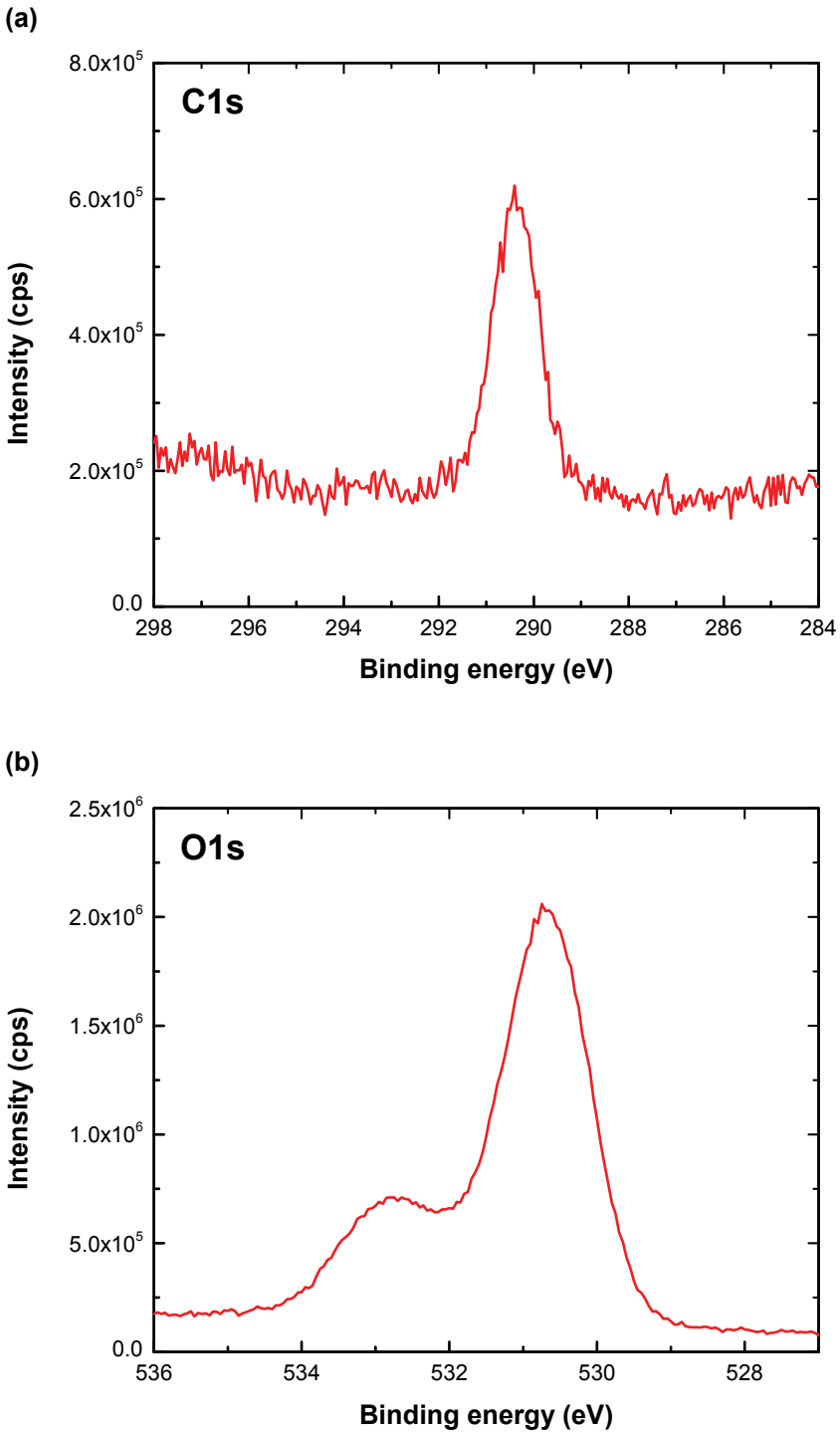

Figure 7.5 C1s (a) and O1s (b) core-level XP spectra following a dose of 1 L CO_2 at room temperature on reduced CeO_{2-x}(110).

7.2 Charge transfer between reduced $CeO_{2-x}(110)$ and CO_2

Libuda and coworkers [193, 195] examined the re-oxidation of the reduced $CeO_{2-x}(111)$ film grown on Cu(111) by CO_2 and observed that a significant amount of Ce^{3+} was oxidized to Ce^{4+}. However, Mullins and coworkers [197] did not detect CO desorption during CO_2 TPD from reduced $CeO_{1.7}(100)$ following CO_2 exposure at 180 K. Additionally, White and coworkers [209] also did not observe CO formation when CO_2 was dosed to pure ceria particles at 300 K and subsequently evacuated at higher temperatures.

To settle the controversy over whether the reduced ceria can be re-oxidized by CO_2, reduced $CeO_{2-x}(110)$ was exposed to 5 L CO_2 at 200 K, and subsequently the sample was flashed up to 500 K to completely remove the adsorbates. Normal emission valence band spectra (cf. figure 7.6) of reduced $CeO_{2-x}(110)$ before and after CO_2 treatment were recorded at 200 K. No change of Ce4f and O2p peaks upon CO_2 treatment was detected, which indicates that CO_2 did not re-oxidize reduced $CeO_{2-x}(110)$.

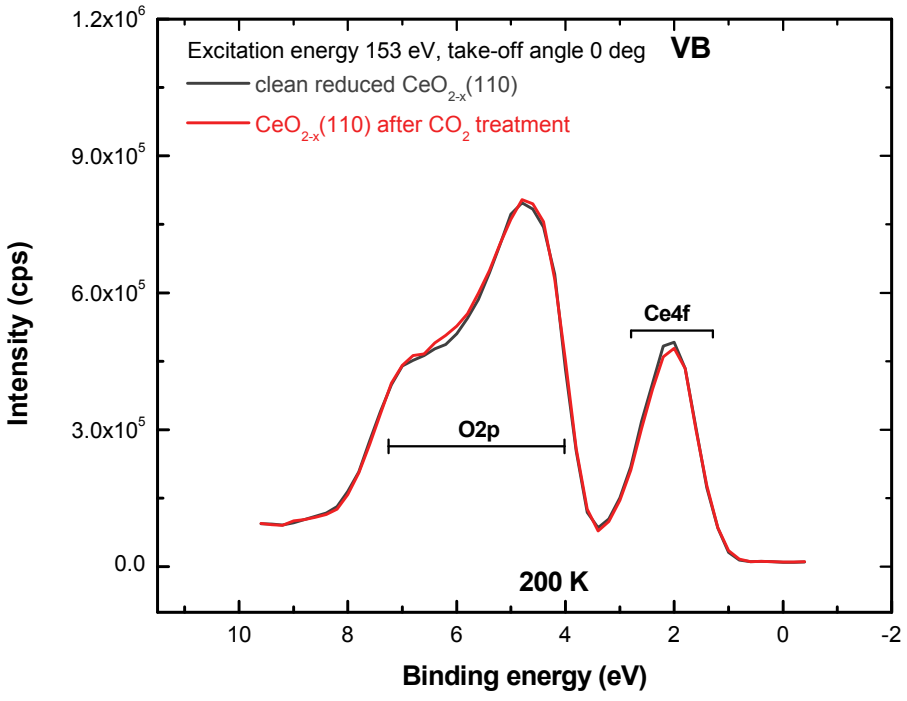

Figure 7.6 Normal emission valence band spectra of clean reduced $CeO_{2-x}(110)$ (grey) and $CeO_{2-x}(110)$ after CO_2 treatment (red).

The same experiment was repeated, while valence band spectra (cf. figure 7.7) were recorded at room temperature and at a take-off angle of 55 degree, which provides information from

atomic layers more close to the sample surface. Again, no change in Ce4f peak of CeO_{2-x}(110) was seen before and after CO_2 treatment, revealing that CO_2 does not oxidize the reduced CeO_{2-x}(110) in agreement with previous observations by Mullins [197] and White [209].

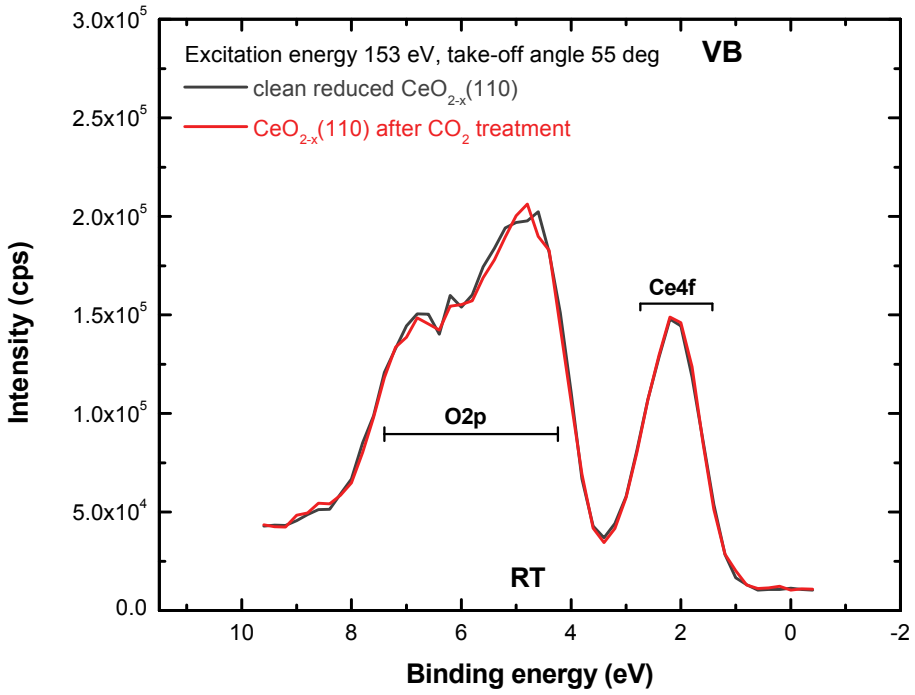

Figure 7.7 Grazing emission valence band spectra of clean reduced CeO_{2-x}(110) (grey) and CeO_{2-x}(110) after CO_2 treatment (red).

The reason why Libuda and coworkers [193, 195] observed the re-oxidation of a large amount of Ce^{3+} to Ce^{4+} on the reduced CeO_{2-x}(111) film is probably because they conducted the measurements in CO_2 atmosphere where the samples were always covered with CO_2. According to a recent theoretical study [198], on the reduced CeO_{2-x}(110) surface upon CO_2 adsorption a net charge of ca. -|e| is transferred from Ce^{3+} to the activated CO_2 molecule, and then this cerium cation is re-oxidized to Ce^{4+}. Nonetheless, upon heating the adsorbates desorb in the form of CO_2 not CO due to higher activation barrier of CO_2 dissociation than CO_2 desorption, thus the negative charge is transferred back to surface Ce^{4+} and form Ce^{3+} again.

7.3 CO_2 adsorption on oxidized CeO_2(110)

Similarly, the XPS data of CO_2 on oxidized CeO_2(110) surface is presented firstly. Figure 7.8 shows C1s core-level XP spectra for CO_2 adsorption on oxidized CeO_2(110). There are several points of contrast with regard to CO_2 adsorption on reduced CeO_{2-x}(110). The spectra consist of a primary peak at 289.7 eV and a weak feature at 285.0 eV. For the primary peak at 289.7 eV, the intensity was less at all temperatures and the peak was located at lower binding energy compared to that of the reduced surface. The shift of XPS peak positions is a typical effect of surface reduction which has also been observed for O1s, C1s, and S2p core levels when other molecules were adsorbed on oxidized and reduced ceria (100) and (111) [172, 173, 192, 210, 211]. The shift to lower binding energy does not therefore represent a different species compared to the reduced surface; and the peak at 289.7 eV is then also assigned to carbonate (CO_3^{2-}), which is not in agreement with the theoretical results of Cheng et al. [198] for CO_2 adsorption on oxidized CeO_2(110) surface. The feature at 285.0 eV is tentatively assigned to residual contamination in the form of graphite or CH_x hydrocarbon fragments, referred as C^0. The intensity of carbonate peak shrinks steadily by increasing the temperature, and the adsorbed species could be present up to 400 K.

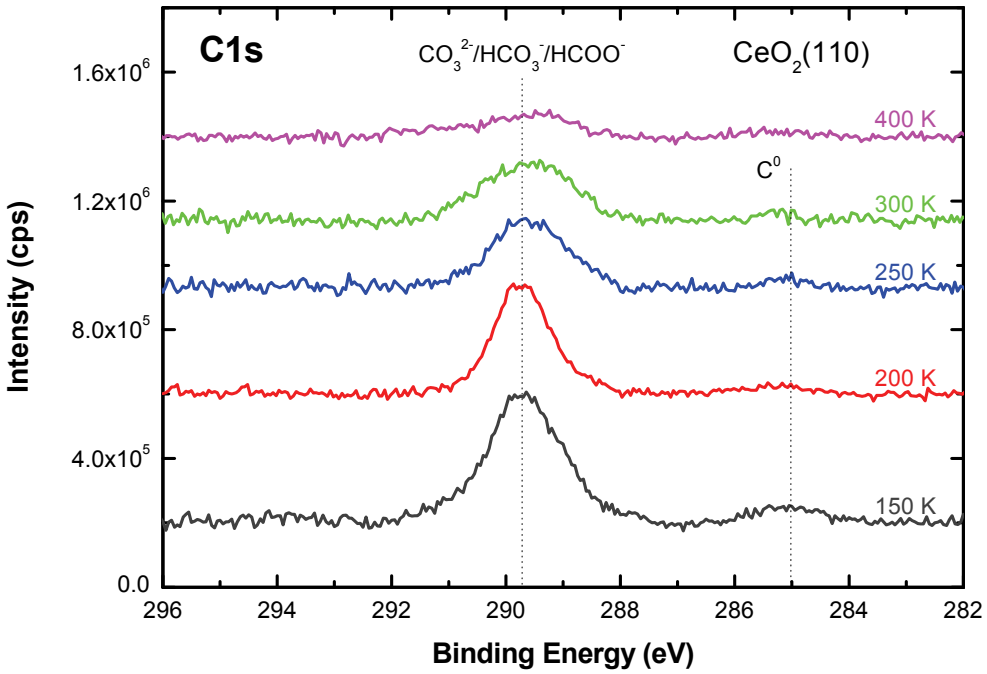

Figure 7.8 C1s core-level XP spectra following a dose of 5 L CO_2 at 120 K and annealed as indicated on oxidized CeO_2(110).

Figure 7.9 shows O1s core-level XP spectra for CO_2 adsorption on oxidized CeO_2(110). The most striking contrast with the O 1s spectra for CO_2 on reduced CeO_{2-x}(110) is the magnitude of the adsorbate (carbonate) peak at around 533.0 eV. Although the carbonate O1s peak has also shifted to lower binding energy with respect to the reduced surface, the shift is similar to what was observed in the C1s spectra (Figure 7.2 and 7.8) and again is not indicative of a different species from that on the reduced surface. The intensity of carbonate O peak decreases monotonically over the temperature range from 150 to 400 K, with the peak nearly extinguished by 400 K.

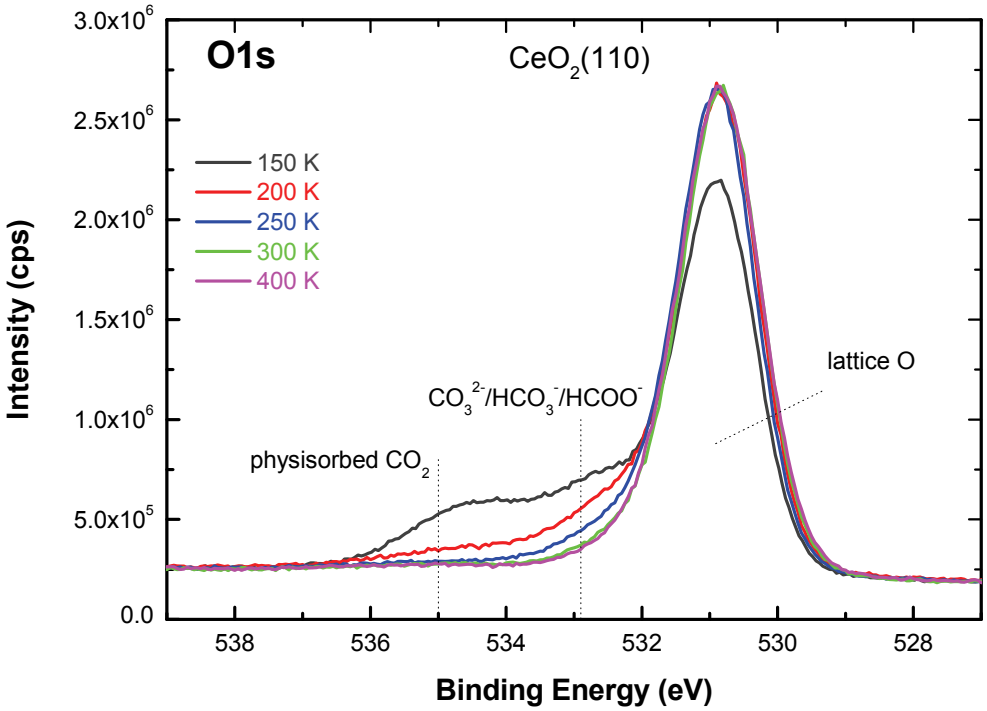

Figure 7.9 O1s core-level XP spectra following a dose of 5 L CO_2 at 120 K and annealed as indicated on oxidized CeO_2(110).

Figure 7.10 shows the C K-edge NEXAFS spectra for the oxidized CeO_2(110) surface exposed to 5 L of CO_2 at 120 K and subsequently annealed to 150, 200 and 300 K. Likewise each spectrum was averaged from 9 spectra acquired at different angles (30, 55, 90°) of incidence, as preferential orientation of adsorbed species on the surface was not observed. In comparison to the C K-edge NEXAFS spectra for CO_2 on reduced CeO_{2-x}(110), the intensities of primary peaks are relatively low, suggesting smaller uptake of CO_2 on the oxidized CeO_2(110) surface. One broad σ*-resonance at around 301.5 eV and another sharper, intense peak corresponding to a π*-resonance at ca. 290.5 eV are evident. The latter can be further resolved into two components at 290.3 and 290.9 eV, respectively. Additionally, a new

minor feature appears at 288.9 eV, which does not exist in the C K-edge NEXAFS spectra of reduced CeO_{2-x}(110). Considering that the oxidized CeO_2(110) sample was prepared ex-situ in the preparation chamber (base pressure 2×10^{-8} mbar) and subsequently transferred into analysis chamber for measurements, during the sample transfer residual water vapor in the chamber might accumulate on the surface and form surface hydroxyl (OH) groups, which probably can react with the later adsorbed CO_2 and induce the newly emerged features in the C K-edge NEXAFS spectra of oxidized CeO_2(110). The possible products are formate ($HCOO^-$) and bicarbonate (HCO_3^-). Thus the new feature at 288.9 eV is assigned to π*-resonance in format ($HCOO^-$) [192, 205], and the new component at 290.9 eV is assigned to π*-resonance in bicarbonate (HCO_3^-) [212].

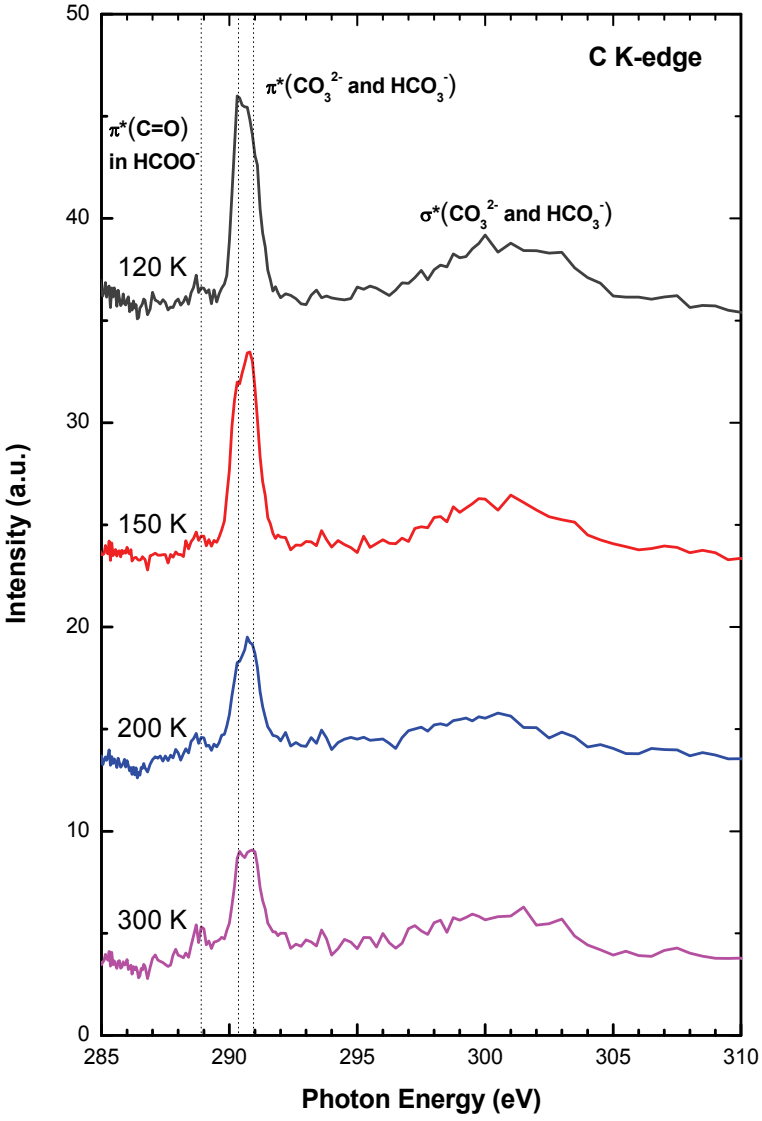

Figure 7.10 Near-edge X-ray absorption fine structure (NEXAFS) spectra at the C K-edge following a dose of 5 L CO_2 at 120 K and annealed as indicated on oxidized CeO_2(110).

To sum up, CO_2 adsorbs on both oxidized and reduced clean ceria (110) surfaces as carbonate and weakly bound CO_2 at low temperatures. No evidence for the formation of a carboxylate ($CO_2^{\delta-}$) intermediate was indicated. The weakly bound CO_2 desorbs by 250 K. Obvious angular dependence of adsorbate was not observed by angle-dependent C K-edge NEXAFS. On reduced CeO_{2-x}(110), carbonate completely desorbs at around 500 K, and furthermore the unchanged reduction extent of the surface indicates that CO_2 does not re-oxidize reduced CeO_{2-x}(110) with breaking of C=O bonds to form CO. On oxidized CeO_2(110) the carbonate is decomposed and desorbed as CO_2 totally at 400 K. The minor formate and bicarbonate species in the spectra probably originate from reactions of CO_2 with surface hydroxyls. The IRRA spectra of CO_2 adsorption on both reduced and oxidized CeO_2(110) contain several peaks with different signs between 1250 and 1650 cm^{-1}, which is documented in Appendix 2.

Conclusions

Since ceria (CeO_2) was first introduced into three-way catalysts (TWCs) 40 years ago, this "magic" material has been widely used as active component, promoter or support in solid phase catalysis. In this thesis, fundamental studies of three C1 molecules (CO, CO_2, and CH_3OH/CD_3OD) adsorption on surfaces of ceria single crystals and/or nanocrystals have been carried out by using ultra-high vacuum Fourier transform infrared spectroscopy (UHV-FTIRS) or near-edge X-ray absorption fine structure (NEXAFS) spectroscopy. The oxidation states of cerium cations on ceria sample surfaces were determined by the core-level and valence band X-ray photoelectron spectroscopy (XPS). LEED was used to assure the well-defined surface crystallinity of the substrate as judged from sharp spots in the patterns.

IRRAS data of carbon monoxide (CO) adsorption on all three low-index surfaces of CeO_2 single crystals demonstrates the capability of CO as an IR-probe to investigate surface oxygen vacancies and distinguish surface orientations. On fully oxidized (111) surface, one intense and Gaussian-like peak at 2154 cm^{-1} is observed, while the CO band blueshifts to 2163 cm^{-1} on reduced surface. The same measurements have also been performed on CeO_2(110) single crystal surface which has higher surface energy than (111) surface. Interestingly, CO adsorption on fully oxidized CeO_2(110) surface exhibits a band at 2170 cm^{-1}, which is 16 cm^{-1} higher than the counterpart of CeO_2(111) surface. Mild annealing CeO_2(110) results in missing of surface oxygen anions in ordered way leading to (2×1) surface reconstruction. Further annealing at higher temperatures in UHV without O_2 induces the increase of defect concentration to form (111) and (11-1) nanofacets at the reduced CeO_{2-x}(110) surface. CeO_2(100) is a polar surface, whose LEED patterns exhibit complex surface reconstructions. The CO adsorption on highly reduced CeO_2(100) surface generates one intense band at 2164 cm^{-1}, while on partial oxidized surface additional two bands at 2182 and 2150 cm^{-1} are observed.

Taking the results of CO adsorption on ceria single crystal surfaces as reference, CO adsorption on ceria nanocrystals (conventional particles, rods, cubes) have been investigated using UHV-FTIR in transmission mode. It is found that ceria nanorods are (110) terminated and expose a great amount of (111) nanofacets. Like ceria nanorods, ceria nanocubes show the primary CO stretching mode of 2170 cm^{-1} at 100 K indicating that ceria nanocubes also contain substantial (110) facets, though ideal ceria nanocubes exclusively expose (100)

surfaces. The proper interpretations with regard to FTIR data of CO adsorption on ceria nanocrystals suggest that ceria nanocrystals are not always as perfectly structured as previous assumptions.

Methanol adsorption on (111) and (110) surfaces of bulk CeO_2 single crystals have been investigated using IRRAS, and our results demonstrate that methanol also can be used as the IR molecular probe. For methanol adsorbed at the fully oxidized (110) surface, IRRA spectra show a single band at 1108 cm^{-1}, which is assigned to a monodentate methoxide species. For the fully oxidized (111) surface, two peaks are observed at 1085 and 1060 cm^{-1} in addition to a weak signal at 1108 cm^{-1}. The latter is assigned to methanol adsorbed at step edges on the ceria surface, which resemble (110) facets. The density functional theory (DFT) simulations suggest that the strong bands at 1085 and 1060 cm^{-1} are assigned to a methanol monolayer that consists of H-bonded methoxide as well as molecularly adsorbed methanol species. *Ab initio* MD simulations for this monolayer yield two strong bands at 1075 and 1055 cm^{-1} that correspond to the symmetrically and asymmetrically coupled CO stretching modes of neighboring methoxide species. For methanol adsorbed at partially reduced ceria (111) surface, no new bands were observed in spite of slight redshift of both bands. The absence of tridentate methoxide bands correlating with oxygen vacancies is probably due to its IR-inactive character. For the reduced ceria (110) surface, a new band around 1070 cm^{-1} was observed, which might be attributed to methoxide species formed on (111) facets at reduced ceria (110) surface.

To date, there have been only NEXAFS studies of CO_2 adsorption on ceria (111) and (100) surfaces. In this thesis, the first NEXAFS results of CO_2 adsorption onto a bulk single crystal CeO_2(110) have been reported. On both reduced and oxidized ceria (110) surface, the adsorbed CO_2 is found to form carbonate species. Upon reduction, excess electrons accumulate on the reduced surface resulting in Ce^{3+} cations. When these electrons are transferred from the substrate to the subsequent adsorbed CO_2 molecules to form carbonate anions, the reduced surface could thus be re-oxidized to some extent. Annealing the CO_2 pre-covered ceria (110) surface does not induce the breaking of C=O bonds and thereby CO formation but CO_2 desorption since the activation energy of CO_2 dissociation is higher than that of CO_2 desorption. Consequently, the surface is reduced back to the original oxidation state.

Abbreviation list

UHV	ultra-high vacuum
SFG	sum frequency generation
SPM	scanning probe microscopy
STM	scanning tunneling microscopy
AFM	atomic force microscopy
XPS	X-ray photoemission spectroscopy
ESCA	electron spectroscopy for chemical analysis
FTIR	Fourier transform infrared spectroscopy
IRRAS	infrared reflection absorption spectroscopy
NEXAFS	near-edge X-ray absorption fine structure
XANES	X-ray absorption near edge structure
LEED	low energy electron diffraction
RHEED	reflection high energy electron diffraction
UPS	ultraviolet photoelectron spectroscopy
TDS	thermal desorption spectroscopy
AES	Auger electron spectroscopy
BET	Brunauer-Emmett-Teller
XRD	X-ray diffraction
HRTEM/HREM	high-resolution transmission electron microscopy
DFT	density functional theory
NIR	near-infrared
MIR	mid-infrared
FIR	far-infrared
MCP	microchannel plate
MCT	mercury cadmium telluride
DTGS	deuterated triglycine sulfate
InSb	indium stibnite
PEY	partial electron yield
TEY	total electron yield
AEY	Auger electron yield
FY	fluorescence yield
TWCs	three-way catalysts

KE	kinetic energy
BE	binding energy
CV	coordination vacancy
PBE	Perdew-Burke-Ernzerhof
BESSY	Berlin Electron Storage Ring Society for Synchrotron Radiation
EB	electron bombardment
V_O	oxygen vacancy
HESGM	high energy spherical grating monochromator
DRIFTS	diffuse reflectance infrared Fourier transform spectroscopy

Appendix 1 Characterizations of ceria single crystals

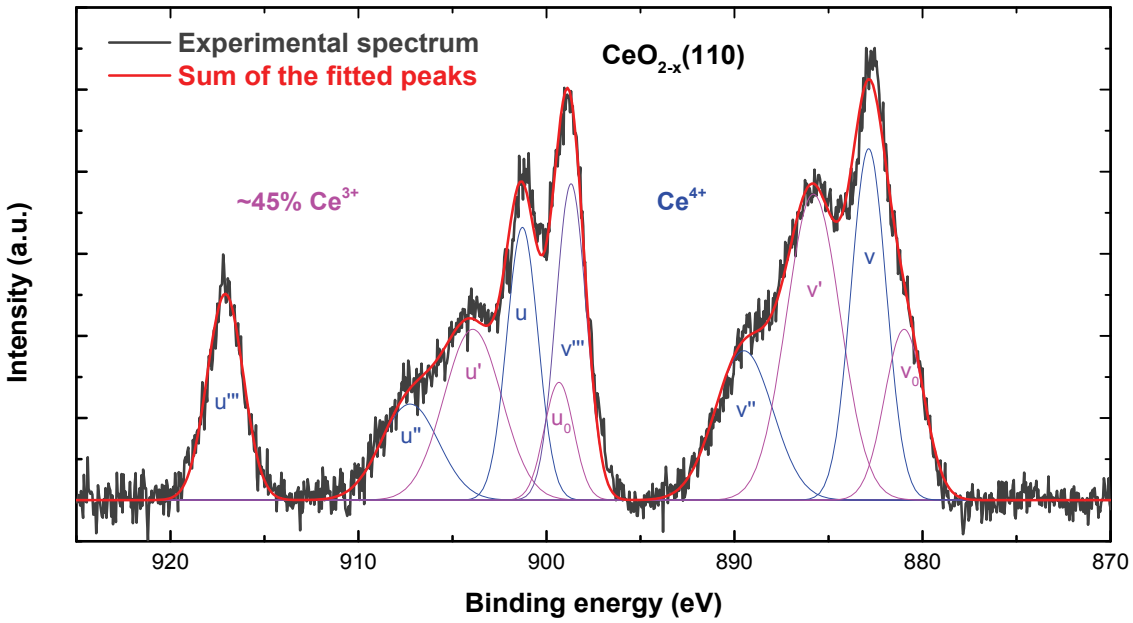

Figure A1.1 Fitted Ce3d XP spectrum of the reduced CeO_{2-x}(110) with (2×1) surface reconstruction.

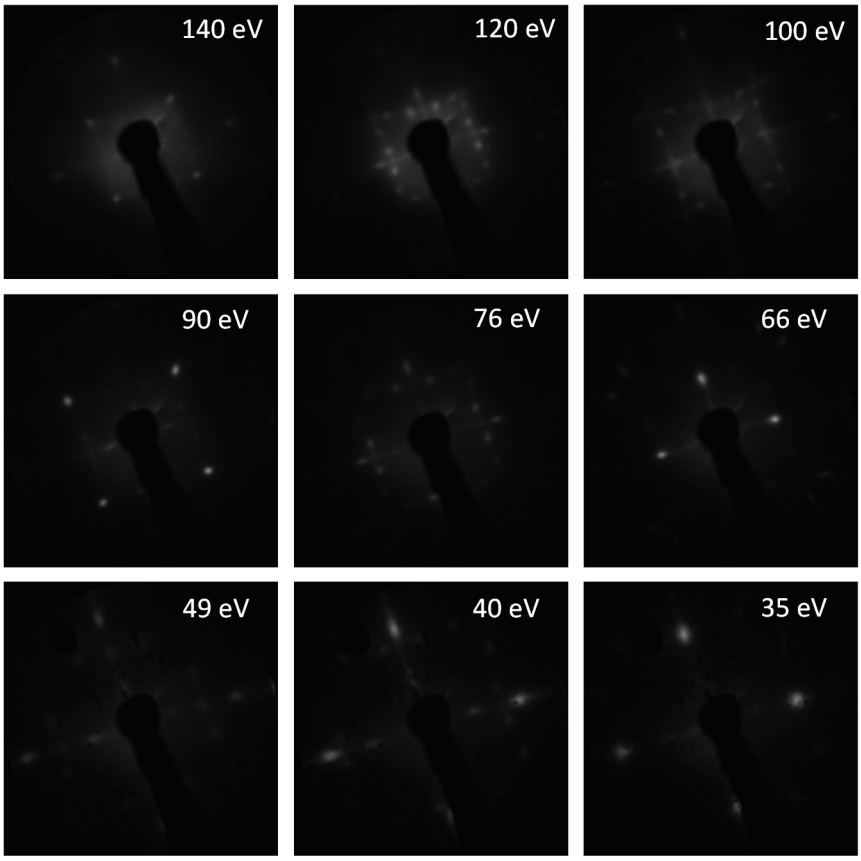

Figure A1.2 LEED patterns of reduced CeO_{2-x}(100).

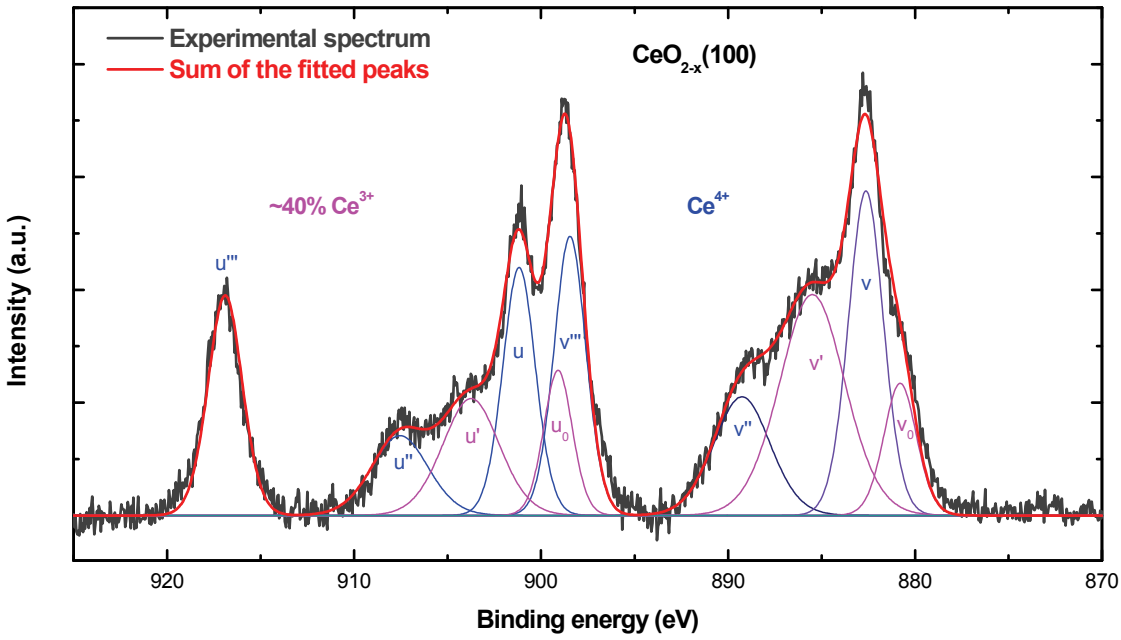

Figure A1.3 Fitted Ce3d XP spectrum of reduced CeO_{2-x}(100).

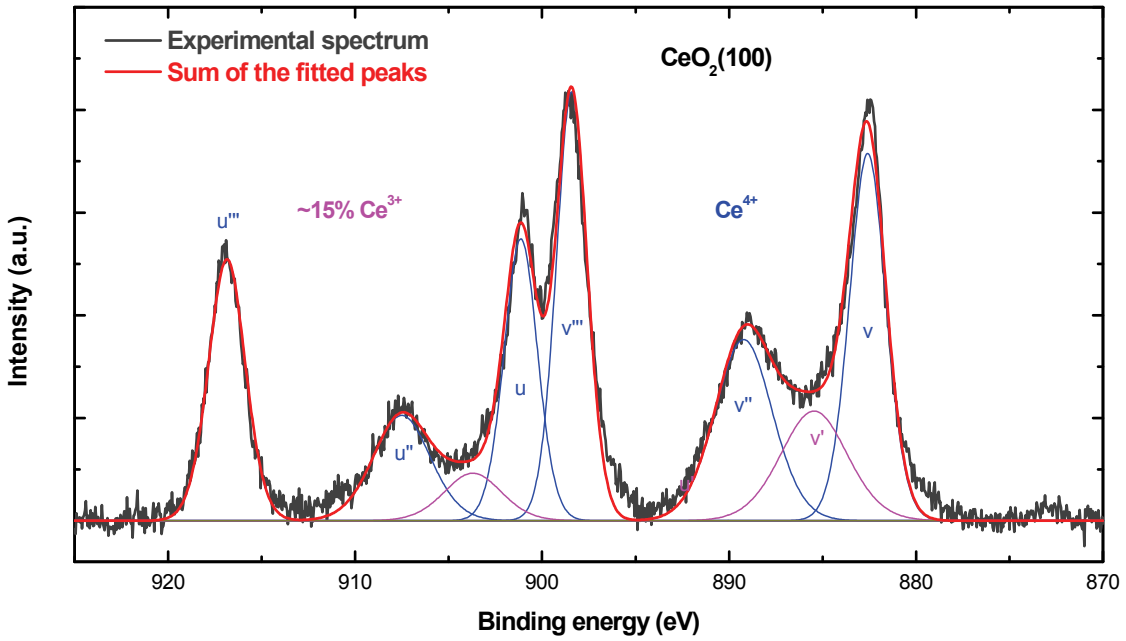

Figure A1.4 Fitted Ce3d XP spectrum of partially oxidized CeO_2(100).

Appendix 2 IRRAS data of CO_2 adsorption on CeO_2(110)

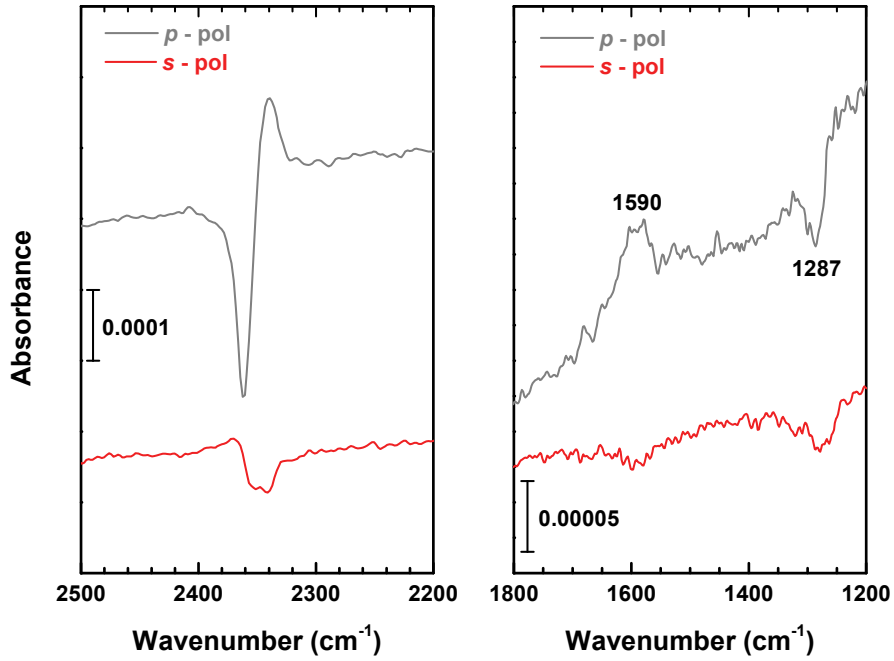

Figure A2.1 Experimental IRRA spectra of 5 L CO_2 at 120 K on reduced CeO_2(110) at a grazing incidence angle of 80° with p- and s-polarized light incident along [1-10].

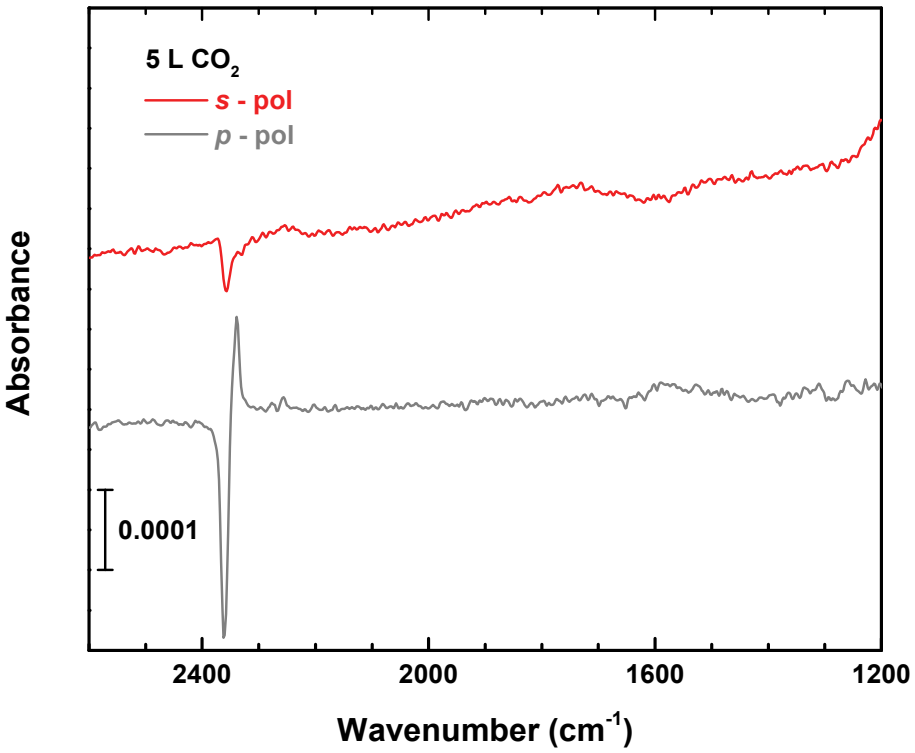

Figure A2.2 Experimental IRRA spectra of 5 L CO_2 at 120 K on reduced CeO_2(110) at a grazing incidence angle of 80° with p- and s-polarized light incident along [001].

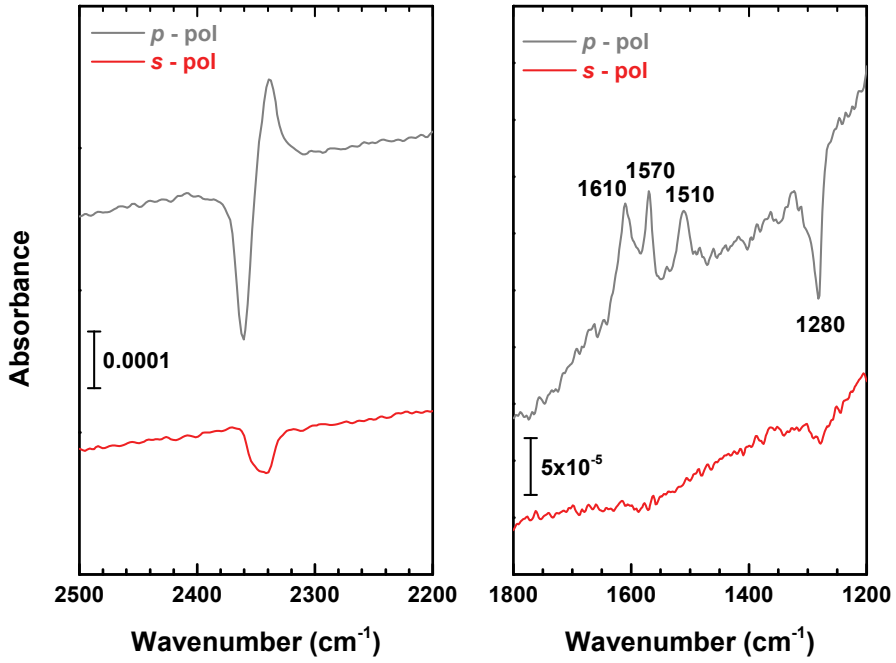

Figure A2.3 Experimental IRRA spectra of 5 L CO_2 at 120 K on oxidized CeO_2(110) at a grazing incidence angle of 80° with p- and s-polarized light incident along [1-10].

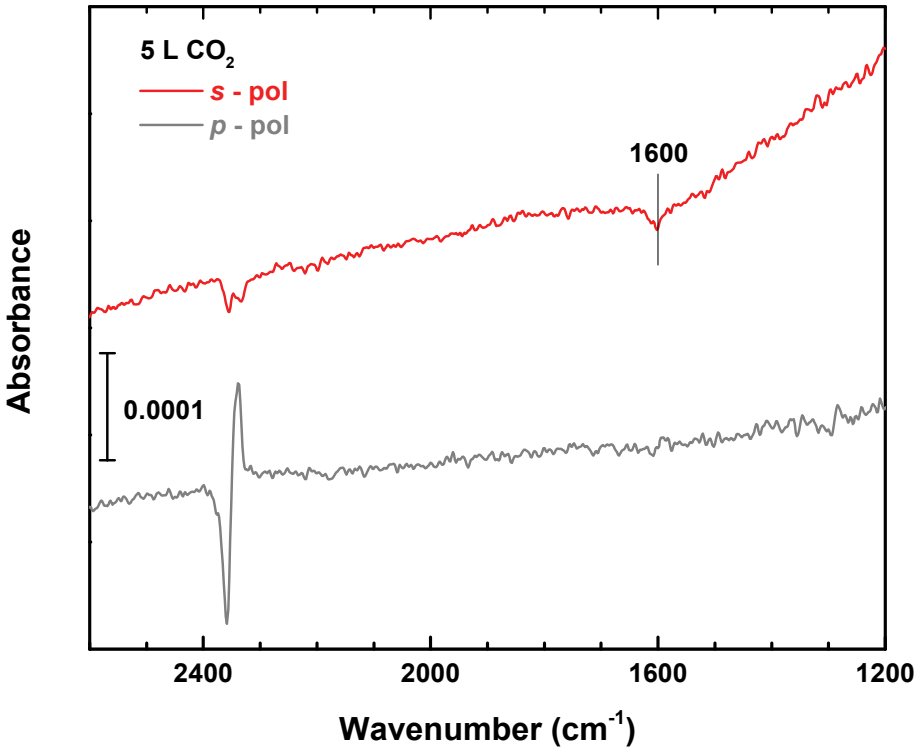

Figure A2.4 Experimental IRRA spectra of 5 L CO_2 at 120 K on reduced CeO_2(110) at a grazing incidence angle of 80° with p- and s-polarized light incident along [001].

Bibliography

[1] J.J. Berzelius, Jber. Chem. 15 (1835) 237.

[2] G. Ertl, T. Gloyna, Katalyse: Vom Stein der Weisen zu Wilhelm Ostwald, Zeitschrift für Physikalische Chemie 217 (2003) 1207–1220.

[3] W. Ostwald, Physikalische Zeitschrioft 3 (1902) 313.

[4] W. Ostwald, Annalen der Naturphilosophie 9 (1910) 1.

[5] National Research Council, Catalysis Looks to the Future, National Academy Press, Washington, D.C., 1992.

[6] I. Langmuir, Chemical reactions on surfaces, Trans. Faraday Soc. 17 (1922) 607–620.

[7] G. Ertl, H.-J. Freund, Catalysis and surface science, Phys. Today 52 (1999) 32–38.

[8] G. Ertl, J. Küppers, Low Energy Electrons and Surface Chemistry, VCH, 1985.

[9] D.P. Woodruff, T.A. Delchar, Modern Techniques of Surface Science, Cambridge University Press, 1994.

[10] J.C. Vickerman, I.S. Gilmore, Surface Analysis: The Principal Techniques, Wiley, 2009.

[11] K.K. Kolasinski, K.W. Kolasinski, Surface Science: Foundations of Catalysis and Nanoscience, Wiley, 2012.

[12] G.A. Somorjai, J.Y. Park, Molecular factors of catalytic selectivity, Angew. Chem. Int. Ed. 47 (2008) 9212–9228.

[13] H.J. Freund, M. Bäumer, J. Libuda, T. Risse, G. Rupprechter, S. Shaikhutdinov, Preparation and characterization of model catalysts: from ultrahigh vacuum to in situ conditions at the atomic dimension, J. Catal. 216 (2003) 223–235.

[14] M.S. Chen, D.W. Goodman, The structure of catalytically active gold on titania, Science 306 (2004) 252–255.

[15] V. Henrich, P. Cox, The Surface Science of Metal Oxides, Cambridge University Press, 1994.

[16] H. Kuhlenbeck, S. Shaikhutdinov, H.-J. Freund, Well-ordered transition metal oxide layers in model catalysis – A series of case studies, Chem. Rev. 113 (2013) 3986–4034.

[17] N. Nilius, Properties of oxide thin films and their adsorption behavior studied by scanning tunneling microscopy and conductance spectroscopy, Surf. Sci. Rep. 64 (2009) 595–659.

[18] V. Johánek, M. Laurin, A.W. Grant, B. Kasemo, C.R. Henry, J. Libuda, Fluctuations

and bistabilities on catalyst nanoparticles, Science 304 (2004) 1639–1644.

[19] F. Traeger, Helium atom scattering from oxide surfaces, ChemPhysChem 7 (2006) 1006–1013.

[20] G.H. Enevoldsen, A.S. Foster, M.C. Christensen, J.V. Lauritsen, F. Besenbacher, Noncontact atomic force microscopy studies of vacancies and hydroxyls of TiO_2(110): Experiments and atomistic simulations, Phys. Rev. B 76 (2007) 205415.

[21] J.V. Lauritsen, M. Reichling, Atomic resolution non-contact atomic force microscopy of clean metal oxide surfaces, J. Phys.: Condens. Matter 22 (2010) 263001.

[22] L. Eyring, The binary rare earth oxides, in Handbook on the Physics and Chemistry of Rare Earths, Elsevier, 1979.

[23] L. Gerward, J. Staun Olsen, L. Petit, G. Vaitheeswaran, V. Kanchana, A. Svane, Bulk modulus of CeO_2 and PrO_2 – An experimental and theoretical study, J. Alloys Compd. 400 (2005) 56–61.

[24] D.D. Koelling, A.M. Boring, J.H. Wood, The electronic structure of CeO_2 and PrO_2, Solid State Commun. 47 (1983) 227–232.

[25] E. Wuilloud, B. Delley, W.D. Schneider, Y. Baer, Spectroscopic evidence for localized and extended *f*-symmetry states in CeO_2, Phys. Rev. Lett. 53 (1984) 202–205.

[26] E. Wuilloud, B. Delley, W.D. Schneider, Y. Baer, Spectroscopic study of localized and extended f-symmetry states in CeO_2, CeN and $CeSi_2$, J. Magn. Magn. Mater. 47 (1985) 197–199.

[27] A. Pfau, K.D. Schierbaum, The electronic structure of stoichiometric and reduced CeO_2 surfaces: An XPS, UPS and HREELS study, Surf. Sci. 321 (1994) 71–80.

[28] J.L.F. Da Silva, M.V. Ganduglia-Pirovano, J. Sauer, V. Bayer, G. Kresse, Hybrid functionals applied to rare-earth oxides: The example of ceria, Phys. Rev. B 75 (2007) 045121.

[29] C.W.M. Castleton, J. Kullgren, K. Hermansson, Tuning LDA+U for electron localization and structure at oxygen vacancies in ceria, J. Chem. Phys. 127 (2007) 244704.

[30] D.R. Mullins, S.H. Overbury, D.R. Huntley, Electron spectroscopy of single crystal and polycrystalline cerium oxide surfaces, Surf. Sci. 409 (1998) 307–319.

[31] J. Paier, C. Penschke, J. Sauer, Oxygen defects and surface chemistry of ceria: Quantum chemical studies compared to experiment, Chem. Rev. 113 (2013) 3949–3985.

[32] H.L. Tuller, A.S. Nowick, Small polaron electron transport in reduced CeO_2 single

crystals, J. Phys. Chem. Solids 38 (1977) 859–867.

[33] H. Nörenberg, G.A.D. Briggs, Defect Structure of nonstoichiometric CeO_2(111) surfaces studied by scanning tunneling microscopy, Phys. Rev. Lett. 79 (1997) 4222–4225.

[34] M.A. Henderson, C.L. Perkins, M.H. Engelhard, S. Thevuthasan, C.H.F. Peden, Redox properties of water on the oxidized and reduced surfaces of CeO_2(111), Surf. Sci. 526 (2003) 1–18.

[35] M.A. Panhans, R.N. Blumenthal, A thermodynamic and electrical conductivity study of nonstoichiometric cerium dioxide, Solid State Ion. 60 (1993) 279–298.

[36] C. Binet, A. Badri, J.-C. Lavalley, A spectroscopic characterization of the reduction of ceria from electronic transitions of intrinsic point defects, J. Phys. Chem. 98 (1994) 6392–6398.

[37] T.X.T. Sayle, S.C. Parker, C.R.A. Catlow, Surface oxygen vacancy formation on CeO_2 and its role in the oxidation of carbon monoxide, J. Chem. Soc., Chem. Commun. (1992) 977–978.

[38] M. Nolan, S.C. Parker, G.W. Watson, The electronic structure of oxygen vacancy defects at the low index surfaces of ceria, Surf. Sci. 595 (2005) 223–232.

[39] D.R. Mullins, P.V. Radulovic, S.H. Overbury, Ordered cerium oxide thin films grown on Ru(0001) and Ni(111), Surf. Sci. 429 (1999) 186–198.

[40] U. Berner, K. Schierbaum, G. Jones, P. Wincott, S. Haq, G. Thornton, Ultrathin ordered CeO_2 overlayers on Pt(111): interaction with NO_2, NO, H_2O and CO, Surf. Sci. 467 (2000) 201–213.

[41] N.V. Skorodumova, S.I. Simak, B.I. Lundqvist, I.A. Abrikosov, B. Johansson, Quantum origin of the oxygen storage capability of ceria, Phys. Rev. Lett. 89 (2002) 166601.

[42] H. Gandhi, A. Piken, M. Shelef, R. Delosh, Laboratory evaluation of three-way catalysts, SAE Tech. Paper (1976) 760201.

[43] A. Trovarelli, Catalytic properties of ceria and CeO_2-containing materials, Catal. Rev. 38 (1996) 439–520.

[44] A. Trovarelli, Catalysis by Ceria and Related Materials, Imperial College Press, 2002.

[45] A. Trovarelli, P. Fornasiero, Catalysis by Ceria and Related Materials 2nd Edition, World Scientific Publishing Company, 2013.

[46] J.J. Delgado, E. del Río, X. Chen, G. Blanco, J.M. Pintado, S. Bernal, J.J. Calvino, A. Trovarelli, P. Fornasiero, Understanding Ceria-Based Catalytic Materials:

An Overview of Recent Progress, in Catalysis by Ceria and Related Materials 2nd Edition, World Scientific Publishing Company, 2013.

[47] L. Vivier, D. Duprez, Ceria-based solid catalysts for organic chemistry, ChemSusChem 3 (2010) 654–678.

[48] D.R. Mullins, The surface chemistry of cerium oxide, Surf. Sci. Rep. 70 (2015) 42–85.

[49] V. Ganduglia-Pirovano, A. Hofmann, J. Sauer, Oxygen vacancies in transition metal and rare earth oxides: Current state of understanding and remaining challenges, Surf. Sci. Rep. 62 (2007) 219–270.

[50] J. Paier, T. Kropp, C. Penschke, J. Sauer, Stability and migration barriers of small vanadium oxide clusters on the CeO_2(111) surface studied by density functional theory, Faraday Discuss. 162 (2013) 233–245.

[51] P.W. Tasker, The stability of ionic crystal surfaces, J. Phys. C: Solid State Phys. 12 (1979) 4977–4984.

[52] J. Conesa, Computer modeling of surfaces and defects on cerium dioxide, Surf. Sci. 339 (1995) 337–352.

[53] M. Baudin, M. Wójcik, K. Hermansson, Dynamics, structure and energetics of the (111), (011) and (001) surfaces of ceria, Surf. Sci. 468 (2000) 51–61.

[54] N.V. Skorodumova, M. Baudin, K. Hermansson, Surface properties of CeO_2 from first principles, Phys. Rev. B 69 (2004) 075401.

[55] Z.X. Yang, T.K. Woo, M. Baudin, K. Hermansson, Atomic and electronic structure of unreduced and reduced CeO_2 surfaces: A first-principles study, J. Chem. Phys. 120 (2004) 7741–7749.

[56] M. Nolan, S. Grigoleit, D.C. Sayle, S.C. Parker, G.W. Watson, Density functional theory studies of the structure and electronic structure of pure and defective low index surfaces of ceria, Surf. Sci. 576 (2005) 217–229.

[57] Y. Jiang, J.B. Adams, M. van Schilfgaarde, Density-functional calculation of CeO_2 surfaces and prediction of effects of oxygen partial pressure and temperature on stabilities, J. Chem. Phys. 123 (2005) 064701.

[58] H.-T. Chen, Y.M. Choi, M. Liu, M.C. Lin, A theoretical study of surface reduction mechanisms of CeO_2(111) and (110) by H_2, ChemPhysChem 8 (2007) 849–855.

[59] M. Nolan, Hybrid density functional theory description of oxygen vacancies in the CeO_2 (110) and (100) surfaces, Chem. Phys. Lett. 499 (2010) 126–130.

[60] T. Desaunay, A. Ringuede, M. Cassir, F. Labat, C. Adamo, Modeling basic components of solid oxide fuel cells using density functional theory: Bulk and surface

properties of CeO_2, Surf. Sci. 606 (2012) 305–311.

[61] H. Nörenberg, G.A.D. Briggs, Surface structure of CeO_2(111) studied by low current STM and electron diffraction, Surf. Sci. 402–404 (1998) 734–737.

[62] S. Eck, C. Castellarin-Cudia, S. Surnev, M.G. Ramsey, F.P. Netzer, Growth and thermal properties of ultrathin cerium oxide layers on Rh(111), Surf. Sci. 520 (2002) 173–185.

[63] J.L. Lu, H.J. Gao, S. Shaikhutdinov, H.J. Freund, Morphology and defect structure of the CeO_2(111) films grown on Ru(0001) as studied by scanning tunneling microscopy, Surf. Sci. 600 (2006) 5004–5010.

[64] A. Siokou, R.M. Nix, Interaction of methanol with well-defined ceria surfaces: Reflection/absorption infrared spectroscopy, X-ray photoelectron spectroscopy, and temperature-programmed desorption study, J. Phys. Chem. B 103 (1999) 6984–6997.

[65] Y. Namai, K.-i. Fukui, Y. Iwasawa, Atom-resolved noncontact atomic force microscopic observations of CeO_2(111) surfaces with different oxidation states: Surface structure and behavior of surface oxygen atoms, J. Phys. Chem. B 107 (2003) 11666–11673.

[66] Y. Namai, K.I. Fukui, Y. Iwasawa, Atom-resolved noncontact atomic force microscopic and scanning tunneling microscopic observations of the structure and dynamic behavior of CeO_2(111) surfaces, Catal. Today 85 (2003) 79–91.

[67] S. Gritschneder, Y. Namai, Y. Iwasawa, M. Reichling, Structural features of CeO_2(111) revealed by dynamic SFM, Nanotechnol. 16 (2005) S41–S48.

[68] S. Gritschneder, M. Reichling, Structural elements of CeO_2(111) surfaces, Nanotechnol. 18 (2007) 044024.

[69] J. Zhou, A.P. Baddorf, D.R. Mullins, S.H. Overbury, Growth and characterization of Rh and Pd nanoparticles on oxidized and reduced CeO_x(111) thin films by scanning tunneling microscopy, J. Phys. Chem. C 112 (2008) 9336–9345.

[70] F. Esch, S. Fabris, L. Zhou, T. Montini, C. Africh, P. Fornasiero, G. Comelli, R. Rosei, Electron localization determines defect formation on ceria substrates, Science 309 (2005) 752–755.

[71] S. Torbrügge, M. Cranney, M. Reichling, Morphology of step structures on CeO_2(111), Appl. Phys. Lett. 93 (2008) 073112.

[72] H. Nörenberg, G.A.D. Briggs, The surface structure of CeO_2(110) single crystals studied by STM and RHEED, Surf. Sci. 433–435 (1999) 127–130.

[73] C. Muggelberg, M.R. Castell, G.A.D. Briggs, D.T. Goddard, The atomic structure of

the UO_{2+x}(110) surface and the effects of interstitial oxygen: an elevated-temperature STM study, Surf. Sci. 402–404 (1998) 673–677.

[74] T.E. Jackman, J.A. Davies, O.P. Jackson, W.N. Unertl, P.R. Norton, The Pt(110) phase transitions: A study by rutherford backscattering, nuclear microanalysis, LEED and thermal desorption spectroscopy, Surf. Sci. 120 (1982) 389–412.

[75] S.R. Bare, P. Hofmann, D.A. King, Vibrational studies of the surface phases of CO on Pt{110} at 300 K, Surf. Sci. 144 (1984) 347–369.

[76] C. Tian, Y. Du, S.-W. Chan, Preparation and microstructural study of CeO_2 thin films, J. Vac. Sci. Technol. A 15 (1997) 85–92.

[77] Y.J. Kim, Y. Gao, G.S. Herman, S. Thevuthasan, W. Jiang, D.E. McCready, S.A. Chambers, Growth and structure of epitaxial CeO_2 by oxygen-plasma-assisted molecular beam epitaxy, J. Vac. Sci. Technol. A 17 (1999) 926–935.

[78] S.H. Overbury, D.R. Huntley, D.R. Mullins, K.S. Ailey, P.V. Radulovic, Surface studies of model supported catalysts: NO adsorption on Rh/CeO_2(001), J. Vac. Sci. Technol. A 15 (1997) 1647–1652.

[79] G.S. Herman, Surface structure determination of CeO_2(001) by angle-resolved mass spectroscopy of recoiled ions, Phys. Rev. B, 59 (1999) 14899–14902.

[80] F. Yang, Y. Choi, S. Agnoli, P. Liu, D. Stacchiola, J. Hrbek, J.A. Rodriguez, $CeO_2 \leftrightarrow CuO_x$ interactions and the controlled assembly of CeO_2(111) and CeO_2(100) nanoparticles on an oxidized Cu(111) substrate, J. Phys. Chem. C 115 (2011) 23062–23066.

[81] H. Nörenberg, J.H. Harding, The surface structure of CeO_2(001) single crystals studied by elevated temperature STM, Surf. Sci. 477 (2001) 17–24.

[82] Y. Lin, Z. Wu, J. Wen, K.R. Poeppelmeier, L.D. Marks, Imaging the atomic surface structures of CeO_2 nanoparticles, Nano Lett., 14 (2014) 191–196.

[83] J.M. Chalmers, P.R. Griffiths, Handbook of vibrational spectroscopy, Wiley, 2002.

[84] B.H. Stuart, Infrared Spectroscopy: Fundamentals and Applications, Wiley, 2004.

[85] P.R. Griffiths, Introduction to Vibrational Spectroscopy, in Handbook of Vibrational Spectroscopy, Wiley, 2006.

[86] http://orgchem.colorado.edu/Spectroscopy/irtutor/IRtheory.pdf, 05.05.2016.

[87] S.A. Francis, A. Ellison, Infrared spectra of monolayers on metal mirrors, J. Opt. Soc. Am. A 49 (1959) 131–137.

[88] R.G. Greenler, Infrared study of adsorbed molecules on metal surfaces by reflection techniques, J. Chem. Phys. 44 (1966) 310–315.

[89] R.G. Greenler, Design of a reflection-absorption experiment for studying the ir spectrum of molecules adsorbed on a metal surface, J. Vac. Sci. Technol. 12 (1975) 1410–1417.

[90] R.G. Greenler, D. Snider, D. Witt, R. Sorbello, The metal-surface selection rule for infrared spectra of molecules adsorbed on small metal particles, Surf. Sci. 118 (1982) 415–428.

[91] M.E. Pemble, P. Gardner, Vibrational Spectroscopy from Surfaces, in Surface Analysis – The Principal Techniques, Wiley, 2009.

[92] J. Kattner, H. Hoffmann, External Reflection Spectroscopy of Thin Films on Dielectric Substrates, in Handbook of Vibrational Spectroscopy, Wiley, 2006.

[93] M.A. VanHove, W.H. Weinberg, C.-M. Chan, Low-Energy Electron Diffraction: Experiment, Theory and Surface Structure Determination, Springer Science & Business Media, 2012.

[94] K. Siegbahn, ESCA Applied to Free Molecules, North-Holland Pub. Co., 1970.

[95] K. Siegbahn, Electron spectroscopy for atoms, molecules, and condensed matter, Rev. Mod. Phys. 54 (1982) 709–728 .

[96] M. Buchholz, UHV-FTIRS-Untersuchungen an einkristallinen Oxidoberflaechen, Karlsruher Institut für Technologie, 2014.

[97] A. Nefedov, C. Wöll, Advanced Applications of NEXAFS Spectroscopy for Functionalized Surfaces, in Surface Science Techniques, Springer, 2013.

[98] J. Stöhr, NEXAFS Spectroscopy, Springer, 1992.

[99] G. Hahner, Near edge X-ray absorption fine structure spectroscopy as a tool to probe electronic and structural properties of thin organic films and liquids, Chem. Soc. Rev. 35 (2006) 1244–1255.

[100] J. Stöhr, D.A. Outka, Determination of molecular orientations on surfaces from the angular dependence of near-edge x-ray-absorption fine-structure spectra, Phys. Rev. B 36 (1987) 7891–7905.

[101] H. Winick, S. Doniach, Synchrotron Radiation Research, Springer Science & Business Media, 2012.

[102] Y. Wang, A. Glenz, M. Muhler, C. Wöll, A new dual-purpose ultrahigh vacuum infrared spectroscopy apparatus optimized for grazing-incidence reflection as well as for transmission geometries, Rev. Sci. Instrum. 80 (2009) 113108.

[103] H. Idriss, M. Scott, J. Llorca, S.C. Chan, W. Chiu, P.-Y. Sheng, A. Yee, M.A. Blackford, S.J. Pas, A.J. Hill, F.M. Alamgir, R. Rettew, C. Petersburg, S.D.

Senanayake, M.A. Barteau, A phenomenological study of the metal-oxide interface: The role of catalysis in hydrogen production from renewable resources, ChemSusChem 1 (2008) 905–910.

[104] X. Wang, J.A. Rodriguez, J.C. Hanson, D. Gamarra, A. Martínez-Arias, M. Fernández-García, In situ studies of the active sites for the water gas shift reaction over Cu−CeO_2 catalysts: Complex interaction between betallic copper and oxygen vacancies of ceria, J. Phys. Chem. B 110 (2006) 428–434.

[105] W. Xu, R. Si, S.D. Senanayake, J. Llorca, H. Idriss, D. Stacchiola, J.C. Hanson, J.A. Rodriguez, In situ studies of CeO_2-supported Pt, Ru, and Pt–Ru alloy catalysts for the water-gas shift reaction: Active phases and reaction intermediates, J. Catal. 291 (2012) 117–126.

[106] J.A. Rodriguez, P. Liu, J. Hrbek, J. Evans, M. Pérez, Water gas shift reaction on Cu and Au nanoparticles supported on CeO_2(111) and ZnO(000-1): Intrinsic activity and importance of support interactions, Angew. Chem. Int. Ed. 46 (2007) 1329–1332.

[107] I. Al-Shankiti, F. Al-Otaibi, Y. Al-Salik, H. Idriss, Solar thermal hydrogen production from water over modified CeO_2 materials, Top. Catal. 56 (2013) 1129–1138.

[108] W.C. Chueh, C. Falter, M. Abbott, D. Scipio, P. Furler, S.M. Haile, A. Steinfeld, High-flux solar-driven thermochemical dissociation of CO_2 and H_2O using nonstoichiometric ceria, Science 330 (2010) 1797–1801.

[109] P. Furler, J.R. Scheffe, A. Steinfeld, Syngas production by simultaneous splitting of H_2O and CO_2 via ceria redox reactions in a high-temperature solar reactor, Energ. Environ. Sci. 5 (2012) 6098–6103.

[110] M.V. Ganduglia-Pirovano, J.L.F. Da Silva, J. Sauer, Density-functional calculations of the structure of near-surface oxygen vacancies and electron localization on CeO_2(111), Phys. Rev. Lett. 102 (2009) 026101.

[111] H.-Y. Li, H.-F. Wang, X.-Q. Gong, Y.-L. Guo, Y. Guo, G. Lu, P. Hu, Multiple configurations of the two excess 4f electrons on defective CeO_2(111): Origin and implications, Phys. Rev. B 79 (2009) 193401.

[112] E. Shoko, M.F. Smith, H.M. Ross, Charge distribution near bulk oxygen vacancies in cerium oxides, J. Phys.: Condens. Matter 22 (2010) 223201.

[113] J.F. Jerratsch, X. Shao, N. Nilius, H.-J. Freund, C. Popa, M.V. Ganduglia-Pirovano, A.M. Burow, J. Sauer, Electron localization in defective ceria films: An STM and DFT study, Phys. Rev. Lett. 106 (2011) 246801.

[114] Y.-G. Wang, D. Mei, J. Li, R. Rousseau, DFT+U study on the localized electronic

states and their potential role during H_2O dissociation and CO oxidation processes on CeO_2(111) surface, J. Phys. Chem. C 117 (2013) 23082–23089.

[115] J.J. Plata, A.M. Márquez, J.F. Sanz, Transport properties in the CeO_{2-x}(111) surface: From charge distribution to ion-electron collaborative migration, J. Phys. Chem. C 117 (2013) 25497–25503.

[116] R. Farra, S. Wrabetz, M.E. Schuster, E. Stotz, N.G. Hamilton, A.P. Amrute, J. Perez-Ramirez, N. Lopez, D. Teschner, Understanding CeO_2 as a Deacon catalyst by probe molecule adsorption and in situ infrared characterisations, Phys. Chem. Chem. Phys. 15 (2013) 3454–3465.

[117] P. Bazin, O. Saur, J.C. Lavalley, M. Daturi, G. Blanchard, FT-IR study of CO adsorption on Pt/CeO_2: characterisation and structural rearrangement of small Pt particles, Phys. Chem. Chem. Phys. 7 (2005) 187–194.

[118] T. Tabakova, F. Boccuzzi, M. Manzoli, D. Andreeva, FTIR study of low-temperature water-gas shift reaction on gold/ceria catalyst, Appl. Catal. A 252 (2003) 385–397.

[119] M. Daturi, C. Binet, J.-C. Lavalley, A. Galtayries, R. Sporken, Surface investigation on $Ce_xZr_{1-x}O_2$ compounds, Phys. Chem. Chem. Phys. 1 (1999) 5717–5724.

[120] G.A. Mekhemer, M.I. Zaki, Low-temperature IR spectroscopy of CO adsorption on calcined supported CeO_2: Probing adsorbed species and adsorbing sites, Adsorpt. Sci. Technol. 15 (1997) 377–389.

[121] C. Binet, M. Daturi, J.-C. Lavalley, IR study of polycrystalline ceria properties in oxidised and reduced states, Catal. Today 50 (1999) 207–225.

[122] A. Badri, C. Binet, J.-C. Lavalley, Metal-support interaction in Pd/CeO_2 catalysts. Part 2. −Ceria textural effects, J. Chem. Soc., Faraday Trans. 92 (1996) 1603–1608.

[123] M.I. Zaki, B. Vielhaber, H. Knoezinger, Low-temperature carbon monoxide adsorption and state of molybdena supported on alumina, titania, ceria, and zirconia. An infrared spectroscopic investigation, J. Phys. Chem. 90 (1986) 3176–3183.

[124] F. Bozon-Verduraz, A. Bensalem, IR studies of cerium dioxide: influence of impurities and defects, J. Chem. Soc., Faraday Trans. 90 (1994) 653–657.

[125] C. Li, Y. Sakata, T. Arai, K. Domen, K.-i. Maruya, T. Onishi, Carbon monoxide and carbon dioxide adsorption on cerium oxide studied by Fourier-transform infrared spectroscopy. Part 1. −Formation of carbonate species on dehydroxylated CeO_2, at room temperature, Journal of the Chemical Society, J. Chem. Soc., Faraday Trans. 1 85 (1989) 929–943.

[126] P. St. Petkov, G.N. Vayssilov, J. Liu, O. Shekhah, Y. Wang, C. Wöll, T. Heine, Defects

in MOFs: A thorough characterization, ChemPhysChem 13 (2012) 2025−2029.

[127] K. Mudiyanselage, H.Y. Kim, S.D. Senanayake, A.E. Baber, P. Liu, D. Stacchiola, Probing adsorption sites for CO on ceria, Phys. Chem. Chem. Phys. 15 (2013) 15856−15862.

[128] M. Xu, H. Noei, K. Fink, M. Muhler, Y. Wang, C. Wöll, The surface science approach for understanding reactions on oxide powders: The importance of IR spectroscopy, Angew. Chem. Int. Ed. 51 (2012) 4731−4734.

[129] M. Xu, Y. Gao, E.M. Moreno, M. Kunst, M. Muhler, Y. Wang, H. Idriss, C. Wöll, Photocatalytic activity of bulk TiO_2 anatase and rutile single crystals using infrared absorption spectroscopy, Phys. Rev. Lett. 106 (2011) 138302.

[130] P. Burroughs, A. Hamnett, A.F. Orchard, G. Thornton, Satellite structure in the X-ray photoelectron spectra of some binary and mixed oxides of lanthanum and cerium, J. Chem. Soc., Dalton Trans. (1976) 1686−1698.

[131] A. Kotani, T. Jo, J.C. Parlebas, Many-body effects in core-level spectroscopy of rare-earth compounds, Adv. Phys. 37 (1988) 37−85.

[132] E.J. Preisler, O.J. Marsh, R.A. Beach, T.C. McGill, Stability of cerium oxide on silicon studied by x-ray photoelectron spectroscopy, J. Vac. Sci. Technol. B 19 (2001) 1611−1618.

[133] I. Celardo, M. De Nicola, C. Mandoli, J.Z. Pedersen, E. Traversa, L. Ghibelli, Ce^{3+} ions determine redox-dependent anti-apoptotic effect of cerium oxide nanoparticles, ACS Nano 5 (2011) 4537−4549.

[134] P.A. Redhead, Thermal desorption of gases, Vacuum 12 (1962) 203−211.

[135] C. Yang, L.-L. Yin, F. Bebensee, M. Buchholz, H. Sezen, S. Heissler, J. Chen, A. Nefedov, H. Idriss, X.-Q. Gong, C. Wöll, Chemical activity of oxygen vacancies on ceria: a combined experimental and theoretical study on CeO_2(111), Phys. Chem. Chem. Phys. 16 (2014) 24165−24168.

[136] C. Rohmann, J.B. Metson, H. Idriss, DFT study of carbon monoxide adsorption on α-Al_2O_3(0001), Surf. Sci. 605 (2011) 1694−1703.

[137] C. Rohmann, J.B. Metson, H. Idriss, A DFT study on carbon monoxide adsorption onto hydroxylated α-Al_2O_3(0001) surfaces, Phys. Chem. Chem. Phys. 16 (2014) 14287−14297.

[138] G. Ertl, Reactions at surfaces: from atoms to complexity (Nobel lecture), Angew. Chem. Int. Ed. 47 (2008) 3524−3535.

[139] G. Vurens, M. Salmeron, G. Somorjai, The preparation of thin ordered transition metal

oxide films on metal single crystals for surface science studies, Prog. Surf. Sci. 32 (1989) 333−360.

[140] H.-J. Freund, Metal-supported ultrathin oxide film systems as designable catalysts and catalyst supports, Surf. Sci. 601 (2007) 1438−1442.

[141] H.-J. Freund, G. Pacchioni, Oxide ultra-thin films on metals: new materials for the design of supported metal catalysts, Chem. Soc. Rev. 37 (2008) 2224−2242.

[142] G. Pacchioni, H.-J. Freund, Electron transfer at oxide surfaces. The MgO paradigm: from defects to ultrathin films, Chem. Rev. 113 (2013) 4035−4072.

[143] G. Pacchioni, Two-dimensional oxides and their role in electron transfer mechanisms with adsorbed species, Chem. Rec. 14 (2014) 910−922.

[144] C.T. Campbell, Ultrathin metal films and particles on oxide surfaces: structural, electronic and chemisorptive properties, Surf. Sci. Rep. 27 (1997) 1−111.

[145] R.I. Masel, Principles of Adsorption and Reaction on Solid Surfaces, Wiley, 1996.

[146] G. Somorjai, Introduction to Surface Chemistry and Catalysis, Wiley, 1994.

[147] K. Christmann, Introduction to Surface Physical Chemistry, Springer, 1991.

[148] W. Weiss, W. Ranke, Surface chemistry and catalysis on well-defined epitaxial iron-oxide layers, Prog. Surf. Sci. 70 (2002) 1−151.

[149] W. Ranke, Y. Joseph, Determination of adsorption energies and kinetic parameters by isosteric methods, Phys. Chem. Chem. Phys. 4 (2002) 2483−2498.

[150] H. Wilkens, O. Schuckmann, R. Oelke, S. Gevers, M. Reichling, A. Schaefer, M. Baumer, M.H. Zoellner, G. Niu, T. Schroeder, J. Wollschlager, Structural transitions of epitaxial ceria films on Si(111), Phys. Chem. Chem. Phys. 15 (2013) 18589−18599.

[151] O. Gamba, H. Noei, J. Pavelec, R. Bliem, M. Schmid, U. Diebold, A. Stierle, G.S. Parkinson, Adsorption of formic acid on the Fe_3O_4(001) surface, J. Phys. Chem. C 119 (2015) 20459−20465.

[152] K. Zhou, Y. Li, Catalysis based on nanocrystals with well-defined facets, Angew. Chem. Int. Ed. 51 (2012) 602−613.

[153] D. Zhang, X. Du, L. Shi, R. Gao, Shape-controlled synthesis and catalytic application of ceria nanomaterials, Dalton Trans. 41 (2012) 14455−14475.

[154] H.-X. Mai, L.-D. Sun, Y.-W. Zhang, R. Si, W. Feng, H.-P. Zhang, H.-C. Liu, C.-H. Yan, Shape-selective synthesis and oxygen storage behavior of ceria nanopolyhedra, Nanorods, and Nanocubes, J. Phys. Chem. B 109 (2005) 24380−24385.

[155] K. Zhou, X. Wang, X. Sun, Q. Peng, Y. Li, Enhanced catalytic activity of ceria nanorods from well-defined reactive crystal planes, J. Catal. 229 (2005) 206−212.

[156] Z.L. Wang, X. Feng, Polyhedral Shapes of CeO_2 Nanoparticles, J. Phys. Chem. B 107 (2003) 13563−13566.

[157] Y. Zhiqiang, Z. Kebin, L. Xiangwen, T. Qun, L. Deyi, Y. Sen, Single-crystalline ceria nanocubes: size-controlled synthesis, characterization and redox property, Nanotechnol. 18 (2007) 185606.

[158] Tana, M. Zhang, J. Li, H. Li, Y. Li, W. Shen, Morphology-dependent redox and catalytic properties of CeO_2 nanostructures: Nanowires, nanorods and nanoparticles, Catal. Today 148 (2009) 179−183.

[159] S. Agarwal, L. Lefferts, B.L. Mojet, D.A.J.M. Ligthart, E.J.M. Hensen, D.R.G. Mitchell, W.J. Erasmus, B.G. Anderson, E.J. Olivier, J.H. Neethling, A.K. Datye, Exposed surfaces on shape-controlled ceria nanoparticles revealed through AC-TEM and water-gas shift reactivity, ChemSusChem 6 (2013) 1898−1906.

[160] T. Inoue, Y. Yamamoto, M. Satoh, A. Ide, S. Katsumata, Surface structure of single-crystal CeO_2 layers grown on Si, Thin Solid Films 281–282 (1996) 24−27.

[161] P.A. Crozier, R. Wang, R. Sharma, In situ environmental TEM studies of dynamic changes in cerium-based oxides nanoparticles during redox processes, Ultramicrosc. 108 (2008) 1432−1440.

[162] D.R. Mullins, P.M. Albrecht, T.-L. Chen, F.C. Calaza, M.D. Biegalski, H.M. Christen, S.H. Overbury, Water dissociation on CeO_2(100) and CeO_2(111) thin films, J. Phys. Chem. C 116 (2012) 19419−19428.

[163] A.K.P. Mann, Z. Wu, S.H. Overbury, The Characterization and Structure-Dependent Catalysis of Ceria with Well-Defined Facets, in Catalysis by Materials with Well-Defined Structures, Elsevier, 2015.

[164] Z. Wu, M. Li, D.R. Mullins, S.H. Overbury, Probing the surface sites of CeO_2 nanocrystals with well-defined surface planes via methanol adsorption and desorption, ACS Catal. 2 (2012) 2224−2234.

[165] J.M. Tatibouët, Methanol oxidation as a catalytic surface probe, Appl. Catal. A 148 (1997) 213−252.

[166] M. Badlani, I.E. Wachs, Methanol: a "smart" chemical probe molecule, Catal. Lett. 75 (2001) 137−149.

[167] A. Beste, D.R. Mullins, S.H. Overbury, R.J. Harrison, Adsorption and dissociation of methanol on the fully oxidized and partially reduced (111) cerium oxide surface: Dependence on the configuration of the cerium 4*f* electrons, Surf. Sci. 602 (2008) 162−175.

[168] T. Kropp, J. Paier, Reactions of methanol with pristine and defective ceria (111) surfaces: A comparison of density functionals, J. Phys. Chem. C 118 (2014) 23690−23700.

[169] C. Li, K. Domen, K.-i. Maruya, T. Onishi, Spectroscopic identification of adsorbed species derived from adsorption and decomposition of formic acid, methanol, and formaldehyde on cerium oxide, J. Catal. 125 (1990) 445−455.

[170] A. Badri, C. Binet, J.C. Lavalley, Use of methanol as an IR molecular probe to study the surface of polycrystalline ceria, J. Chem. Soc.-Faraday Trans. 93 (1997) 1159−1168.

[171] Y. Namai, K. Fukui, Y. Iwasawa, The dynamic behaviour of CH_3OH and NO_2 adsorbed on CeO_2(111) studied by noncontact atomic force microscopy, Nanotechnol. 15 (2004) S49−S54.

[172] D.R. Mullins, M.D. Robbins, J. Zhou, Adsorption and reaction of methanol on thin-film cerium oxide, Surf. Sci. 600 (2006) 1547−1558.

[173] P.M. Albrecht, D.R. Mullins, Adsorption and reaction of methanol over CeO_X(100) thin films, Langmuir 29 (2013) 4559−4567.

[174] H.L. Abbott, A. Uhl, M. Baron, Y. Lei, R.J. Meyer, D.J. Stacchiola, O. Bondarchuk, S. Shaikhutdinov, H.J. Freund, Relating methanol oxidation to the structure of ceria-supported vanadia monolayer catalysts, J. Catal. 272 (2010) 82−91.

[175] J. Uhlrich, B. Yang, S. Shaikhutdinov, Methanol reactivity on silica-supported ceria nanoparticles, Top. Catal. 57 (2014) 1229–1235.

[176] K. Nakanishi, Infrared Absorption Spectroscopy, Practical, Holden-Day, 1962.

[177] S.M.F. Shahed, Y. Sainoo, T. Komeda, Scanning tunneling microscope study of surface morphology variation of CeO_2(111) with changing annealing condition, JPN J. Appl. Phys. 50 (2011) 08LB05.

[178] N. Nilius, S.M. Kozlov, J.F. Jerratsch, M. Baron, X. Shao, F. Vines, S. Shaikhutdinov, K.M. Neyman, H.J. Freund, Formation of one-dimensional electronic states along the step edges of CeO_2(111), ACS Nano 6 (2012) 1126−1133.

[179] S.M. Kozlov, F. Vines, N. Nilius, S. Shaikhutdinov, K.M. Neyman, Absolute surface step energies: Accurate theoretical methods applied to ceria nanoislands, J. Phys. Chem. Lett. 3 (2012) 1956−1961.

[180] C. Yang, F. Bebensee, A. Nefedov, C. Wöll, T. Kropp, L. Komissarov, C. Penschke, R. Moerer, J. Paier, J. Sauer, Methanol adsorption on monocrystalline ceria surfaces, J. Catal. 336 (2016) 116−125.

[181] V. Matolín, J. Libra, M. Skoda, N. Tsud, K.C. Prince, T. Skála, Methanol adsorption on a CeO_2(111)/Cu(111) thin film model catalyst, Surf. Sci. 603 (2009) 1087−1092.

[182] T. Kropp, J. Paier, Activity versus selectivity of the methanol oxidation at ceria surfaces: A comparative first-principles study, J. Phys. Chem. C 119 (2015) 23021−23031.

[183] M. Aresta, Carbon Dioxide as Chemical Feedstock, Wiley, 2010.

[184] U. Burghaus, Surface chemistry of CO_2 – Adsorption of carbon dioxide on clean surfaces at ultrahigh vacuum, Prog. Surf. Sci. 89 (2014) 161–217.

[185] U. Burghaus, Surface science perspective of carbon dioxide chemistry – Adsorption kinetics and dynamics of CO_2 on selected model surfaces, Catal. Today 148 (2009) 212–220.

[186] H.J. Freund, M.W. Roberts, Surface chemistry of carbon dioxide, Surf. Sci. Rep. 25 (1996) 225–273.

[187] J. Graciani, K. Mudiyanselage, F. Xu, A.E. Baber, J. Evans, S.D. Senanayake, D.J. Stacchiola, P. Liu, J. Hrbek, J.F. Sanz, J.A. Rodriguez, Highly active copper-ceria and copper-ceria-titania catalysts for methanol synthesis from CO_2, Science 345 (2014) 546–550.

[188] S. Hilaire, X. Wang, T. Luo, R.J. Gorte, J. Wagner, A comparative study of water-gas-shift reaction over ceria-supported metallic catalysts, Appl. Catal. A 258 (2004) 271–276.

[189] K. Otsuka, Y. Wang, E. Sunada, I. Yamanaka, Direct partial oxidation of methane to synthesis gas by cerium oxide, J. Catal. 175 (1998) 152–160.

[190] S. Sharma, S. Hilaire, J.M. Vohs, R.J. Gorte, H.W. Jen, Evidence for oxidation of ceria by CO_2, J. Catal. 190 (2000) 199–204.

[191] A. Bueno-López, K. Krishna, M. Makkee, Oxygen exchange mechanism between isotopic CO_2 and Pt/CeO_2, Appl. Catal. A 342 (2008) 144–149.

[192] S.D. Senanayake, D.R. Mullins, Redox pathways for HCOOH decomposition over CeO_2 surfaces, J. Phys. Chem. C 112 (2008) 9744–9752.

[193] Y. Lykhach, T. Staudt, R. Streber, M. Lorenz, A. Bayer, H.-P. Steinrück, J. Libuda, CO_2 activation on single crystal based ceria and magnesia/ceria model catalysts, Eur. Phys. J. B 75 (2010) 89–100.

[194] T. Staudt, Y. Lykhach, N. Tsud, T. Skála, K.C. Prince, V. Matolín, J. Libuda, Electronic structure of magnesia−ceria model catalysts, CO_2 adsorption, and CO_2 activation: A synchrotron radiation photoelectron spectroscopy study, J. Phys. Chem. C 115 (2011)

8716–8724.

[195] T. Staudt, Y. Lykhach, N. Tsud, T. Skála, K.C. Prince, V. Matolín, J. Libuda, Ceria reoxidation by CO_2: A model study, J. Catal. 275 (2010) 181–185.

[196] K.R. Hahn, M. Iannuzzi, A.P. Seitsonen, J. Hutter, Coverage effect of the CO_2 adsorption mechanisms on CeO_2(111) by first principles analysis, J. Phys. Chem. C 117 (2013) 1701–1711.

[197] P.M. Albrecht, D.-e. Jiang, D.R. Mullins, CO_2 adsorption as a flat-lying, tridentate carbonate on CeO_2(100), J. Phys. Chem. C 118 (2014) 9042–9050.

[198] Z. Cheng, B.J. Sherman, C.S. Lo, Carbon dioxide activation and dissociation on ceria (110): A density functional theory study, J. Chem. Phys. 138 (2013) 014702.

[199] M.W. Abee, S.C. York, D.F. Cox, CO_2 Adsorption on α-Cr_2O_3 (101-2) surfaces, J. Phys. Chem. B 105 (2001) 7755–7761.

[200] C.T. Au, W. Hirsch, W. Hirschwald, Adsorption and interaction of carbon dioxide, formic acid and hydrogen/carbon dioxide mixtures on (1010) zinc oxide surfaces studied by photoelectron spectroscopy (XPS and UPS), Surf. Sci. 199 (1988) 507–517.

[201] C.T. Au, W. Hirsch, W. Hirschwald, Adsorption of carbon monoxide and carbon dioxide on annealed and defect zinc oxide (0001) surfaces studied by photoelectron spectroscopy (XPS and UPS), Surf. Sci. 197 (1988) 391–401.

[202] S.D. Senanayake, D. Stacchiola, J. Evans, M. Estrella, L. Barrio, M. Pérez, J. Hrbek, J.A. Rodriguez, Probing the reaction intermediates for the water-gas shift over inverse CeO_x/Au(111) catalysts, J. Catal. 271 (2010) 392–400.

[203] G. Illing, D. Heskett, E.W. Plummer, H.J. Freund, J. Somers, T. Lindner, A.M. Bradshaw, U. Buskotte, M. Neumann, U. Starke, K. Heinz, P.L. De Andres, D. Saldin, J.B. Pendry, Adsorption and reaction of CO_2 on Ni{110}: X-ray photoemission, near-edge X-ray absorption fine-structure and diffuse leed studies, Surf. Sci. 206 (1988) 1–19.

[204] A. Fujimori, Y. Sugita, H. Nakahara, E. Ito, M. Hara, N. Matsuie, K. Kanai, Y. Ouchi, K. Seki, Change of molecular packing and orientation from monolayer to multilayers of hydrogenated and fluorinated carboxylates studied by in-plane X-ray diffraction together with NEXAFS spectroscopy at C K-edge, Chem. Phys. Lett. 387 (2004) 345–351.

[205] P.A. Stevens, R.J. Madix, J. Stöhr, NEXAFS study of HCOO/Ag(110): Evidence for dynamic bending, Surf. Sci. 230 (1990) 1–12.

[206] R. Davis, J.F. Walsh, C.A. Muryn, G. Thornton, V.R. Dhanak, K.C. Prince, The orientation of formate and carbonate on ZnO(101-0), Surf. Sci. 298 (1993) L196–L202.

[207] R. Lindsay, A. Gutiérrez-Sosa, G. Thornton, A. Ludviksson, S. Parker, C.T. Campbell, NEXAFS study of CO adsorption on ZnO(000-1)–O and ZnO(000-1)–O/Cu, Surf. Sci. 439 (1999) 131–138.

[208] A. Gutiérrez-Sosa, T.M. Evans, S.C. Parker, C.T. Campbell, G. Thornton, Geometry of C1–3 oxygenates on ZnO(0001)–Zn, Surf. Sci. 497 (2002) 239–246.

[209] T. Jin, Y. Zhou, G.J. Mains, J.M. White, Infrared and x-ray photoelectron spectroscopy study of carbon monoxide and carbon dioxide on platinum/ceria, J. Phys. Chem. 91 (1987) 5931–5937.

[210] D.R. Mullins, T.S. McDonald, Adsorption and reaction of hydrogen sulfide on thin-film cerium oxide, Surf. Sci. 601 (2007) 4931–4938.

[211] D.R. Mullins, T.S. McDonald, Adsorption and reaction of methanethiol on thin-film cerium oxide, Surf. Sci. 602 (2008) 1280–1287.

[212] A.H. England, A.M. Duffin, C.P. Schwartz, J.S. Uejio, D. Prendergast, R.J. Saykally, On the hydration and hydrolysis of carbon dioxide, Chem. Phys. Lett. 514 (2011) 187–195.

Publication list

[1] X. Yu, Z. Zhang, **C. Yang**, F. Bebensee, S. Heissler, A. Nefedov, M. Tang, Q. Ge, L. Chen, B. K. Kay, Z. Dohnálek, Y. Wang, C. Wöll, Interaction of formaldehyde with the rutile TiO_2(110) surface: a combined experimental and theoretical study, *Journal of Physical Chemistry C*, 2016, 120, 12626.

[2] **C. Yang**, F. Bebensee, A. Nefedov, C. Wöll, T. Kropp, L. Komissarov, C. Penschke, R. Moerer, J. Paier, J. Sauer, Methanol adsorption on monocrystalline ceria surfaces, *Journal of Catalysis*, 2016, 336, 116. (**Featured article**)

[3] W. Guo, Z. Chen, **C. Yang**, T. Neumann, C. Kübel, W. Wenzel, A. Welle, W. Pfleging, O. Shekhah, C. Wöll, E. Redel, Bi_2O_3 nanoparticles encapsulated in surface mounted metalorganic frameworks, *Nanoscale*, 2016, 8, 6468.

[4] M. Buchholz, X. Yu, **C. Yang**, S. Heissler, A. Nefedov, Y. Wang, C. Wöll, IR-spectroscopy of CO adsorption on mixed-terminated ZnO surfaces, *Surface Science*, 2016, 652, 247.

[5] W. Feng, L. Li, **C. Yang**, A. Welle, O. Trapp, P. A. Levkin, UV-induced tetrazole-thiol reaction for polymer conjugation and surface functionalization, *Angewandte Chemie International Edition*, 2015, 54, 8732.

[6] H. Sezen, H. Shang, F. Bebensee, **C. Yang**, M. Buchholz, A. Nefedov, S. Heissler, C. Carbogno, M. Scheffler, P. Rinke, C. Wöll, Evidence for photogenerated intermediate hole polarons in ZnO, *Nature Communications*, 2015, 6, 6901.

[7] Z. Wang, H. Sezen, J. Liu, **C. Yang**, S. E. Roggenbuck, K. Peikert, M. Fröba, A. Mavrandonakis, B. Supronowicz, T. Heine, H. Gliemann, C. Wöll, Tunable coordinative defects in UHM-3 surface-mounted MOFs for gas adsorption and separation: A combined experimental and theoretical study, *Microporous and Mesoporous Materials*, 2015, 207, 53.

[8] **C. Yang**, L. Yin, F. Bebensee, M. Buchholz, H. Sezen, S. Heissler, J. Chen, A. Nefedov, H. Idriss, X. Gong, C. Wöll, Chemical activity of oxygen vacancies on ceria: a combined experimental and theoretical study on CeO_2(111), *Physical Chemistry Chemical Physics*, 2014, 16, 24165. (**Featured on front cover**)

[9] X. Du, L. Li, J. Li, **C. Yang**, N. Frenkel, A. Welle, S. Heissler, A. Nefedov, M. Grunze, P. A. Levkin, UV-triggered dopamine polymerization: control of polymerization, surface coating, and photopatterning, *Advanced Materials*, 2014, 26, 8029.

[10] **C. Yang**, A. Nefedov, F. Bebensee, C. Wöll, Comparison of CO adsorption on CeO_2(111) single crystals and films, to be submitted.

[11] **C. Yang**, F. Bebensee, J. Chen, X. Yu, C. Wöll, A. Nefedov, Carbon dioxide adsorption on CeO_2(110): an XPS and NEXAFS study, to be submitted.

[12] **C. Yang**, A. Nefedov, A. Trovarelli, Y. Wang, C. Wöll, Structure and reactivity of ceria (110) surface, to be submitted.

[13] **C. Yang**, T. Kropp, A. Nefedov, J. Paier, Y. Wang, J. Sauer, C. Wöll, Activation and adsorption of oxygen on ceria surfaces, in preparation.

[14] **C. Yang**, A. Nefedov, X. Yu, L. Schöttner, F. Bebensee, Y. Wang, C. Wöll, Decomposition of N_2O over ceria surfaces, in preparation.

Conference contributions

[1] **C. Yang**, A. Nefedov, Y. Wang, C. Wöll, N_2O photochemical depletion at nonstoichiometric ceria surfaces, 16th International Congress on Catalysis, 2016, Beijing, China.

[2] **C. Yang**, A. Nefedov, Y. Wang, C. Wöll, Structure and reactivity of ceria single crystal surfaces studied by IR spectroscopy, 115th General Assembly of the German Bunsen Society for Physical Chemistry, 2016, Rostock, Germany.

[3] **C. Yang**, A. Nefedov, Y. Wang, C. Wöll, UHV-IR spectroscopy study of carbon monoxide adsorption on ceria single crystal surfaces, 80th Annual Conference of the DPG and DPG Spring Meeting, 2016, Regensburg, Germany.

[4] **C. Yang**, A. Nefedov, Y. Wang, C. Wöll, IR-probes for ceria surfaces: a comparison of CO and CH_3OH applied to CeO_2(111), CeO_2(110) and ceria powders, 10th International Workshop on Oxide Surfaces, 2016, Dalian, China.

[5] **C. Yang**, L. Schöttner, A. Nefedov, F. Bebensee, C. Wöll, NEXAFS studies of N_2O conversion on reduced ceria surface, 16th International Conference on X-ray Absorption Fine Structure, 2015, Karlsruhe, Germany.

[6] **C. Yang**, X. Yu, A. Nefedov, F. Bebensee, C. Wöll, CO_2 adsorption on CeO_2(110), 16th International Conference on X-ray Absorption Fine Structure, 2015, Karlsruhe, Germany.

[7] **C. Yang**, L. Yin, F. Bebensee, A. Nefedov, X. Gong, C. Wöll, UHV-IR spectroscopy study of carbon monoxide adsorption on CeO_2(111) single crystal surface, Workshop on

Ceria-based Materials in Catalysis and Electrochemistry, 2015, Schloss Rauischholzhausen , Germany.

[8] **C. Yang**, A. Nefedov, X. Yu, J. Chen, F. Bebensee, C. Wöll, Spectroscopy studies of CO_2 adsorption on CeO_2(110), 114th General Assembly of the German Bunsen Society for Physical Chemistry, 2015, Bochum, Germany.

[9] **C. Yang**, F. Bebensee, A. Nefedov, C. Wöll, IRRAS studies of methanol adsorption on CeO_2(111), 114th General Assembly of the German Bunsen Society for Physical Chemistry, 2015, Bochum, Germany.

[10] **C. Yang**, F. Bebensee, A. Nefedov, C. Wöll, Methanol adsorption on CeO_2(111) single crystal surface, DPG Spring Meeting, 2015, Berlin, Germany.

[11] **C. Yang**, A. Nefedov, J. Chen, F. Bebensee, C. Wöll, CO_2 adsorption on CeO_2(110) single crystal surface, DPG Spring Meeting, 2015, Berlin, Germany.

[12] **C. Yang**, A. Nefedov, F. Bebensee, J. Chen, C. Wöll, CO_2 adsorption on CeO_2(110) single crystal surface, 6th Joint Ber II and Bessy II User Meeting, 2014, Berlin, Germany.

[13] **C. Yang**, M. Buchholz, F. Bebensee, J. Chen, A. Nefedov, C. Wöll, UHV-IR spectroscopy study of carbon monoxide adsorption on cerium oxide surfaces, 113th General Assembly of the German Bunsen Society for Physical Chemistry, 2014, Hamburg, Germany.